Titre: Title:	CFD-DEM Hybrid Modelling of Multiphase Gravity-Driven Granular Flows
Auteur: Author:	Maryam Shademani
Date:	2020
Type:	Mémoire ou thèse / Dissertation or Thesis
Référence: Citation:	Shademani, M. (2020). CFD-DEM Hybrid Modelling of Multiphase Gravity-Driven Granular Flows [Master's thesis, Polytechnique Montréal]. PolyPublie. https://publications.polymtl.ca/5283/

URL de PolyPublie: PolyPublie URL:	https://publications.polymtl.ca/5283/
Directeurs de recherche: Advisors:	Ahmad Shakibaeinia, & Bruno Blais
Programme: Program:	Génies civil, géologique et des mines

POLYTECHNIQUE MONTRÉAL

affiliée à l'Université de Montréal

CFD-DEM Hybrid Modelling of Multiphase Gravity-Driven Granular Flows

MARYAM SHADEMANI

Département des Génies civil, géologique et des mines

Mémoire Présenté en vue de l'obtention du diplôme de *Maîtrise ès sciences appliquées*

Génie Civil

Avril 2020

POLYTECHNIQUE MONTRÉAL

affiliée à l'Université de Montréal

Ce mémoire intitulé:

CFD-DEM Hybrid Modelling of Multiphase Gravity-Driven Granular Flows

Présenté par **Maryam SHADEMANI**

en vue de l'obtention du diplôme de Maîtrise ès sciences appliquées

a été dûment accepté par le jury d'examen constitué de :

Tew-Fik MAHDI, président
Ahmad SHAKIBAEINIA, directrice de recherche
Bruno BLAIS, codirectrice de recherche
Elmira HASSANZADEH, membre

DEDICATION

To my beloved parents, Mahnaz and Hossein

And my sweet sister, Melika

ACKNOWLEDGEMENTS

I express my sincere appreciation to those who have contributed to this thesis and supported me during this journey for without any of them, this research work would not have been possible.

First, I would like to express my deepest appreciation to my supervisor Prof. Shakibaeinia for his supporting to complete my master thesis. His deep insight helped me at various stages of my research. Very thank for his contributions of time and ideas to make my research productive. Joining to his research group was the best experience for me.

I am extremely grateful to my co-supervisor prof. Blais for his priceless suggestions, ideas and advices at each stages of my research. Thank you for his valuable time, co-operating, and generosity which set this work possible as it is till end.

Very special thanks to my dear parents, my sweet sister and my dear uncle for all their help and support. They have been a constant source of strength and inspiration to me.

I also thank all my friends who I met them in Montreal for helping me during these years of my study both emotionally and academically.

RÉSUMÉ

Les matériaux granulaires se trouvent dans de nombreux processus industriels, les sciences naturelles et notre vie quotidienne. La prédiction du comportement complexe des écoulements granulaires est cruciale pour une conception plus efficace, valide et fiable dans de nombreux problèmes d'ingénierie. En outre, les écoulements granulaires entraînés par l'effet de gravité sous forme de coulées de débris, glissements de terrain, et les avalanches pourraient entraîner des conséquences dévastatrices en raison de leur longue distance parcourue, de leur vitesse d'écoulement élevée et de leur mouvement massif. Compte tenu de ces derniers, la prédiction du comportement et du mécanisme des écoulements granulaires devient nécessaire et d'une importance cruciale.

L'étude des matériaux granulaires est souvent extrêmement difficile car les matériaux granulaires peuvent se comporter soit sous forme liquide, solide ou gazeuse dans des différentes circonstances. De plus, dans le monde réel, les écoulements granulaires ne sont pas toujours considérés comme des écoulements monophasiques car dans de nombreuses applications ils se sont entourés d'un fluide ambiant. Dans ce cas, le comportement de ce genre des écoulements est de nature multiphasique et complexe. De nombreuses études expérimentales ont été menées pour explorer le mécanisme et le comportement des écoulements granulaires. Néanmoins, les études expérimentales sont souvent coûteuses et longues. Aujourd'hui, la capacité croissante de la puissance de calcul des ordinateurs ouvre de nouvelles perspectives pour la modélisation et la simulation numérique des écoulements granulaires que ce soit pour compléter ou voire même remplacer totalement les études expérimentales.

L'objectif de cette étude est de développer un modèle numérique capable de simuler des écoulements multiphasiques granulaires en se basant sur une stratégie de couplage CFD-DEM. Dans cette stratégie, la méthode DEM (Discrete Element Method) est mis en œuvre pour simuler l'interaction particule-particule du système granulaire, tandis que la CFD (Computational Fluid Dynamics) est utilisée pour modéliser l'écoulement du fluide tout en résolvant les équations de Navier-Stokes. La difficulté de la simulation des écoulements granulaires multiphasiques provient de la complexité de l'interaction entre le fluide et les particules granulaires ainsi qu'entre les particules granulaires elles-même. Dans la stratégie de couplage CFD-DEM, l'interaction entre la

particule granulaire et le fluide est prise en compte par l'échange des forces d'interaction telles que la force de traînée et la force ascensionnelle respectivement entre le solveur DEM et le solveur CFD. Pour capter la dynamique de la surface libre du fluid, la méthode VOF (Volume Of Fluid) est également incorporée dans le cadre de la stratégie de couplage CFD-DEM.

Les calculs sont effectués avec le programme à code source ouvert CFDEM®coupling. Ce dernier combine le code OpenFOAM qui est basé sur un solveur en volumes finis (FVM) et le code LIGGGHTS qui est basé sur la méthode DEM. Pour intégrer la méthode VOF dans le programme CFDEM®coupling afin de capter la surface libre de l'écoulement, le interFOAM qui est un progiciel appartenant au code OpenFOAM est utilisé.

Le modèle développé a été d'abord validé à travers le test de sédimentation d'une seule particule de matériau granulaire dans le fluide dont la solution analytique est disponible. Le modèle aussi fournit des résultats raisonnables par rapport aux résultats expérimentaux extraits du test d'effondrement d’une colonne de matériau granulaire immergé dans l’eau. Pour valider quantitativement ce dernier cas test, le déplacement du front de colonne du matériau granulaire obtenu numériquement a été tracé avec les résultats expérimentaux correspondants. Les trois régimes ont été distingués numériquement comme il est observé à travers les résultats expérimentaux. Le champ de vitesse extrait de la simulation numérique montre les mêmes zones déformées et non-déformées (solides) de matériau granulaire comme dans l'expérience.

Le solveur développé a été utilisé pour simuler le glissement de terrain sous-marin d’une colonne de matériau granulaire. L'évolution globale de la masse granulaire était relativement en accord avec l'expérience. Quelques différences, telle qu’un mouvement plus lent de la masse, entre les résultats numériques et expérimentaux ont été observées et sont causées entre autres par l’ouverture de la vanne.

ABSTRACT

Granular materials are ubiquitous in many industrial processes, the natural sciences, and our everyday life. Prediction of the complex behavior of the granular flow is crucial for a more efficient, effective, and reliable design in many engineering problems. Furthermore, gravity-driven granular flows in forms of debris flows, landslides, and avalanches could lead to devastating consequences due to their long runout distance, their high flow velocity and their massive movement. Considering these devastating consequences, prediction of the behavior and mechanism of granular flows become necessary and of crucial importance.

Investigation of the granular flows is often extremely difficult since granular materials may behave either as a liquid, a solid or a gas under different circumstances. In addition, in the real world, granular flows are not always considered as a single-phase flow since in many applications they are surrounded by an ambient fluid. In this circumstance, the behaviour of this kind of flows is of multiphase and complex nature. Many experimental studies have been carried out to explore the mechanism and behavior of granular flows. However experimental studies are frequently expensive and time consuming. Nowadays, the increasing capability of the computational power of computers opens up new perspectives for the modeling and numerical simulation of granular flows, whether it is to supplement or even to replace totally the experimental studies.

The objective of this study is to develop a numerical model capable of simulating multiphase granular flows based on a CFD-DEM coupling strategy. In this method, Discrete Element Method (DEM) is implemented to simulate the particle-particle interaction of the granular system, whilst the Computational fluid Dynamic (CFD) is employed to model the fluid phase by solving the Navier-stokes equation. The difficulty in simulating multiphase granular flows comes from the complexity of the interaction between the fluid and the granular particle as well as between the granular particles themselves. In the CFD-DEM coupling strategy, the particle-fluid interaction is taken into account through the exchanging of the interaction forces such as the drag force and buoyancy force between DEM and CFD solvers, respectively. To capture the dynamic of free surface fluid, also Volume Of Fluid (VOF) method is incorporated into the CFD-DEM coupling framework.

The computations are conducted with the opensource code CFDEMcoupling. This software package combines OpenFOAM based on the finite volume solver and LIGGGHTS based on DEM method. To integrated VOF method into the CFDEM coupling in order to capture the free surface flow, the interFOAM solver available in OpenFOAM code is used

The developed model was first validated by one single particle settling test from air to the fluid and has a good agreement with the analytical solution. The model also for the submerged granular collapse provides reasonable results in comparison with experimental results. To validate this case quantitively, the runout distance was plotted against the corresponding experimental results. The three regimes were distinguished numerically as observed through the experimental results. The velocity field also extracted from the simulation shows the same yielded and non-yielded zones as the experimental.

The developed solver was also used to simulate the submerged granular slide. The overall evolution of the granular mass was relatively in good agreement with the experiment (i.e. forming the thick frontier and the thinner tail). However, some discrepancies (i.e. slower motion and forming one granular mass circulation) between the numerical results and the experimental results were observed for this test case which may be related to the gate mechanism.

TABLE OF CONTENTS

LIST OF TABLES

LIST OF FIGURES

LIST OF SYMBOLS AND ABBREVIATIONS

G-PIV	Granular Particle image Velocimetry
TFM	Two Fluid Model
MPS	Moving Particle Semi-implicit
SPH	Smoothed Particle Hydrodynamics
DEM	Discrete Element Method
LES	Large Eddy Simulation
DNS	Direct Numerical Simulation
LB	Lattice-Boltzman
CFD	Computational Fluid Dynamic
LS	Level Set
VOF	Volume of Fluid method
IBM	Immersed Boundary Method
CLS	Conservative Level Set
RMSE	Root Mean Squar Error

CHAPTER 1 INTRODUCTION

1.1 Context and Motivation

Granular material is defined as a group of distinct macroscopic particles interacting through contact interactions [1] . A granular medium is an assembly of particles with a size greater than 100 μm. In Brownian particles or molecules with smaller sizes, other interactions such as Van der Walls forces are dominant as well as friction and collision forces. In granular media with even smaller sizes ($\leq 1\mu m$), thermal agitation should be considered for particle collisions. However, the term of granular flow is often referred to the flow of granular materials where the particles are large enough that the Brownian motion can be neglected [1-3]. Granular materials, of which sand is a common example, are one of the most important materials in many natural and engineering processes. Figure 1-1 shows examples of granular materials in day-to-day life and in engineering

Figure 1-1 Examples of granular materials (food grain, rock, pharmaceutical grains, sand, industrial grains (image has taken from: [4-8]).

Granular materials are found in various industrial areas such as chemical, petroleum, metallurgical, pharmaceutical and food processes. Common examples of granular flows in geophysics and civil engineering are debris flows, turbidity currents, sediment transportations, snow avalanches, pyroclastic flows. Being able to predict the complex behavior of the granular flow is crucial for more efficient, effective, and reliable design [9] in many engineering problems.

Additionally, granular flow is the core element of in many natural disasters, with devastating consequences, such as landslides, debris flows, mud flows and avalanches. Due to their long runout distance, high flow velocity and the massive movement of materials, they cause serious damages to people’s life and properties. According to some reports, a big portion of the casualties from natural disasters such as storms and earthquakes is caused by the debris flows on the steep lands. In addition to the direct damages of debris flows on people’s life, damages to the infrastructures and agricultural lands as well as the indirect cost generated by traffic and communication interruption can not been overlooked [10]. Based on the reports of the QUEBEC Ministry of Transport, 350 landslides reported in 2017 led to residence destruction, hydro tower damages and the closure of the major freeway for more than a month. Furthermore, historical reports of landslide indicate that at least 278 people have died in Quebec due to devastating results of landslides. The deadliest report of landslide in Quebec happened in Champlain street in Quebec City where 93 people lost their life [11].

Another form of natural granular flows causing devastating consequences are explosive volcanic eruptions triggered by a mixture of gas and magma under high pressure and velocity. One of the most dangerous volcanic events is the pyroclastic density current which is a cloud containing a high concentration of volcanic materials and moving at high velocity [12, 13]. Obviously, a deep understanding of these hazardous natural phenomena and their features could provide engineers with predictive techniques required to avoid such catastrophic consequences. Furthermore, granular flows in form of sediment transport is a phenomenon which plays a critical role in transport processes and erosion in coastal regions and lakes [14].

Figure 1-2 Hanging of a house on the edge of a cliff in Saint Roch de Richelieu, Quebec, after a landslide [11].

1.1.1 Granular regimes

One difficulty associated with understanding the granular materials is that they behave like different physical state of matter, depending on the way they are dealt [1, 15]. As Figure 1-3 shows, the granular media can behave as liquid, solid and gas, in different condition. Hence, in order to understand the complex physics of granular flows, three different granular flow regimes have been defined. The gaseous or collisional regime is defined where the flow is dilute (no permeant contacts between the grains), and the kinetic theory of gases are applied to describe the particles motion. The quasi-static (solid) regime is referred to those granular regimes, in which the interaction of particles is associated with very slow deformations and hence plasticity theories are used to describe the particle interactions. The liquid regime, which also known as dense granular flow, is a kind of regime where the grains are in contact and flow like a viscous liquid. In aquatic sediment transport literature, these three gaseous, quasi-static, and dense flow regimes are referred as suspended load, in-active (immobile) sediments, and the bed load, respectively. Here the focus is on the solid and dense granular flow regimes, also known as visco-plastic flow, which is the common form of granular flows [1, 16]. One can also categorize the granular flow regimes based on the dominant force that drives the granular material. In this regard, the granular flows can be gravity-driven (e.g. in case of landslides), or flow-driven (e.g. in case of fluvial sediment transport).

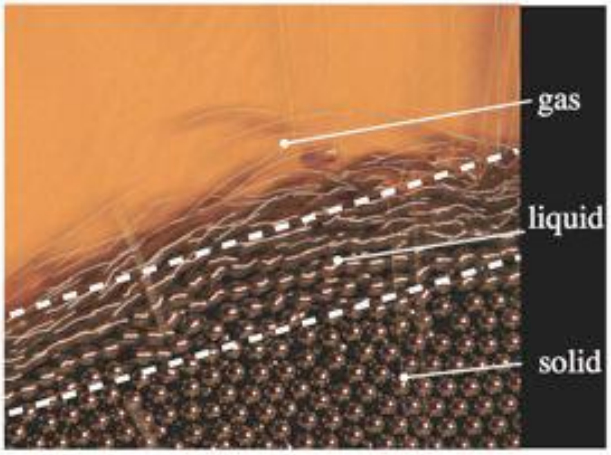

Figure 1-3 Different physical states of granular flows[1]

In respect to present of ambient fluid, the granular flow can be classified as dry granular flows, and multiphase (fully saturated or partially saturated) granular flows. The presence of the liquid phase in a granular flow plays an important role in the materials' behaviour since the particles interact with the surrounding fluid in addition to the other particles [3]. While, the rheology (i.e. stress-strain rate relationship) of the dry granular flows is only determined by friction and collision between particles, in the multiphase granular flows, the liquid phase changes the rheology of the granular media. In order to understand better, the multiphase granular flow, three different regimes have been defined in the literature, including: the free-fall regime, viscous regime, and inertial regime. In the free fall regime, the drag force applied on the particle from the liquid can be neglected. Dry granular flows (where the ambient fluid is air) belong to this regime. In the viscous regime, the viscosity of the fluid (and the drag force) plays an important role in particles motions. In the third regime, the inertial regime, the fluid viscosity and the strain rates can be neglected. In this regime, particle velocities are controlled by the drag force [1, 15]. Figure 1-4 shows a phase diagram, in which the scope of the three different regimes are defined by two dimensionless numbers: St (Stokes) and r (related to the fluid-grain density ratio). If $St >> 1$ and $r >> 1$ the flow regime belongs to the free fall regime or dry granular flow. While If $St << 1$ and $r >> 1$ the viscosity is dominated and if $St << 1$ and $r << 1$ the regime is inertial.

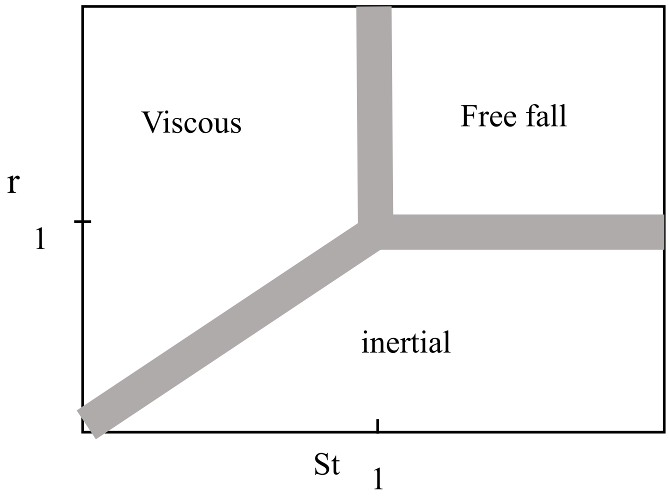

Figure 1-4 . Different flow regimes corresponding the dimensionless number St and r for multiphase granular flows [1].

Therefore, due to the diverse behaviour of granular flows considering the different flow regimes and transition between these regimes the investigation of granular flow behaviour is challenging. Furthermore, the evaluation of the complex interaction between particle-particle and fluid-particle, is difficult. Despite the numerous research efforts focused on the granular flow's behaviour, this field of study remains an active area of research.

1.2 Literature review

1.2.1 Experimental studies

Multiphase granular flows are complicated phenomena with nonuniform, complex and unsteady rheologies [14]. Many studies have focused on catastrophe prevention of granular flows such as landslides and avalanches as mentioned above. Due to the importance of such phenomena, many experimental studies have been conducted to observe and give new insight on both flow-driven and gravity-driven granular flows.

Some experimental efforts studied the steady state condition of the gravity-driven granular flow on slopes. These studies investigated the friction effects and depth-averaged hydrodynamic equations [2, 17, 18]. Some experimental studies on two-dimensional and axisymmetric granular collapse have been conducted in various geometrical conditions and with different material properties [19-23]. Thompson et al. [23] studied the behaviour of granular collapse qualitatively by describing the final runout distance as a function of the proportion of the initial height to initial horizontal spread of the granular column. Laboratory experiments on granular slide also have been performed using various conditions such as different material types, slope angles and flow regimes. Pilvar et al. [24] experimentally studied the granular slide for sub-aerial, submerged and transitional conditions. The work of [20, 21, 25] studied the morphodynamic of granular sliding (down an slope) for different slope angles. They identified three phases in movement of materials (and the time series of runout distance), which included: an acceleration phase, a steady flow phase, and a deceleration phase. Furthermore, the internal flow structure has also been the interest of many experimental studies. For this purpose, they used granular particle image velocimetry (G-PIV) technique to quantify the morphology (shape evolution) and the velocity fields of unsteady granular flows [24, 26, 27].

1.2.2 Numerical studies

Compared with experimental studies, numerical methods are more interesting to investigate the multiphase granular flows behaviour because they are less expensive and time-consuming and more flexible comparing that the experimental works. With the advancements of the computational power and the numerical methods and techniques, numerical simulations are more effective to study these complex phenomena. The complexity of multiphase granular flow arises from the simultaneous interaction between different phases (gas, liquid and solid particles) as well as the particle-particle interactions. For the particular case of sediment transport modelling, the majority of past studies are based on single-phase numerical models that solve the flow equations associated with advection-diffusion equation and empirical relations [28, 29]. These methods are only appropriate for the low-dynamic sediment transport problems. The numerical methods for more generalized case of granular flows are however multiphase (granular material and ambient fluid as separate phases). Based on the description of the granular phase, these methods typically can be categorized into two groups of a continuum-based methods and a discrete-based methods method [30].

1.2.2.1 Continuum-based models

The Continuum-based models consider the granular mass as a body of continuum, whose behaviour predicted using a rheological model. Considerable research attention has been devoted to the continuum method to investigate the general behavior of the granular flows. Some of these methods are based on a fully Eulerian framework. In Eulerian context, the computational domain consists of mesh grids and, assuming that in each cell there is a uniform phase, physical parameters can be calculated in each cell. One popular method, belonging to the continuum family, is the TFM which was first proposed by Anderson [31]. In this method, both liquid and solid phases are considered as two fluids and their physical properties are determined by the conservation of mass and momentum equations based on the local averaged Navier-Stokes equations. However, this method has limitations to model granular flows with fast flow regimes [30]. Furthermore, some continuum approaches based on Lagrangian framework, used meshfree particle method such as moving particle semi-implicit (MPS) [32] and smoothed particle hydrodynamics (SPH) [33]. These Lagrangian meshfree methods are suitable to model large interfacial deformations and fragmentations in continuum simulations [34, 35]. After the development of MPS, a new method known as WC-MPS method has been implemented to the multiphase granular flows. This method considers the multiphase system as a multi-density and multi-viscosity continuum system [34]. Although all these continuum-based methods could successfully model multiphase granular flows, the interaction between particles are disregarded. In addition, no continuum theory (and rheological model) has been proved to be valid to all flow conditions.

1.2.2.2 Discrete-based models

In contrast, the second group of methods treats granular phase as a discrete media, by modelling each single grain. Different discrete models have been developed such as the Monte Carlo method, the cellular automata and the discrete element method (DEM) [36]. The DEM method was originally introduced by Cundall Strack in 1979 [37] and today it became an effective method of addressing granular materials. The last few years have seen an increased interest in this method and a large number of papers have been published based on DEM in the literature. DEM belongs to the Lagrangian methods in which the dynamic behaviour of each particles is considered individually based on Newton's second law of motion [36]. Two types of motions of particles are defined in the DEM method including translational and rotational. Figure 1-5 shows the typical forces and torques applied schematically in a particle in DEM.

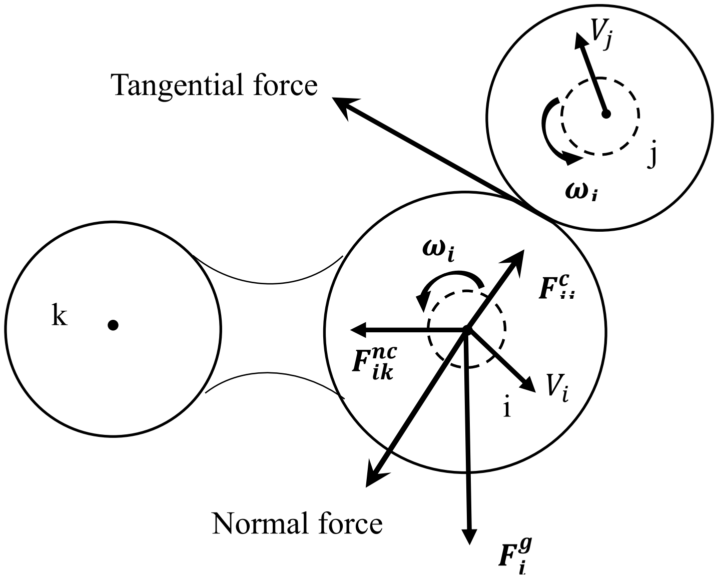

Figure 1-5 Forces acting on particle *i* resulted from Contact forces (with particle j) and non-contact force (particle k) [36].

The governing equations of these motions for particle *i* are expressed as[36]:

$$m_i \frac{d\mathbf{V}_i}{dt} = \sum_j \mathbf{F}^c_{ij} + \sum_k \mathbf{F}^{nc}_{ik} + \mathbf{F}^f_i + \mathbf{F}^g_i \qquad \text{Eq. 1-1}$$

$$I_i \frac{d\boldsymbol{\omega}_i}{dt} = \sum_j \mathbf{M}_{ij} \qquad \text{Eq. 1-2}$$

respectively.$\mathbf{F}^c_{ij}$ is the contact force of the interparticle and $\mathbf{M}_{ij}$ is the torque acting on particle *i* by particle j. $\mathbf{F}^{nc}_{ik}$ are the non-contact forces such as the van der Waals forces and the electrostatics forces acting on particle *i* by particle k. Finally, $\mathbf{F}^g_i$ is the gravitational force. The contact forces are comprised of the normal forces and of the tangential forces. Several methods have been introduced to evaluate the forces and torques involved in the DEM method. The simplest model to calculate the normal force is known as the linear spring-dashpot (Figure 1-6) which was introduced by Cundall and Strack (1979). This method is widely used to model granular materials due to its simplicity.

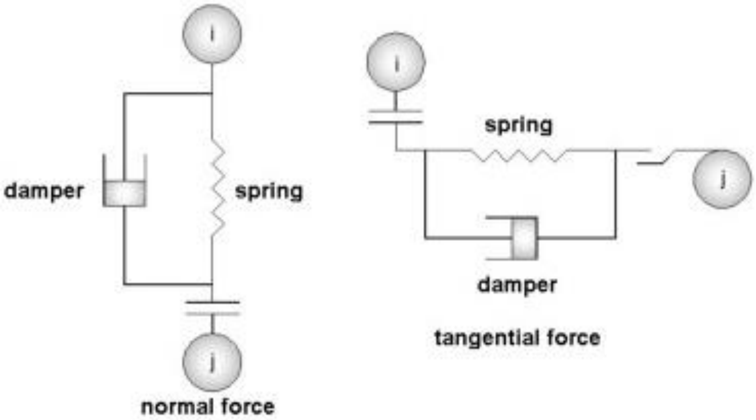

Figure 1-6 Schematic of spring-dashpot contact model for normal and tangential force [38]

In addition to the linear models, non-liners models have been proposed in which the relation between the normal displacement and the normal force is non-linear.

One of the capabilities of DEM method is the evaluation of non-contact forces. The non-contact forces can be combination of three forces including the van der Waals force, electrostatic force and capillary force. In Cohesive particles like sedimentation of fine particles, these forces can not be disregarded and are dominant forces. DEM method enables to considers non-contact forces directly [36, 39].

Different contact and non-contact models have been introduced in literature and Table 1-1 shows a summary of development of force models in DEM.

Although nonlinear models using Hertz and Mindlin-Deresiwicz methods may be more accurate comparing to the linear models, studies conducted by Dio Renzo et al show that using complex models does not significantly improve the results. Therefore, linear methods sometimes can be more effective than complex models which are more time consuming[39].

Table 1-1 A brief review of DEM development

Ref no	Developer name	year	Type of force/torque	Model proposed
[37]	Cundall and Strack	1979	Contact force	Linear spring-dashpot
[40]	Di Renzo and Di Maio	2004	Contact force	Linear spring without dashpot
[41]	Hertz	1882	Contact force	Non-linear normal force
[42]	Mindlin and Deresiewicz	1953	Contact force	Tangential force model based on loading histories
[43]	Langston	1994	Contact force	New simple tangential force and Hertz model for normal force
[44]	Thornton	1997	Contact force	Normal contact force between two elastic and plastic spheres
[45] [46]	Zhu Iwashita	1999 1998	Contact torque	Rolling friction torque using tangential forces

Table 1-1 A brief review of DEM development (continued)

Ref no	Developer name	year	Type of force/torque	Model proposed
[47] [48]	Pelessone Bertrand et al	2003 2005	Contact force	Contact force for non-spherical particles using multi-sphere approach
[49]	Hamaker	1937	Non-contact force	Developing van der Waals force using dipole interaction
[50]	Krupp	1967	Non-contact force	Developing Electrostatic force using Coulomb force
[51] [52]	Fisher Lian et al.	1926 1993	Non-contact force	Developing liquid bridge force using surface tension

DEM has been widely used to model packing and flow of particles which is important to many industrial processes [39]. In terms of particle packing, DEM can be implemented to simulate the pouring and deposition of particles under the gravity force [39]. Hence, several studies have been carried out to describe the macroscopic properties and force distribution of particles packing by means of the DEM method. For instance, Zhou et al, Wei et al and Li et al [53-56] predicted the angle of repose of granular martials precisely by DEM simulation. Predicting the internal force structure of granular pack is an important advantage of numerical modeling since the existing laboratories techniques can only measure the external forces. Various DEM simulations have been conducted to evaluate force networks in granular materials. Matuttis et al., [57] worked on microscopic and macroscopic information of the static packing of granular materials by modeling the forces on the particle level. They successfully simulated the force network for spherical and polygonal particles. Zhou et al., [58] studied the effect of base deflection on the normal pressure distribution under a sandpile. More recently, studies on force network have been done on the kinematic of force chain of granular materials. For instance, Tordesillas et al.[59] applied the DEM method on a two-dimensional deformation of dense granular flow and simulated the kinematics behaviour of force chain during buckling. Another study on force chain dynamically have been conducted by Wang et al.[60]. They modeled the Taylor-Couette shear by using the DEM method to evaluate the mechanical properties and the changing force in the network of a granular flow corresponding to the particle's friction coefficient, rotational speed and particle size. In addition to the packing particles, DEM has been developed for particle flows simulation. On this matter, considerable research attention has been devoted to describe the granular flow behaviour by means of DEM simulations. For instance, Zhang et al, Hanes et al, Teufelsbauer et al, Lo et al and Zhou et al [61-66] describe the mechanical and dynamic behaviour of the dry granular flow on an inclined plane using DEM method. Moreover, DEM simulation has been extensively used to model dry granular flows in hoppers [67-72] and mixtures [73-77].

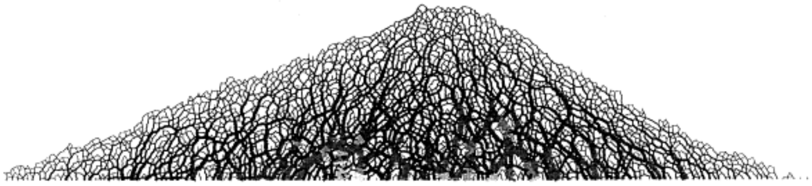

Figure 1-7 Force network of a heap constructed on a flat bottom [57].

DEM is more attractive comparing to continuum methods because particles' properties such as size and density which are specific to each individual particle can be directly taken into account in the model. Furthermore, the governing equations for the particle's interactions are influenced by materials properties such as the friction coefficient, Young's modulus and Poisson ratio. As a result, compared to continuum methods, DEM requires fewer assumptions [78]. Furthermore, depending on the length and time scale of the fluid flow, DEM can be combined with continuum methods to model particle-fluid flows in what is generally referred to as CFD-DEM. Hence, DEM has been coupled with different continuum methods such as large eddy simulation (LES), direct numerical simulation (DNS), lattice-Boltzman (LB), Smoothed Particle Hydrodynamics (SPH) and other Computational Fluid Dynamic(CFD) approaches [39].

1.2.2.3 CFD-DEM models

CFD-DEM has received more attention in engineering applications owing to its computational convenience in comparison with the other methods [36]. In this method, DEM, as a discrete method can provide information of particles individually and CFD, as continuum method, can describe the dynamic of the liquid phase by solving the locally averaged Navier–Stokes equations. The general scheme of CFD-DEM coupling presented in CFD-DEM studies is the DEM method provides the position and velocity of particles for CFD and then CFD calculates the porosity based on the position of particles in each computational cell. Then, CFD evaluates the drag force applied on each particle and provides the fluid force on each particle so that the DEM can calculate the position and velocity for the next time step. However, the schemes used to evaluate the particle-fluid interactions are different depending on the different length scales [36].

The governing equations in CFD-DEM were developed in two different approaches: resolved and unresolved CFD-DEM. The resolved CFD-DEM is suitable to those cases in which the particles are significantly larger than the fluid grid. Hence in this approach each particle must cover at least 8 computational grids [79]. This approach is based on Direct Numerical Simulations (DNS) and the particle phase is solved by a fictitious domain method. On the other hand, unresolved CFD-DEM is proposed for those cases where the particles are smaller than the fluid grid. Figure 1-8 shows a comparison of resolved and unresolved CFD-DEM [80, 81].

(a) Unresolved CFD-DEM

(b) Resolved CFD-DEM

Figure 1-8 Schematic of the CFD grid size and particle size in two CFD-DEM approaches

Coupling of DEM with CFD was first introduced by Tsuji et al in 1993 [78] and then many authors extended and developed this method for different purposes. and then many authors extended and developed this method for different purposes. Numerous studies of CFD-DEM coupling have been focused on the simulation of fluidized bed (gas/liquid-solid flow) reactors. In fluidized bed systems, gas flows rising from the bed of particles and particles motion have complex flow pattern as depicted in (Figure 1-9).

On this research area, numerous studies used CFD-DEM to model fluidized bed [78, 82-92]. Moreover, CFD-DEM has been widely used to model pneumatic conveying, pipeline flow, hydrocyclones, horizontal and vertical conveying which are widely present in chemical and agricultural processes [30, 39].

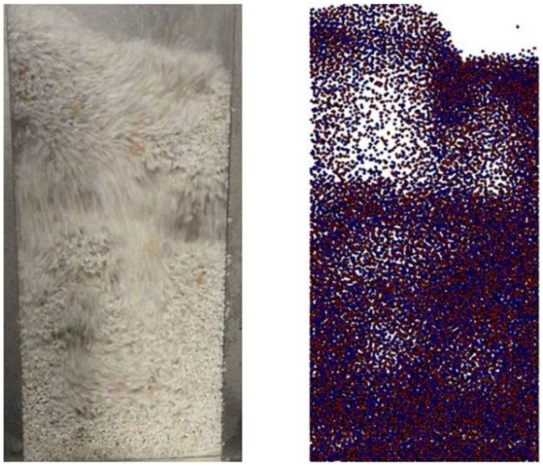

Figure 1-9 Comparing of a snapshot of simulation(right) and the experimental result(left) for a fluidized bed [91].

Afterward, CFD-DEM was extensively developed to study in other fields. For example in civil and geotechnical engineering, investigation of particle-fluid and particle- particle interaction of soils has been recently studied by coupling CFD-DEM, since understanding soil behavior plays an important role to mitigate and predict various geotechnical risks [93]. For this purpose, Zhao et al. developed a CFD-DEM model to study the features of a sandpile formed by a hopper flow in both dry and saturated cases to understand the complex particle-fluid interactions[93]. In another CFD-DEM study, [94] analyzed submerged debris flows using ESySS-particle code as a discrete tool and

OpenFOAM as a continuum method. Another example of implantation of CFD_DEM in geotechnical studies was done by Chen et al., [95] They studied solid-particle interaction in upward seepage gradient condition using two open source codes: OpenFOAM for modeling the fluid dynamics and YADE-OpenDEM for the particle's motion.

One of the challenges in modelling multiphase granular flows in industrial and environmental applications is simulating the free surface between water and air. Many studies have focused on developing different methods able to capture the free surface interface. Two popular methods are the Level Set (LS) [96] and the Volume of Fluid method (VOF) [97]. In [98], the CFD-DEM coupling was used to model landslide motions and the impulse waves generated by the landslides. In this study, the Immersed Boundary Method (IBM) was used to model the fluid-landslide interaction and the Conservative Level Set (CLS) was implemented to capture the free surface [98]. According to [99], it is better to implement the VOF method to capture the interface phase when using unresolved CFD-DEM coupling. For this reason, many multiphase granular flows have been modeled using integration VOF in CFD-DEM model. For instance, Jing et al. [100] combined VOF into CFD-DEM to model free surface multi-size granular flows and they developed a porous sphere method for cases with a wider range of particle size. Wu et al, [99] also developed a VOF-DEM model to simulate a turbulent free surface. They successfully applied their model for the solid-liquid mixing in stirred tanks. In another study conducted by Sun [101], a DEM-VOF model is propped for three-dimensional simulation of multiphase granular flows in complex geometries. A more recent study on the dynamics of granular driven by flow conducted by Zhao et al. used VOF in CFD-DEM to model landslides [102]. Another example of VOF implemented in CFD_DEM for landslides is done by Shan et al [103], where they simulated gravity-driven granular flow on an inclined plane and falling into water successfully.

1.3 Objectives and originality

The previous part highlighted the facts that: (1) understanding granular flows play a significant role in the prediction of complex behavior of various destructive granular flows in the form of debris flows; (2) Despite past experimental and numerical simulations that have been conducted on the dynamic behavior of granular flow, there is a lack of a comprehensive model to offer a realistic description of the motion of particles; (3) Particularly for DEM modelling of granular flows, the coupling DEM with a fluid simulation model (for multiphase cases) is still an open problem; (4) Finally for the case of multiphase gravity-driven granular slides and collapses application and parametrization of DEM technique has been limited to only few studies.

Therefore, the global objective of this research is to develop a CFD-DEM hybrid model for the study of multiphase gravity driven dense granular flows and use it for study of sub-aerial and submerged granular slides and collapses. The specific objectives are:

- Implement, calibrate and validate a DEM model (based on an open-source DEM code) for gravity-driven subaerial granular flow.
- Develop, calibrate and validate a hybrid CFD-DEM model, by coupling the developed DEM model with an open-source CFD code.
- Apply the model for simulation and study of the sub-aerial and submerged granular slides and collapse.

The contribution of this research in the advancement of knowledge will be in two aspects:

1) This study provides a better understanding of the physics of granular flow for applications cases of sub-aerial and submerged granular collapse and landslides.
2) Moreover, since the CFD-DEM framework has the capability to model the interaction of the fluid-particles and particle-particle with a very high degree of accuracy, our models can be used as a benchmark for parametrization and validation the scalable continuum-based models.

1.4 Thesis structure

This thesis has five chapters.

- Chapter 1: Present the objectives of this study and the literate review.
- Chapter 2: Provides the validation and calibration of a single-phase Discrete Element Method (DEM) model for simulate dry granular collapse and landslide, based on an opensource DEM code called LIGGGHTS. This chapter addresses the objective 1.

- Chapter 3: Presents and validates the free-surface hydrodynamic model of this study, which is based on the opensource code OpenFOAM. This chapter has been included to validate the CFD model before combining it with DEM.
- Chapter 4: Focuses on combining LIGGGHTS and OpenFOAM through a CFD-DEM framework, to develop a hybrid model, and validation and applying the model for simulation of multiphase (submerged) granular collapse and landslide. This chapter addresses the objectives 2 and 3.
- Chapter 5: Presents the conclusions of this study.

CHAPTER 2 VALIDATING A SINGLE-PHASE DEM MODEL

In this chapter the particle-particle interaction in a single -phase gravity-driven granular flow is investigated using a Lagrangian method named Discrete Element Method. First, the methodology and the governing equations are explained. Then the open source (LIGGGHTS) used in this study to simulate the single-phase granular flow is introduced. Finally, two granular flow cases are modeled and validated with the experimental data conducted in the laboratory of hydraulics at École Polytechnique of Montreal by Prof. Ahmad Shakibaeinia.

2.1 General overview of Discrete Element Method (DEM):

In the past, experimental studies were carried out to investigate the behavior of granular materials. Nowadays, due to increasing computer performance, numerical simulations start to play a crucial role in understanding and investigating the granular material's behavior more effectively [104]. To investigate the physical phenomena of granular flow two different methods have been proposed:

1) Continuum- based method: the granular flow is considered as a fluid flow and the behavior of individual particles are overlooked.
2) Discrete methods: interactions between particles are considered.

Discrete Element Method (DEM) is the most common discrete method and was first proposed by Cundall and Strack (1979). Two types of DEMs have been developed: hard-particle method and the soft-particle method. In a hard particle approach, the collision happens instantaneously, and the particles are assumed perfectly rigid. This kind of approach is reliable in rapid granular. In contrast, in the soft-particle method, the particles are allowed to interpenetrate each other, and the overlap is used to calculate the contact forces between particles. The discrete element method discussed in this study is the soft-particle model which is widely applied in granular simulation [36].

Linear models are the simplest models and are first proposed by Cundall and Strack (1979) [37] . The linear spring-dashpot model is the most common model in which the spring represents the elastic deformation and the dashpot represents the damping effects. After the other more complex ones have been introduced. For example, nonlinear model proposed by Hertz (1882) considers a nonlinear relationship between the normal forces and the normal overlap. Recently various studies have been conducted on more complex models to take into account other effects such as the plastic deformation and the rolling friction torque. The complexity of the models increases as the shape of particles is less spherical. In this regard, many models have been proposed for non-spherical shapes [36]. Due to the intrinsic complexity of DEM, this research area is still active and is directed toward understanding and modeling particle interactions more accurately.

2.2 Governing equations

The main idea behind the DEM method is to find the displacement and the new position of each particle from the acceleration caused by the contact forces produced by interactions with adjacent particles, walls, or with the surrounding fluid. The Newton's second law can be used to model the motion of each particle. The governing equations for the rotational and translational motion of a particle *i* with the mass m_i and the mass moment of inertia $I_i$can be written as:

$$I_i \frac{d\boldsymbol{\omega}_{\mathbf{i}}}{dt} = \sum_j (\mathbf{M}_{c,ij} + \mathbf{M}_{r,ij}) + \sum_w (\mathbf{M}_{c,iw} + \mathbf{M}_{r,iw})$$

Eq. 2-1

$$m_i \frac{d^2\mathbf{x}_i}{dt^2} = \mathbf{F}_{taotal}$$

Eq. 2-2

where, ω_i is the angular velocity of particle i, $\mathbf{M}_{c,ij}$ and $\mathbf{M}_{c,ij}$ are the contact torque and rolling friction torque respectively between particle *i* and particle j. $\mathbf{M}_{c,iw}$ and $\mathbf{M}_{r,iw}$ are defined as the contact torque between particle *i* and the wall. The total forces acting on each particle is given by:

$$\mathbf{F}_{total} = \underset{\text{contact force}}{\sum_j \mathbf{F}_{ij}^{c}} + \underbrace{\sum_k \mathbf{F}_{ik}^{nc}}_{\substack{\text{Long range forces} \\ \text{particle-particle}}} + \underset{\text{fluid forces}}{\mathbf{F}_i^{f}} + \underset{\text{body forces}}{\mathbf{F}_i^{b}}$$

Eq. 2-3

where fluid forces can be drag forces and long-range force can be cohesion forces and electrostatic forces depending on the kind of system. Body forces also can be the gravitational force which applied on the particle's body. Only on the contact force, which is the core of DEM method, is explained in this section. The contact force between particles is consisted of two components and is given as:

$$\mathbf{F}_{contact,ij} = \mathbf{F}_{normal\ contact,ij} + \mathbf{F}_{tangential,ij}$$

Eq. 2-4

The contact forces are based on a widely-used the soft-particle approach that assumes a small overlap between contacting particles. As mentioned earlier, one of the most common contact forces model is the spring-dashpot model. This model includes elastic and dissipative forces and can be calculated as:

$$\boldsymbol{F}_{contact\ i,j} = \left(K_{n,ij}\left\|\boldsymbol{\delta}_{n,ij}\right\|^{a}\boldsymbol{\delta}_{n,ij}\right) + \left(\gamma_{n,ij}\left\|\boldsymbol{\delta}_{n,ij}\right\|^{b}\dot{\boldsymbol{\delta}}_{n,ij}\right) + \left(K_{t,ij}\left\|\boldsymbol{\delta}_{n,ij}\right\|^{c}\boldsymbol{\delta}_{t,ij}\right) + \left(\gamma_{t,ij}\left\|\boldsymbol{\delta}_{n,ij}\right\|^{d}\dot{\boldsymbol{\delta}}_{t,ij}\right) \qquad \text{Eq. 2-5}$$

where, $\boldsymbol{\delta}_{t,ij}$ and $\boldsymbol{\delta}_{n,ij}$ are the tangential overlaps and normal of particles, $K_{n,ij}$ and $K_{t,ij}$ are the normal and tangential elastic stiffness coefficients, $\gamma_{n,ij}$ and $\gamma_{t,ij}$ are the normal and tangential damping coefficients, $\dot{\boldsymbol{\delta}}_{n,ij}$ and $\dot{\boldsymbol{\delta}}_{t,ij}$ are the normal and tangential relative velocities of particles, and a, b and c are constants. As Eq. 2-5 shows, the contact force is a combination of the repulsion and dissipation terms. Many models have been proposed for Eq. 2-4 and the most well-known model is the linear spring-dashpot model. In this model, the relationship between the contact force and the overlap is assumed to be linear. Many non-linear models have been proposed to calculate contact forces. These models, compared to the linear models, are more complex [105].

2.2.1 Normal and tangential overlaps:

To calculate the normal overlaps, first the normal contact vector **n** is defined. The normal contact vector for spherical particles is the unit vector which connects to center of mass of particles *i* and *j* and is defined as:

$$\mathbf{n} = \frac{\mathbf{x}_i - \mathbf{x}_j}{\left\|\mathbf{x}_i - \mathbf{x}_j\right\|} \qquad \text{Eq. 2-6}$$

where $\mathbf{x}_i$ and $\mathbf{x}_j$ are the position vectors of the center of particle *i* and *j* respectively. As Figure 2-1 shows, the normal overlap is the overlap of particles *i* and *j* in the direction of the normal vector and is given as:

$$\boldsymbol{\delta}_{n,ij} = \delta_{n,ij}\mathbf{n} = \left(\left(r_i + r_j\right) - \left\|\mathbf{x}_i - \mathbf{x}_j\right\|\right)\mathbf{n} \qquad \text{Eq. 2-7}$$

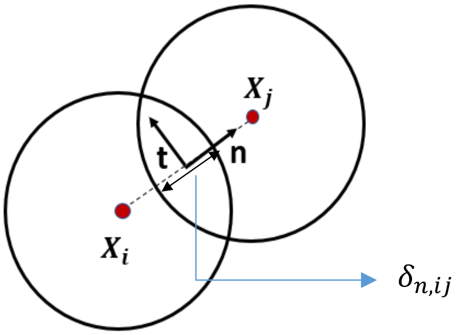

Figure 2-1 The overlap of between two particles

where, r_i and r_j are the radiuses of particles i and j respectively. Then when the particles' distance is smaller than the summation of their radiuses, in other words when $\delta_{n,ij} > 0$, there is collision. The tangential overlap vector is orthogonal to the normal unit vector as Figure 2-1 shows. The tangential overlap vector in 3-D cases is a plane perpendicular to the normal plane. As a result, in 3-D cases it is impossible to define a tangential unit vector because there are countless tangential unit vectors which are perpendicular to the unit normal vector. To overcome this problem, the tangential overlap $\boldsymbol{\delta}_{t,ij}$is thus defined as:

$$\boldsymbol{\delta}_{t,ij} = -\int_{t=t_{c,ij}}^{t} \boldsymbol{\upsilon}_{t,ij}\ dt \qquad \text{Eq. 2-8}$$

where $\boldsymbol{\upsilon}_{t,ij}$ is the tangential relative velocity and can be calculated as:

$$\boldsymbol{\upsilon}_{t,ij} = \boldsymbol{\upsilon}_{ij} - \boldsymbol{\upsilon}_{n,ij} \qquad \text{Eq. 2-9}$$

where, $\boldsymbol{\upsilon}_{ij}$ is the relative velocity. Hence, the time derivatives of the normal and tangential overlap can be written as:

$$\dot{\boldsymbol{\delta}}_{n,ij} = -\boldsymbol{\nu}_{n,ij} \qquad \text{Eq. 2-10}$$

$$\dot{\boldsymbol{\delta}}_{t,ij} = -\boldsymbol{\nu}_{t,ij} \qquad \text{Eq. 2-11}$$

2.2.2 Normal contact forces

Different normal contact forces have been proposed in the literature which can be categorized into main groups: linear visco-elastic models, non-linear visco-elastic models and hysteretic models [105].

The linear spring and a dashpot and the normal force are calculated as:

$$\mathbf{f}^{c}_{n,ij} = K_{n,ij}\boldsymbol{\delta}_{n,ij} + \gamma_{n,ij}\dot{\boldsymbol{\delta}}_{n,ij} \qquad \text{Eq. 2-12}$$

$K_{n,ij}$ can be obtained as [105]:

$$K_{n,ij} = 1.2024(E^{2}_{ij}\sqrt{m_{ij}}\, r_{ij}\left\|v_{n,ij}\right\|)^{2/5} \qquad \text{Eq. 2-13}$$

where E_{ij}, m_{ij},r_{ij} and υ_{ij} are Young's modulus, mass, radius and Poisson ratio in the collision between particles i and j which can be calculated as:

$$E_{ij} = \left(\frac{1-v_i^2}{E_i} + \frac{1-v_j^2}{E_j}\right)^{-1} \qquad \text{Eq. 2-14}$$

$$r_{ij} = \left(\frac{1}{r_i} + \frac{1}{r_j}\right)^{-1} \qquad \text{Eq. 2-15}$$

$$m_{ij} = \left(\frac{1}{m_i} + \frac{1}{m_j}\right)^{-1} \qquad \text{Eq. 2-16}$$

where the subscribes indicate the properties of particles *i* and *j*. The normal damping coefficient can also be calculated as [105]:

$$\gamma_{n,ij} = \frac{-2\sqrt{m_{ij}\ k_{n,ij}}ln\, e_n}{\sqrt{(ln e_n)^2+\pi^2}} \qquad \text{Eq. 2-17}$$

where, e_n, obtained experimentally, is the coefficient of normal energy restitution.

Another model, based on the nonlinear Hertz's elastic contact theory, can be used to represent the normal force as:

$$\mathbf{f}^{c}_{n,ij} = K_{n,ij}\left\|\boldsymbol{\delta}_{n,ij}\right\|^{1/2}\boldsymbol{\delta}_{n,ij} \qquad \text{Eq. 2-18}$$

where the normal spring stiffness is given by:

$$K_{n,ij} = \frac{4}{3}E_{ij}\sqrt{r_{ij}} \qquad \text{Eq. 2-19}$$

Finally, the third group is a combination of a linear dashpot and a non-linear elastic normal force [105].

2.2.3 Tangential contact forces

Tangential contact force models are also developed in three models including linear visco-elastic models, non-linear visco-elastic models and hysteretic models. Both linear and non-linear tangential models can be written as:

$$\mathbf{f}_{t,ij} = -K_{t,ij}\boldsymbol{\delta}_{t,ij} - \gamma_{t,ij}\dot{\boldsymbol{\delta}}_{t,ij} \qquad \text{Eq. 2-20}$$

The difference between the linear and non-linear tangential models is calculating the tangential stiffness coefficient. In the linear models, the value of $K_{t,ij}$ is constant, while, this value in the non-linear is calculated as:

$$K_{t,ij} = 8G_{ij}\sqrt{r_{ij}} \qquad \text{Eq. 2-21}$$

where G_{ij} is the shear modulus which can be written as:

$$G_{ij} = (\frac{2-\nu_i}{G_i} + \frac{2-\nu_j}{G_j})^{-1} \qquad \text{Eq. 2-22}$$

The hysteric tangential models employ a different stiffness in phases of collision (loading and unloading).

All of these tangential forces are confined by the coulomb limit:

$$f_{t,ij} \leq \mu_f f_{n,ij} \qquad \text{Eq. 2-23}$$

where μ_f is the friction coefficient [105].

2.3 LIGGGHTS

LIGGGHTS [106] is a free opensource code for particle simulation based on Discrete Element Method. It is an acronym for ‘LAMMPS [107] Improved for General Granular and Granular-heat transfer simulation’. LIGGGHTS is an improved version of LAMMPS (Large-scale Atomic/Molecular Massively Parallel Simulation) which is a molecular dynamics software simulation. This improvement includes additional features such as Hertz/Hooke pair styles, cohesion and rolling friction forces, and heat conduction between particles. This software can be used to simulate particles at the atomic, meso or continuum scale. LIGGGHTS is written in C++ and offers the option to run in parallel. Two contact models, linear (Hook) and non-linear (Hertz), are available in LIGGGHTS to simulate granular particles with efficient algorithms for detecting and calculating the interaction forces. In this study, Hertz's model is used to calculate the contact forces in which the $K_n, K_t, \gamma_n, \gamma_t$ coefficients are obtained from material properties [108, 109].

$$K_n = \frac{4}{3} Y^* \sqrt{R^* \delta_n} \qquad \text{Eq. 2-24}$$

$$\gamma_n = -2\sqrt{\frac{5}{6}}\, \beta \sqrt{m^* s_n} \geq 0 \qquad \text{Eq. 2-25}$$

$$K_t = 8G^* \sqrt{\delta_n R^*} \qquad \text{Eq. 2-26}$$

$$\gamma_t = -2\sqrt{\frac{5}{6}}\, \beta \sqrt{m^* s_t} \geq 0 \qquad \text{Eq. 2-27}$$

The following equations are used for two particles in contact:

$$s_n = 2Y^* \sqrt{\delta_n R^*} \qquad \text{Eq. 2-28}$$

$$s_t = 8G^* \sqrt{\delta_n R^*} \qquad \text{Eq. 2-29}$$

$$\beta = \frac{\ln{(e)}}{\sqrt{ln^2}(e) + \pi^2} \qquad \text{Eq. 2-30}$$

$$\frac{1}{Y^*} = \frac{(1-\upsilon_1^2)}{Y_1} + \frac{(1-\upsilon_2^2)}{Y_2} \qquad \text{Eq. 2-31}$$

$$\frac{1}{G^*} = \frac{2(2+\upsilon_1)(1-\upsilon_1)}{Y_1} + \frac{2(2+\upsilon_2)(1-\upsilon_2)}{Y_2} \qquad \text{Eq. 2-32}$$

$$\frac{1}{R^*} = \frac{1}{R_1} + \frac{1}{R_2} \qquad \text{Eq. 2-33}$$

$$\frac{1}{m^*} = \frac{1}{m_1} + \frac{1}{m_2} \qquad \text{Eq. 2-34}$$

where, e is the coefficient of restitution, Y is Young's modulus, ν is Poisson ratio, m is the mass and R is the radius of a particle. In this method, tangential forces include shear and damping forces. The shear force is a history effect that considers the tangential overlap between the particles. The tangential force is limited by the Coulomb criterion: $F_t \leq \mu F_n$, where μ is the particle-particle friction coefficient. It is assumed that the contact surfaces are considered sticky when $F_t \leq \mu F_n$ and are considered slick when the Coulomb yield criterion is satisfied [109].

2.3.1 Reasons for choosing LIGGGHTS

LIGGGHTS as an Open source software has many advantages over the commercial software. First of all, it is free and can be downloaded without paying for a licence. The other major benefit is that the users have direct access to the source code of the package and thus can adjust additional features depending on their needs. In addition, open source codes are enhanced to run efficiently since several researchers worked together in improving every feature. Furthermore, LIGGHTS is an effective platform for DEM simulations due to the following characteristics [106]:

- Can run in parallel mode or using a single processor
- Can be coupled with other codes
- Complex geometries can be imported via STL file
- Moving mesh with different motion of schemes can be implemented
- Different contacts models are available

2.3.2 Numerical parameters in LIGGGHTS

Numerical parameters are set up in an input file in LIGGGHTS. The boundary of computational domain is first defined and the physical parameters such as Young's modulus, coefficient of restitution and friction are set. The coefficient friction can be set for different elements. For example, users can choose different coefficient friction for particle-particle, particle-walls and particle-STL file. The friction coefficient between particle and particle is based on the internal friction angle, φ , which the friction coefficient is obtained by $\mu = \tan\varphi$ [110].

Users can also choose the contact models. LIGGGHTS lets users define the minimum distance for detecting neighboring particles and generates neighbor lists to look for the nearby particles for detection collision. This enhances LIGGGHTS' computational efficiency [106].

2.4 DEM simulation using LIGGGHTS

In this part, numerical results obtained from the simulation of two granular flows cases, i.e. granular collapse and granular slide using DEM from the opensource code LIGGGHTS, are presented. The time evolution of the position and shape of granular collapse is compared with experimental results to validate the granular simulation.

2.4.1 Dry granular collapse:

Granular collapse is a test case which is widely used, due to its simplicity, to validate numerical models [34]. In this test case granular materials collapse under the gravity force. The configuration is based on the experiments conducted at the laboratory of hydraulic at Polytechnique Montreal, and includes a horizontal bed partially filled with glass beads to form a rectangular granular column of length l_0= 0.0975 m, height $h_0 = 0.049$ m in a rectangular tank as Figure 2-2 shows. The granular collapse is created by the removal of a gate with a speed of 1m/s. The material properties implemented in the simulation are shown in the Table 2-1.

Table 2-1 physical properties for the test case

Young's modulus (GPa)	Friction coefficient	Poisson ratio	Restitution coefficient	Density (kg/m^3)	Bulk density (kg/m^3)	Diameter (m)
60	0.4	0.45	0.9	2500	1535.993	0.0008

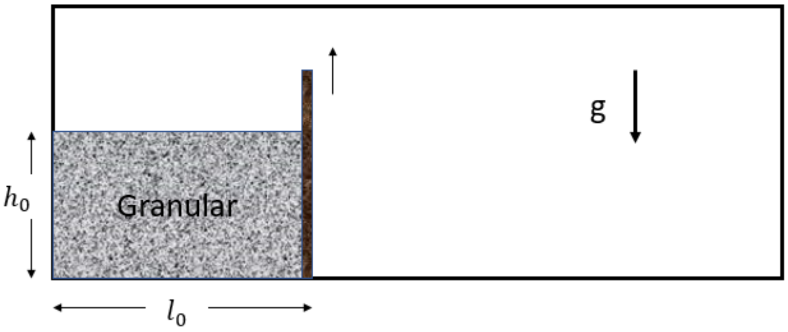

Figure 2-2 Initial configuration of the granular test case

A 3-dimensional simulation is conducted using open source LIGGGHTS. The initial compaction of the granular column is of 60% according to the bulk density. To create such an initial configuration, the required numbers of particles are set behind a physical gate. Then by removing the gate, the simulation starts. The coefficient friction is considered 0.4. It should be noted that to speed up the 3-D simulation, a smaller width was adopted in the simulation instead of the real width used in the experiment. In addition, the time step in the DEM method had to be chosen very small depends on material properties and the particle size. Since the time step in DEM is inversely proportional to the Young’s modulus, a smaller Young's modulus can decrease simulation time significantly. According to the literature, decreasing the elastic parameters does not produce a major change in the simulation results [9] Therefore, to speed up the simulation the Young's modulus used in this study is much smaller than the real value.

In order to better identify the evolution of the granular mass, the initial configuration is set by different color both in the experiment and the simulation.

To validate the simulation, the deposit configuration of granular collapse was compared with the experimental results.

Figure 2-3 shows a comparison of numerical and experimental snapshots of deposit configuration in different dimensionless time steps $T=t/\sqrt{(h_0/g)}$. The experimental snapshots are produced by a video recording with a Phorton Mini WX-100 high-speed camera and resolution of 2048× 2048 pixels. It should be noted that all experimental conducted in the Hydraulic laboratory of Polytechnique, have been obtained by this camera.

The comparison shows that there is relatively good agreement between simulation and experiment. The collapse starts when the upper part of the granular column undergoes a high vertical negative acceleration due to the removal of the gate.

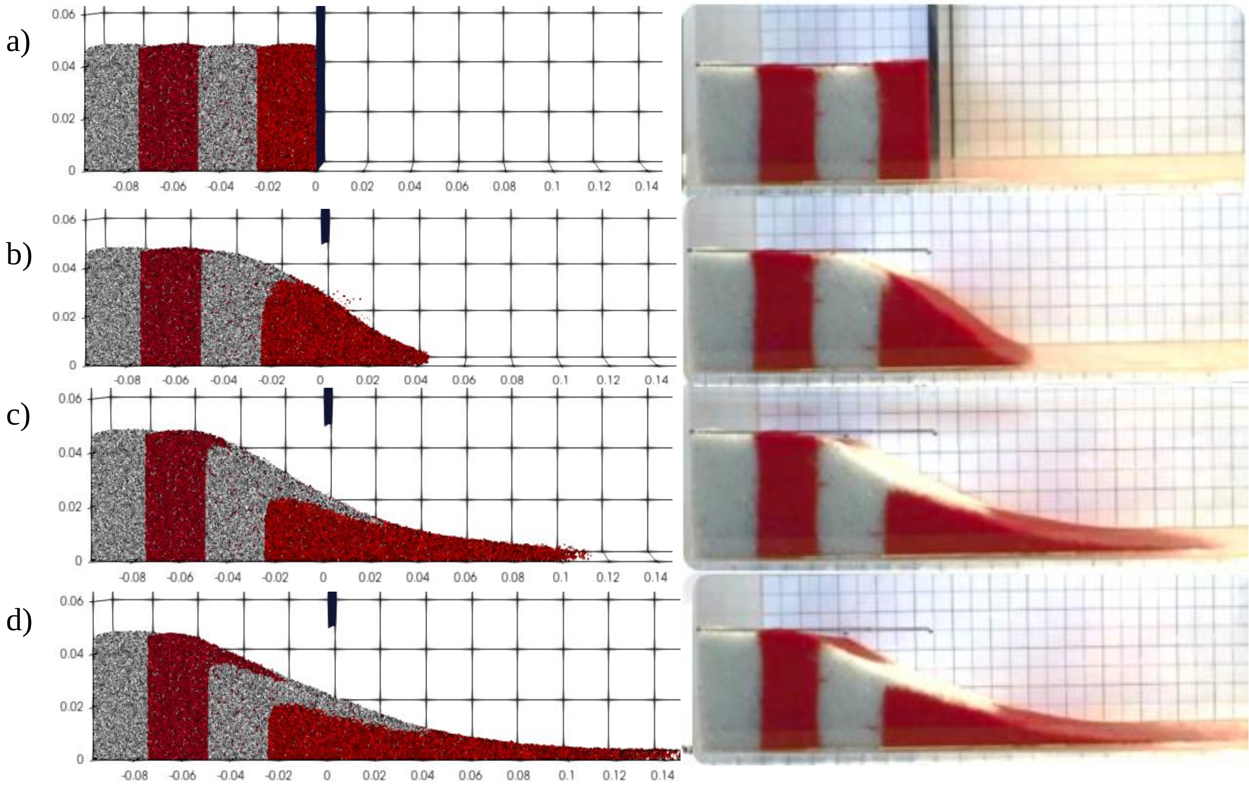

Figure 2-3 Numerical (left column) and experimental (right column) snapshots of deposit configuration for different dimensionless time steps (a) [T] =0, b) [T]=2, c) [T]=4, d) final)

In order to validate the simulation quantitively, the evolution of the dimensionless runout distance of the granular deposit is compared with the experimental results as depicted in Figure 2-4. In the numerical results, the position of the flow front is defined by the last particle. The particles which are dispersed in the domain and which are not touching the mass flow are disregarded. The comparison shows a good agreement between the results of LIGGGHTS and the experiment. The Root-Mean-Square Error (RMSE) calculated for this case is 0.006 m. Three regions can be seen in the runout distance as mentioned in the literature [34].The acceleration regime which occurs when[T]<1, the steady flow regime, and the deceleration regime which occurs when [T]>3. At times T=1, 2, 3, and 4, it can be seen that the runout distance predicted by LIGGGHTS is overestimated. This discrepancy between the numerical and experimental results can be explained by the fact that the friction coefficient, which plays an important role in the DEM method, is only estimated and might be different from the real friction coefficient. Moreover, in the simulation, all particles are perfectly spherical and have the same properties but, in reality, it can not be possible to have such a uniformity. Furthermore, small errors may be added by experimental measurements such as in the extraction of the runout distance. Experimental results are evaluated by the recorded videos and the motion of flow is described and measured by the video snapshots.

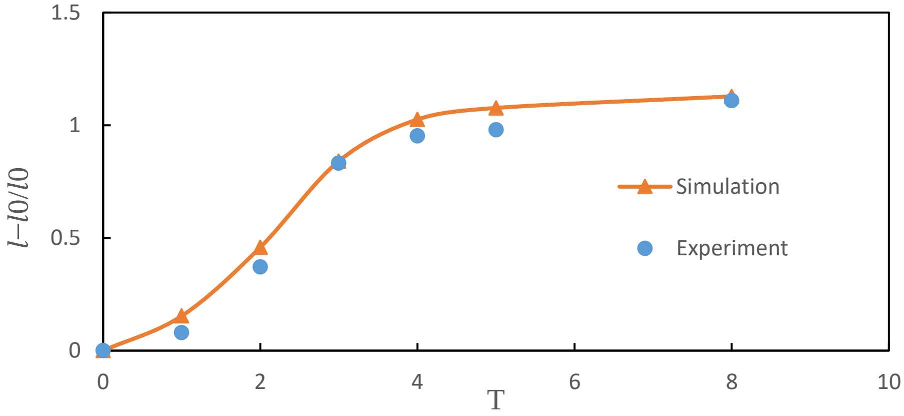

Figure 2-4 Simulation and experimental runout distance of dry granular collapse

Numerical surface profiles have also been compared with experimental surface profiles by digitizing the snapshots. In Figure 2-5, the comparison of surface profiles for different dimensionless time steps shows that there is good agreement between the simulation and the experimental results.

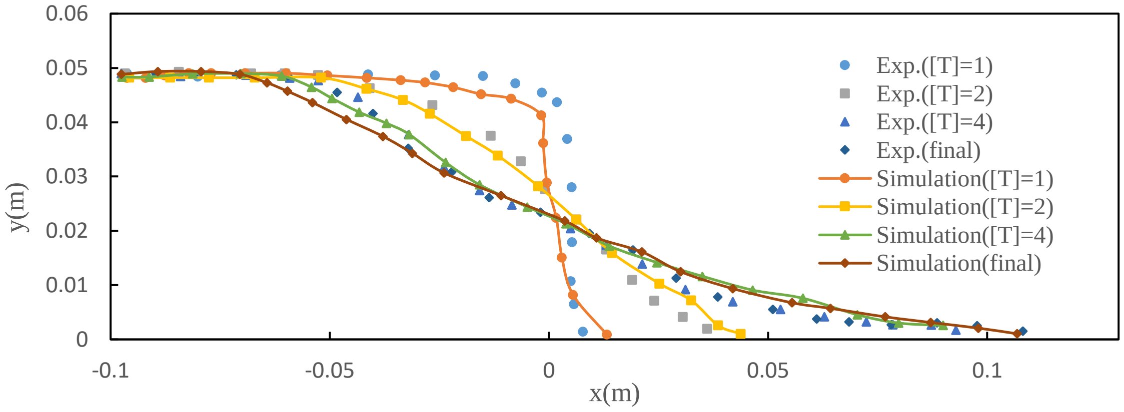

Figure 2-5 Comparison of Simulation and experimental surface profiles of dry granular collapse

After the validation of the simulation, the parameters and information of the granular collapse, which are hard to measure by experiment, have been extracted. Figure 2-6 shows the velocity field and vectors in different dimensionless time steps from which one can distinguish two zones in the granular collapse: the yielded zone in which the particles move and the non-yielded zone in which the particles velocity is zero or near-zero. The non-yielded zone is the trapezoidal blue zone that starts from the left corner of the mass granular to the concave yield line. In the yielded zone, particles velocity grows toward the profile’s surface and hence in the frontier face, particles have the maximum velocity. As time passes, the yielded zone becomes smaller and, at the final time step when the final profile forms, the yielded zone disappears totally.

DEM method also has the capacity to overcome the difficulties associated with experimental studies to evaluate the dynamic contact forces. As we mention in chapter 1, the force distribution of granular materials plays a significant role in the dynamic and static granular flows. DEM simulations enable to offer the information of the internal forces which provide us a better understanding of a granular system. In this study, we extracted normal force interaction between particles. Figure 2-7 shows how the normal force contact is distributed in the particles flow. The maximum normal force is happened at the bottom of the granular mass and at the surface this force has its minimum values.

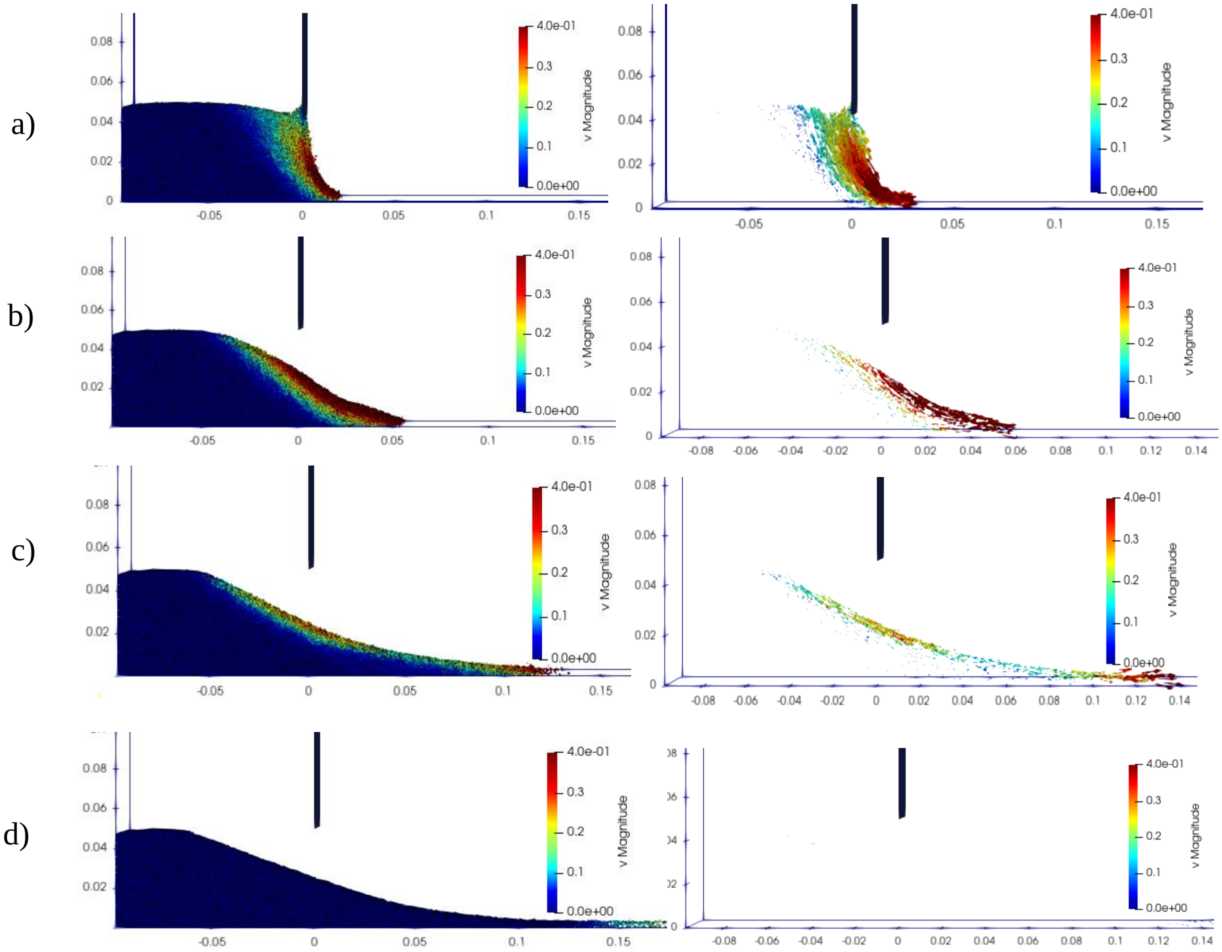

Figure 2-6 Velocity field and vector of granular collapse at different time steps (a) [T]=1, b) [T]=2, c) [T]=3, d)final)

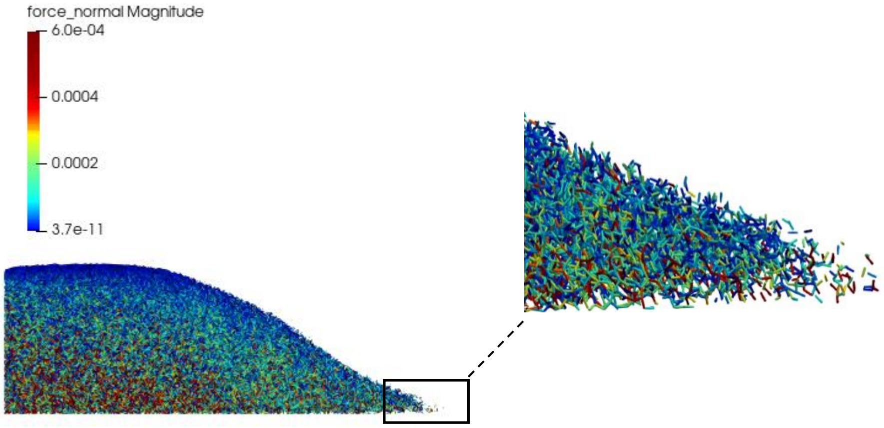

Figure 2-7 Normal force distribution of dry granular collapse at T=2

2.4.1.1 Sensitive analysis of the friction coefficient for the dry granular collapse

In DEM, the friction coefficient has more significant effects on the results compared to the other particles' properties such as coefficient of restitution and Young's modulus [111]. As the external friction coefficient factor depends on many factors such as surface material and roughness, it is associated with large uncertainty. Therefore, we must consider it as a calibration factor. LIGGGHTS offers the option to set different properties for different elements. The particle-particle friction coefficient, as discussed earlier, is based on the internal friction angle, φ , while this definition for particle-wall or particle-gate is meaningless. To calibrate the appropriate friction coefficient for particle-wall and particle-gate, a sensitive analysis has been done. To evaluate the effect of friction coefficient, three simulations have been carried out. Table 2-2 shows the parameters of these three simulations.

Table 2-2 Different friction coefficients for the dry granular collapse test

No. simulation	Friction coefficient for particle-particle	Friction coefficient for particle-walls	Friction coefficient for particle-gate
1	0.4	0.4	0.6
2	0.4	0.4	0.4
3	0.4	0.2	0.2
4	0.4	0.2	0.4

Figure 2-8 shows the runout distance obtained from the three simulations and from the experimental results. One can conclude from simulation 1 and simulation 2 that when the friction coefficient for particle-gate is higher, the numerical results is closer to the experimental results. Furthermore, it can be seen from simulations 2 and 4 that the particle-wall coefficient friction has a greater impact on the results. Thus, both the particle-wall friction coefficient and the particle-gate friction coefficient affect the numerical results. Consequently, the deposit of granular collapse strongly depends on the friction coefficient of particle-wall and particle-gate.

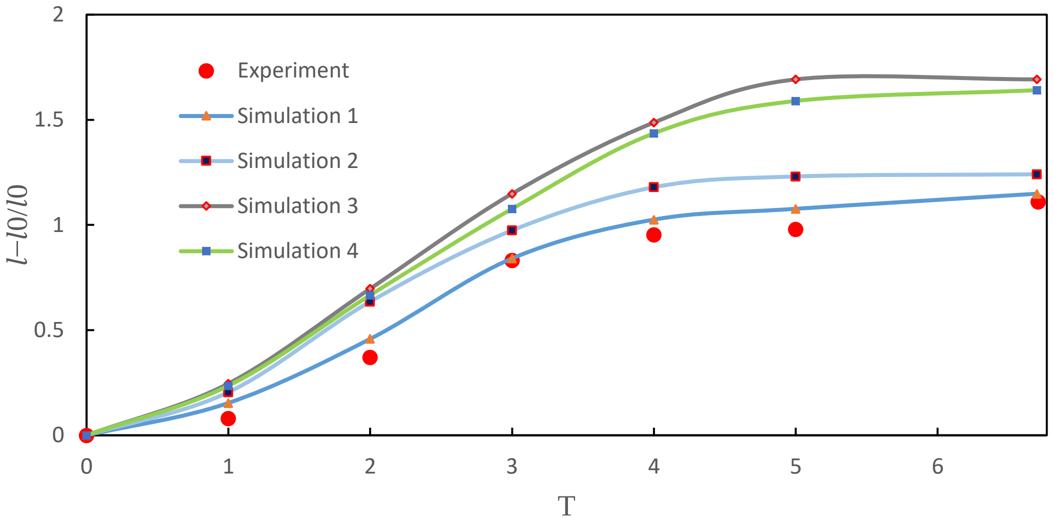

Figure 2-8 Comparing simulation with different friction coefficients with the experiment for the dry granular collapse

2.4.2 Dry granular slide

Granular slide test cases are common to model gravity driven granular materials and many studies have been focused on these testcases [24]. The computational domain of a landslide, as Figure shows, includes an inclined surface with an angle of 45 degrees. The granular mass with length, height and width of $l_g = 0.06\ m$, $h_g = 0.06\ m$ and $w_g = 0.15\ m$ respectively is set behind a gate. When the gate is removed at a speed of 1 m/s, the granular mass is released suddenly. The material properties are similar to the granular collapse test. These same properties were implemented in LIGGGHTS. To evaluate the DEM simulation, the runout distance and the surface profile of the granular mass were compared.

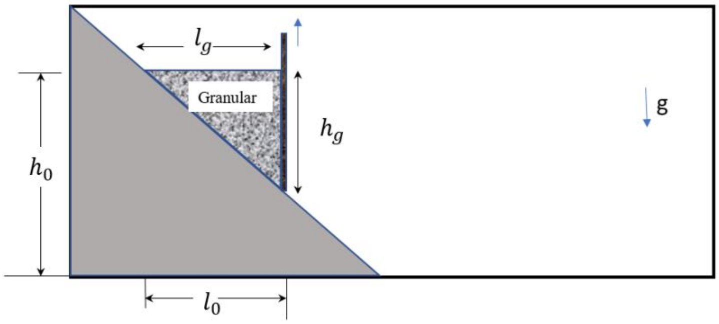

Figure 2-9 Initial configuration of the landslide test case

To evaluate the DEM simulation, like the granular collapse test case, we first compared simulation results for the flow configuration with the experimental snapshot in different dimensionless times ($[T]= t/\sqrt{(h_0/g)}$). As Figure 2-10 shows, one can conclude visually that simulation results and the experiment have the similar flow features.

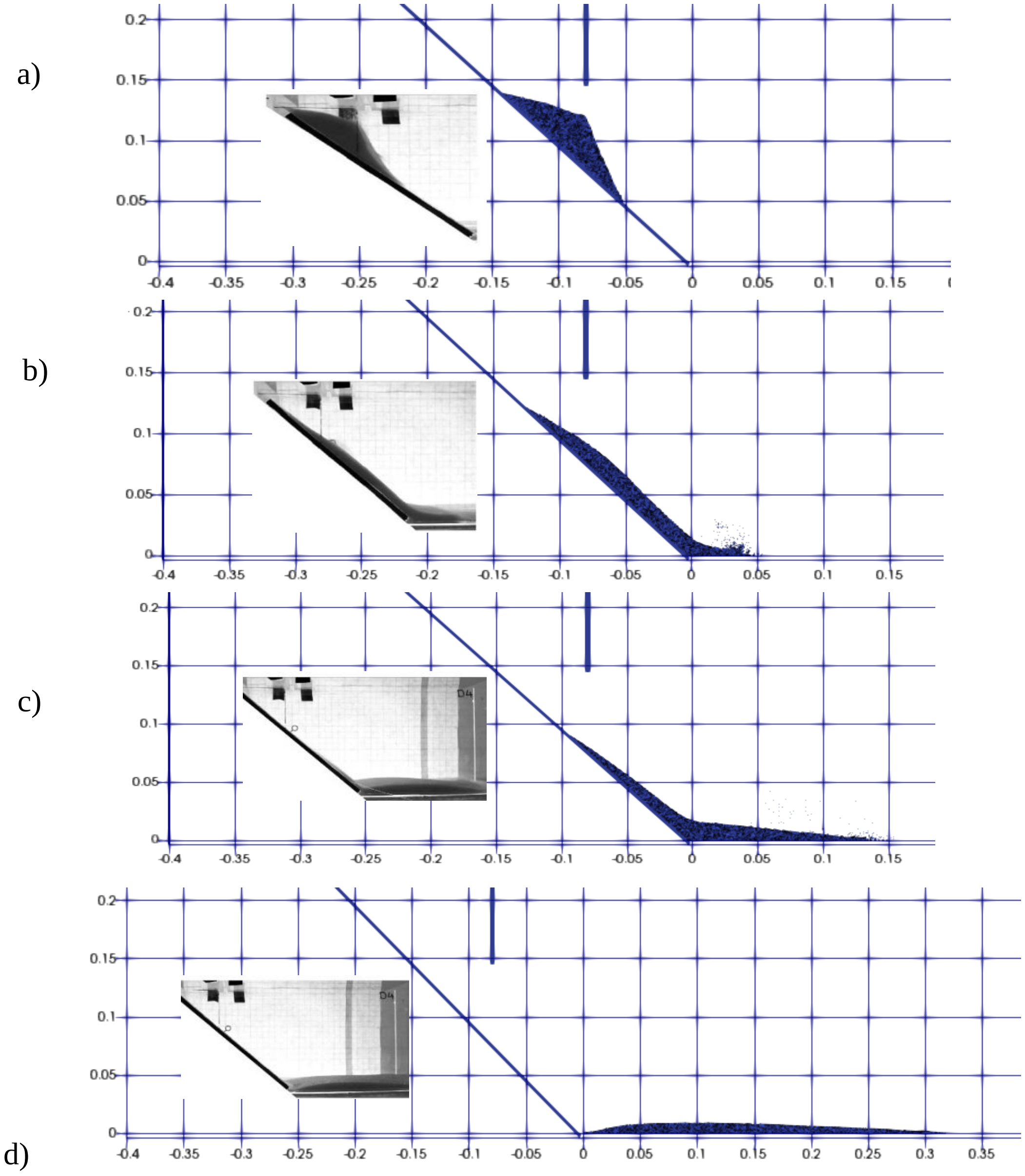

Figure 2-10 Numerical and experimental snapshots of granular flow on a inclined plane for different dimensionless time steps (a) [T] =1, b) [T] =2, c) [T] =3, d) final)

The granular motion is also quantified and validated by plotting the surface profiles in different dimensionless time steps in Figure 2-11 and Figure 2-12. The avalanche starts with the granular failure of mass in front and top. During the avalanche the granules materials are stretched along the slope by making a thin layer with a surface. Then the granular flow reaches to the slope toe and then the slow down and finally by forming a pile comes to rest. This was also observed in previous studies [24].

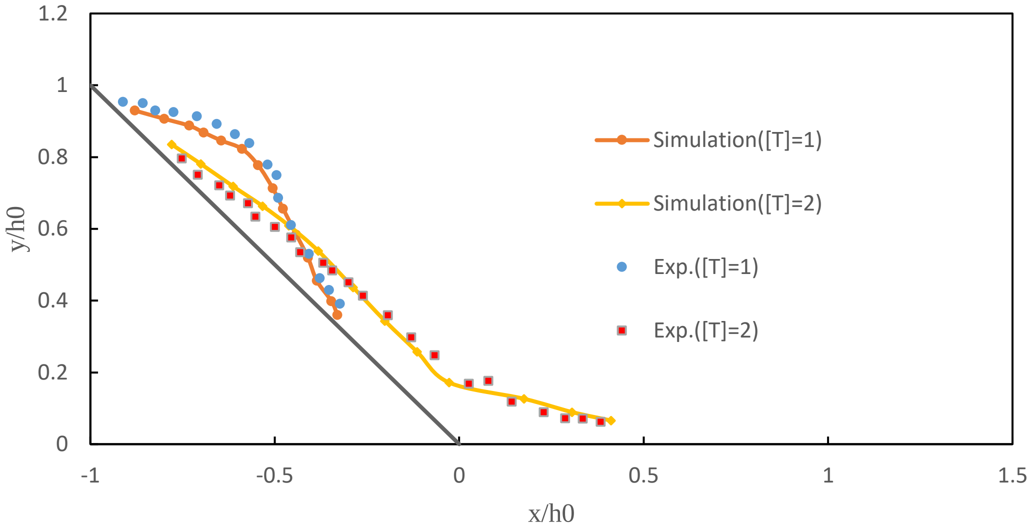

Figure 2-11 Comparison of Simulation and experimental surface profiles of dry granular slide ([T] = 1,2)

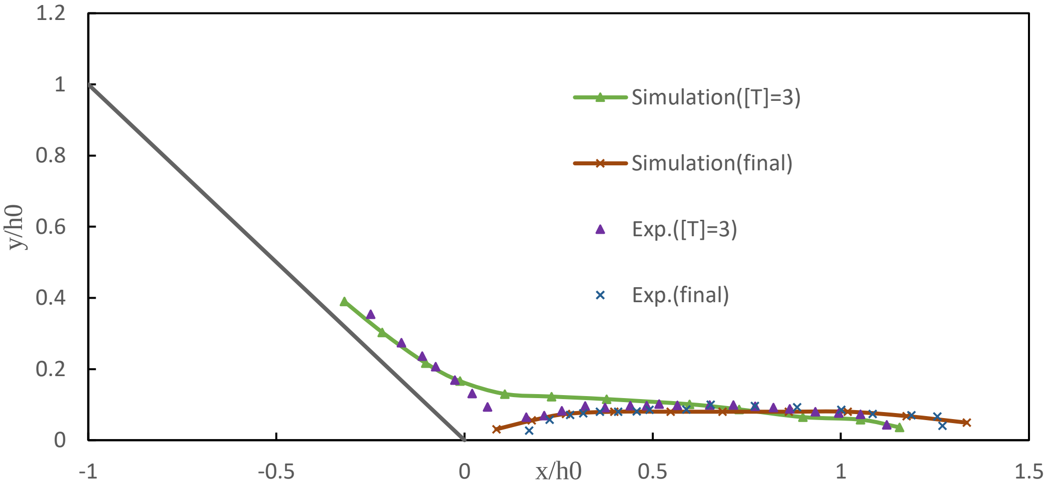

Figure 2-12 Comparison of Simulation and experimental surface profiles of dry granular slide([T]= 3 , final)

The granular motion is also quantified and validated by scheming the runout distance $(l - l_g)/l_g$ in different dimensionless time steps as depicted in Figure 2-13. Where l is the position of the last particle which still attached to the granular mass. The three regimes including accelerating([T] < 1.5), steady flow and decelerating regime([T] > 3.5) as observed in the previous studies [24, 35].

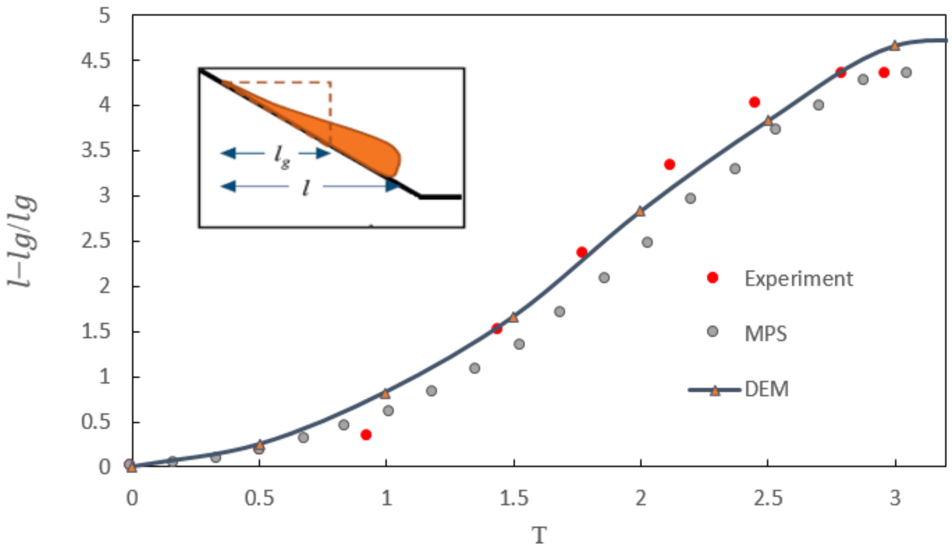

Figure 2-13 Simulation and experimental runout distance of the dry landslide

The DEM result for the runout distance is also compared with the results obtained from MPS method [35] with RMSE of 0.032 m in Figure 2.13. The RMSE of DEM method calculated for this case is 0.019 m. In order to explore the granular flow in the landside case, more quantitatively, we extracted the velocity filed and vector and the normal force distributions at different dimensionless time steps. Figure 2-13Figure 2-14 shows how the velocity filed and vector changing once the avalanche starts. The velocity field has the maximum values at the top and frontier of the granular mass. It was also interesting to extract the normal force distribution of the landslide test case. Figure 2-15 illustrates also the normal force distribution at two time steps. Similar to the granular collapse test case, the maximum values of the normal forces have been observed at the bottom of the granular mass and the minimum values can be observed at the surface of the granular mass.

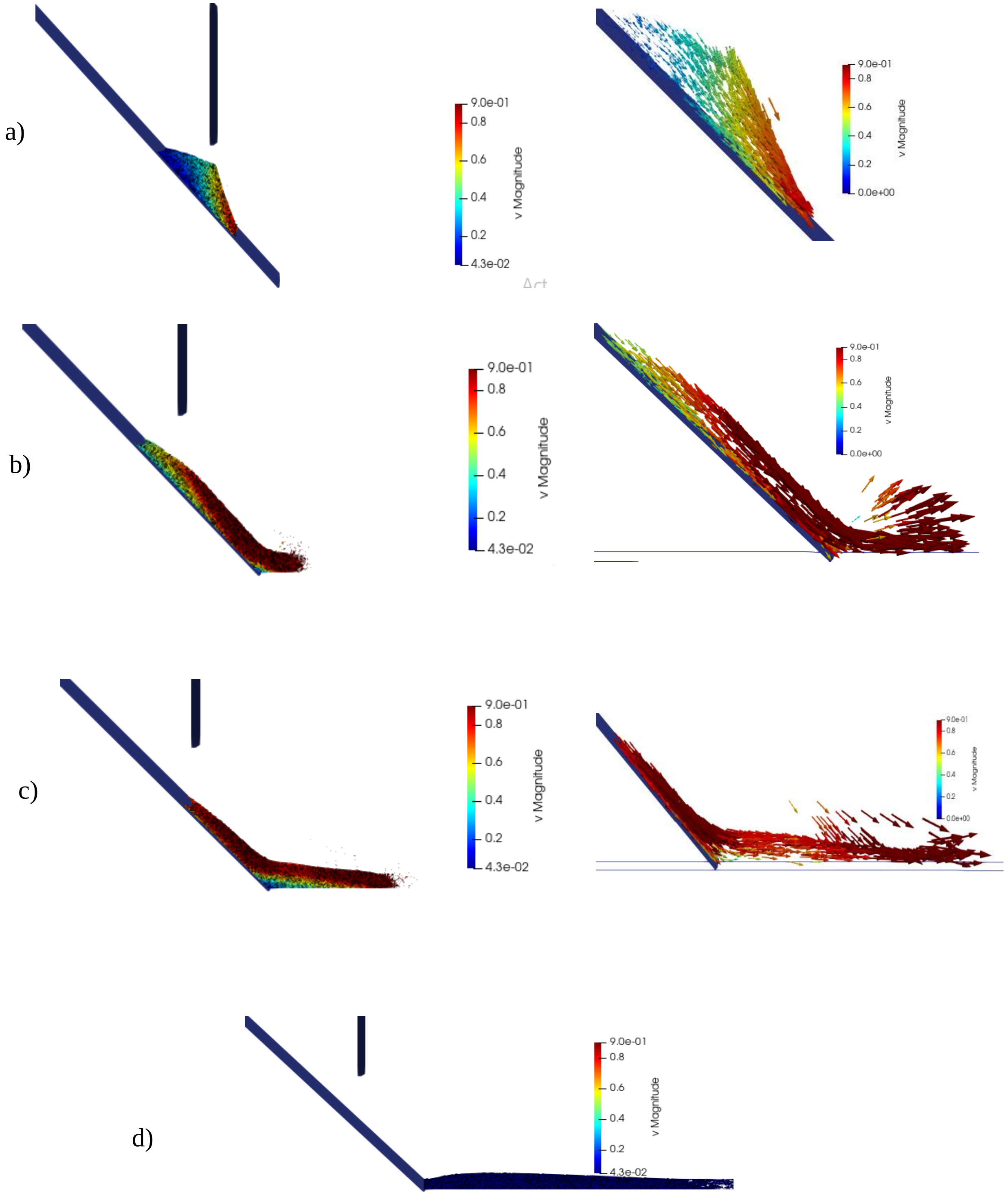

Figure 2-14 Velocity field and vector of the dry landslide at different time steps (a) [T]=1, b) [T]=2, c) [T]=3, d) final)

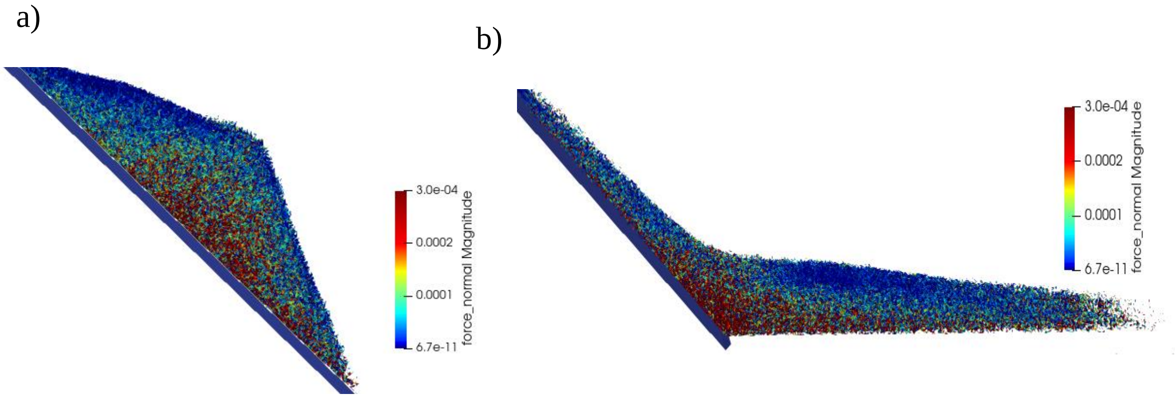

Figure 2-15 Normal force distribution at two time steps for the dry landslide (a) [T]=1, b) [T]=3)

2.5 Conclusion

In this chapter, we modeled single-phase granular flows by means of the DEM method. Two test cases simulations were performed by open source code LIGGGHTS as a C++ library of functions. We validated the simulations with the experimental and generally, the model demonstrated its capacities to describe the motion and behavior of granular flows in two test cases. Furthermore, DEM simulation provided us more information about the flow's dynamic. For example, in addition to the macroscopic information such as the velocity field and the position of particles individually, the internal forces can be extracted. This capacity of the DEM method provides us a better understanding of the granular flows. The sensitivity analysis of the friction coefficient for the dry test case indicated that the friction coefficient of particle-walls and particle-gate significantly affect the results as well as friction coefficient of particle-particle

CHAPTER 3 IMPLEMENTATION OF A FREE-SURFACE HYDRODYNAMIC MODEL BASED ON OPENFOAM

In this chapter, we present the calibration, parameterization and validation of the CFD model to show the accurateness of the hydrodynamic model before its coupling with DEM. The hydrodynamic model is based on an Eulerian scheme using the open source software package, OpenFoam [112]. First, we present the mathematical model of the two-phase immiscible, incompressible fluids, each having a constant viscosity based on the Navier-Stokes equations. Then the opensource OpenFoam is introduced. At the end we evaluate and validate the numerical model using a widely-used benchmark case, i.e. dam break. To validate the model, we used experimental results presented by Lobovský et al. [113].

3.1 CFD multiphase flow methodology

One of the most practical field of fluid dynamics is investigation of multiphase flows, where there is more than one phase of fluid. An important aspect of modelling the multiphase flows is the detection of the interfaces. In context of mesh-based Eulerian methods, several methods have been introduced in the literature to for capturing and tracking the interfaces. These methods can be categorized into two groups: 1) surface methods and 2) volume methods. Figure 3-1 shows the two methods. The interface in the surface method is characterized by marker points as depicted in Figure 3-1b). Front tracking method and level-set method are two common methods of surface methods which widely used to track the interface. However, there are some difficulties and limitation associated with this method. For example, this method would not be appropriate for those interfaces that include coalescence and breakup [114]. Also, flows with vorticities or significant deformation can not me modeled accurately with surface methods [114].

In the volume methods, Figure 3-1 a), an indicator function is needed to mark the fluids on either side of the interface. Different volume methods have been proposed to capture the interface

[114]. In this study, the Volume-of-fluid (VOF) approach, which is a popular method, is used to model the interface.

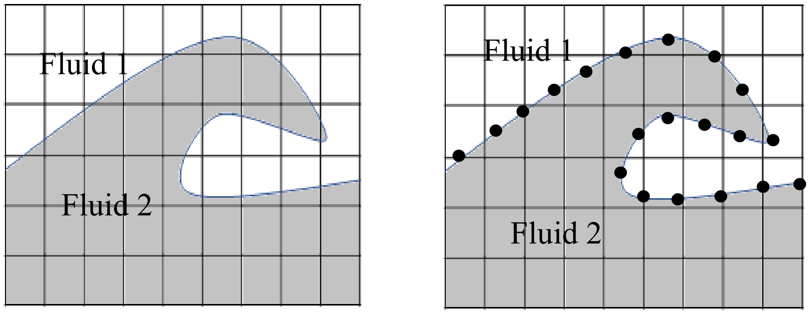

a) Volume method b) Surface method

Figure 3-1 Two methods representing interface

3.1.1 Volume of fluid (VOF)

This method was first introduced by Hirt and Nicholas [97] who started a new approach in multiphase flow simulation. In the VOF approach, the conservative equations have to take into account the surface tension force applied at the interface and the different material properties. In addition to the continuity and momentum equations, an additional equation is required to capture the interface. This equation uses the volume fraction as an indicator function to differentiate the interface between two phases. Based on the indicator function, the volume fraction, α, can have a value between 0 and 1. A unit value of α corresponds to a computational cell having a liquid phase and a zero value corresponds to a computational cell having a gaseous phase. The values between zero and one indicate the presence both phases in the cell, showing the interface (Figure 3-2).

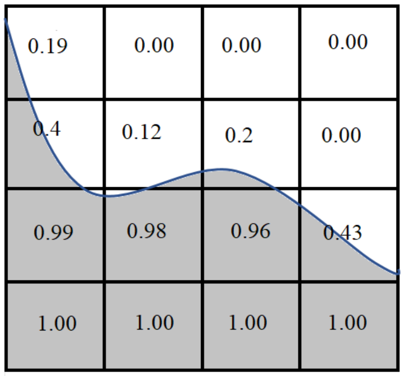

Figure 3-2 Volume fraction on computational cells near interface of two fluids

Therefore, in the volume of fluid method, the transportation equation for determining the relative volume fraction of two phases is solved concurrently with the continuity and momentum equations:

$$\nabla . \mathbf{U} = 0 \qquad \text{Eq. 3-1}$$

$$\frac{\partial \alpha}{\partial t} + \nabla . (\mathbf{U}\alpha) = 0 \qquad \text{Eq. 3-2}$$

$$\frac{\partial (\rho \mathbf{U})}{\partial t} + \nabla . (\rho \mathbf{U}\mathbf{U}) = -\nabla P + \nabla . \mathrm{T} + \rho \mathbf{f}_{\mathrm{b}} \qquad \text{Eq. 3-3}$$

where $\mathbf{U}$ is the velocity field communal by the two phases throughout the flow domain, P is the pressure, ρ is the density, $\mathbf{f}_b$ is the body force, α is volume fraction and **T** is the deviation viscous stress tensor which can be calculated as following:

$\mathbf{T} = 2\mu\mathbf{S} - 2\mu(\nabla . \mathbf{U})\,\mathbf{I}/3$, where μ is the dynamic viscosity, $\mathbf{S} = 0.5[\nabla \mathbf{U} + (\nabla \mathbf{U})^{\mathrm{T}}]$ and $\mathbf{I} \equiv \delta_{ij}$.

The physical properties of the interface region are considered as weighted averages based on the values of the volume fraction in this region. Thus, the local density and the local viscosity can be calculated as:

$$\rho = \rho_l \alpha + \rho_g (1 - \alpha) \qquad \text{Eq. 3-4}$$

$$\mu = \mu_l \alpha + \mu_g (1 - \alpha) \qquad \text{Eq. 3-5}$$

where ρ_l and ρ_g are the densities of the liquid and gas phases and μ_l and μ_g the dynamic viscosities [115, 116].

The conservation of the volume fraction is a critical issue for tracking the free surface in VOF method. In cases with high density ratios, small errors in volume fraction can cause significant errors in calculations of physical properties. Therefore, calculation of the volume fraction is very important to ensure accurate evaluation of the surface curvature. In order to address these difficulties, various attempts have been made. In this study, an implementation of a model formulated by OpenCFD is used instead of the conventional formula of the transport Eq. 3-2. In this model, an artificial compression term, like the one proposed by [116], adds to the volume fraction equation to yield a sharper interface resolution. In this model, for the liquid and gas phase, the volume fraction equations are solved separately. Thus, the volume fraction equations can be written as:

$$\frac{\partial \alpha}{\partial t} + \nabla.(\mathbf{U}_l \alpha) = 0 \qquad \text{Eq. 3-6}$$

$$\frac{\partial (1-\alpha)}{\partial t} + \nabla.\left[\mathbf{U}_g (1-\alpha)\right] = 0 \qquad \text{Eq. 3-7}$$

where, $\mathbf{U}_l$ and $\mathbf{U}_g$ are the liquid and gas phase velocity respectively. the contributions of the liquid and gas velocities to the development of the free surface is assumed to be relational to the corresponding phase fraction. The velocity of the effective fluid in a VOF model is defined as a weighted average. Therefore, the velocity can be considered as the velocity of the effective flow:

$$\mathbf{U} = \alpha \mathbf{U}_l + (1-\alpha)\mathbf{U}_g \qquad \text{Eq. 3-8}$$

By rearranging Eq. 3-6 the volume fraction equation can written as:

$$\frac{\partial \alpha}{\partial t} + \nabla.(\mathbf{U}\alpha) + \nabla.[\mathbf{U}_r \alpha (1-\alpha)] = 0 \qquad \text{Eq. 3-9}$$

where $\mathbf{U}_r = \mathbf{U}_l - \mathbf{U}_g$ is the relative velocity known as “compression velocity”. Eq. 3-9 includes an additional convectional term which leads to a higher interface resolution. It should be noted that this term acts only within the interface region and, therefore, it does not influence the outside of the interface region.

The surface tension at the interface region yields an additional pressure gradient and, consequently, a force which can be expressed as:

$$\mathbf{f}_\sigma = \sigma k \nabla \alpha \qquad \text{Eq. 3-10}$$

where σ is the surface tension and k is the mean curvature of the free surface obtained from the following expression:

$$k = -\nabla.\left(\frac{\nabla \alpha}{|\nabla \alpha|}\right) \qquad \text{Eq. 3-11}$$

Since the two fluids are considered to be Newtonian and incompressible, the strain rate tensor and the stress tensor have a linear relation and the discretization form can be expressed as:

$$\nabla.T = \mu[\nabla \mathbf{U} + (\nabla \mathbf{U})^T] = \nabla.(\mu \nabla \mathbf{U}) + (\nabla \mathbf{U}).\nabla \mu \qquad \text{Eq. 3-12}$$

In this VOF method, a modified pressure which disregards the hydrostatic pressure is used and it is defined as:

$$P_{rgh} = P - \rho \mathbf{g}.\mathbf{x} \qquad \text{Eq. 3-13}$$

Where P_{rgh} is the modified pressure and $\mathbf{x}$ is the position vector. This modified pressure simplifies the boundary condition when a no-slip condition is used. Since the normal component of the pressure gradient for each phase is different because of the hydrostatic pressure, the modified pressure simplifies the boundary definition. By implementing the modified pressure definition in the momentum equation, a new equation can be defined as:

$$\frac{\partial(\rho\mathbf{U})}{\partial t} + \nabla.(\rho\mathbf{U}\mathbf{U}) - \nabla.(\mu\nabla\mathbf{U}) - (\nabla\mathbf{U}).\nabla\mu = -\nabla P_{rgh} - \mathbf{g}.\mathbf{x}\nabla\rho + \sigma k\,\nabla\alpha \qquad \text{Eq. 3-14}$$

3.1.2 Discretization of the Navier-Stoke equations

In this section, the Navier-Stokes equations are discretized and solved for the incompressible system. General forms of continuity and momentum equations of the Navier-stokes can be written as [117]:

$$\nabla.\mathbf{U} = 0 \qquad \text{Eq. 3-15}$$

$$\frac{\partial\mathbf{U}}{\partial t} + \nabla.(\mathbf{U}\mathbf{U}) - \nabla.(\nu\nabla\mathbf{U}) = -\nabla p \qquad \text{Eq. 3-16}$$

To discretize the Navier-Stokes equations, two issues must be addressed. These two issues are the pressure-velocity coupling and the non-linearity term ($\nabla.(\mathbf{U}\mathbf{U})$) of the momentum equation.

The non-linearity term can be solved by rewriting the term as follow:

$$\nabla.(\mathbf{U}\mathbf{U}) = \sum_f F(\mathbf{U})_f = a_P\mathbf{U}_P + \sum_N a_N\,\mathbf{U}_N \qquad \text{Eq. 3-17}$$

where, F is the mass flux through the face and should satisfy the Eq.3-15, a_P and a_N are function of $\mathbf{U}$ and are calculated from F. The pressure equation can be derived by the integral form of the momentum equation and therefore:

$$a_P\mathbf{U}_P = H(\mathbf{U}) - \nabla p \qquad \text{Eq. 3-18}$$

where, $H(\mathbf{U})$ has two terms including the transport part and the source part and hence can be written as:

$$H(\mathbf{U}) = -\sum_N a_N\mathbf{U}_N + \frac{\mathbf{U}^0}{\Delta t} \qquad \text{Eq. 3-19}$$

To express **U**, Eq. 3-18 is used:

$$\mathbf{U}_P = \frac{\boldsymbol{H}(\mathbf{U})}{a_P} - \frac{1}{a_P}\nabla p \qquad \text{Eq. 3-20}$$

where $\mathbf{U}_P$ is the velocity at the center of the cell. The velocity on the cell face is interpolated:

$$\mathbf{U}_f = \left(\frac{\boldsymbol{H}(\mathbf{U})}{a_P}\right)_f - \left(\frac{1}{a_P}\right)_f (\nabla p)_f \qquad \text{Eq. 3-21}$$

Eq. 3-21 is used to calculate the face fluxes. The discretization form of the continuity equation is:

$$\nabla.\mathbf{U} = \sum_f S.\mathbf{U}_f = 0 \qquad \text{Eq. 3-22}$$

where S is the outward-pointing face area vector of the control volume. By substituting Eq. 3-21 into the discretized form of the continuity equation, the new form of pressure equation can be expressed as:

$$\nabla.\left(\frac{1}{a_P}\nabla p\right) = \nabla.\left(\frac{\boldsymbol{H}(\mathbf{U})}{a_P}\right) = \sum_f s.\left(\frac{\boldsymbol{H}(\mathbf{U})}{a_P}\right)_f \qquad \text{Eq. 3-23}$$

Finally, the discretized form of the Navier-Stokes equations are:

$$a_P\mathbf{U}_P = H(\mathbf{U}) - \sum_f S(p)_f \qquad \text{Eq. 3-24}$$

$$\sum_f S.\left[\left(\frac{1}{a_P}\right)_f (\nabla p)_f\right] = \sum_f S.\left(\frac{\boldsymbol{H}(\mathbf{U})}{a_P}\right)_f \qquad \text{Eq. 3-25}$$

The flux at the face is then obtained as:

$$F = S.\mathbf{U}_f = S.\left[\left(\frac{\boldsymbol{H}(\mathbf{U})}{a_P}\right)_f - \left(\frac{1}{a_P}\right)_f (\nabla p)_f\right] \qquad \text{Eq. 3-26}$$

3.1.3 Pressure-velocity coupling

The PISO algorithm (Pressure-Implicit with Splitting of Operators) is a widely used method to handle the linear dependency of the pressure with the velocity in the Navier-stokes equations. The PISO algorithm can be summarized as follows [117]:

1) Once the momentum equation is solved, the pressure field from the previous time step is used to calculate the pressure gradient source term. This step is known as the “momentum predictor”. By solving Eq. 3-24, an approximation of the new field of velocity is obtained.

2) In this step, the predicted velocity is used to assemble the operator of $\mathbf{H(U)}$. Then the first new pressure field can be estimated by the pressure equation. This step is known as the pressure solution.
3) Using the new pressure field in the Eq. 3-26, a set of conservative fluxes can be obtained. The velocity field is then corrected using Eq.3-20.

The velocity correction can be calculated using an explicit scheme. The discretized form of velocity field (Eq. 3-20) shows that the velocity correction includes two terms. The first term is the $\frac{\boldsymbol{H}(\mathbf{U})}{a_P}$ term and the second term is related to the pressure gradient. The explicit scheme of the velocity correction implies that the first term is disregarded and only the pressure term is considered. Therefore, one can conclude that the PISO algorithm is comprised of an explicit velocity correction and an implicit momentum predicted. The PISO algorithm is repeated until a convergence criterion is satisfied.

3.2 OpenFOAM

OpenFOAM (Open Field Operation and Manipulation) [112] is an open source software package which is used widely for academic and industrial purposes [112]. OpenFOAM is written C++ and provides users with numerical solvers to model different complex physics. The most important advantage of open source codes is the extensibility which enables users to adapt the software and make it more efficient for their project. OpenFOAM, which is an object-oriented library, can simulate a wide range of engineering problems using the finite volume method (FVM) with massive parallel computing. Users have access to the OpenFOAM source codes, and they can add or modify the functions or equations if needed. Different solvers are implemented in OpenFOAM for specific CFD projects [118].

InterFoam is one of these solvers and is based on the VOF method to predict the interface between two incompressible, immiscible and non isothermal liquids. In this project, this solver is used for the free surface test case.

3.3 Validation the VOF solver

Before the CFD method can be coupled with the DEM method for modelling of multiphase granular flows, it must be validated. To validate the performance of the implemented CFD method (with VOF solver), a wieldy-used dam break problem is used. The open-source package OpenFOAM v.5 is used to set up the numerical model which runs on Ubuntu 16.04. The dam break experiment presented by Lobovský, Libor, et al (2014) is simulated with the InterFoam solver. Figure 3.3 shows the computational domain. As Figure 3-3 shows, the length of the box is 161 cm and a water column behind the gate has the height, length and width of 30 cm, 60 cm and 15 cm, respectively. The density, kinematic viscosity and surface tension in this case are considered 997 kg/m^3, $8.9\times10^{-7}\ m^2s^{-1}$ and 0.072 Nm^{-1} respectively.

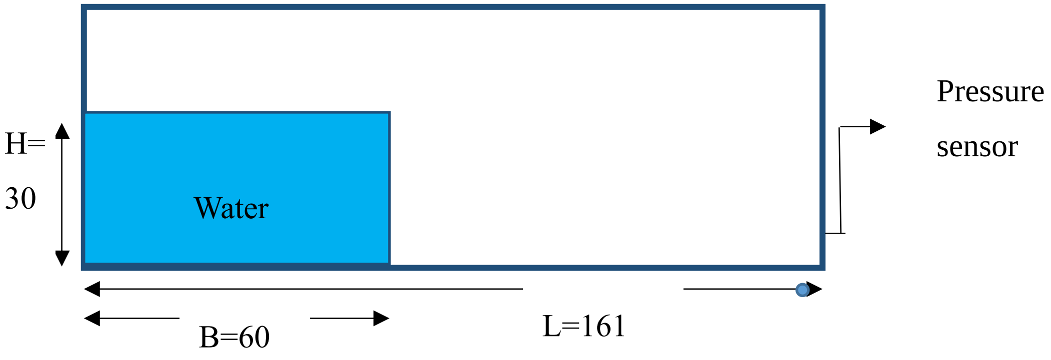

Figure 3-3 Initial configuration of dam Break test case

The simulation starts when the gate is removed, and the water is released. To validate the solver, the wave propagation, the snapshot of water profiles at different time steps, and the pressure at a specific point calculated by OpenFOAM are compared with the experimental results. To simulate the dam break test case, meshes of 5 mm were used. The initial velocity and pressure are set to zero because there is no motion initially. The initial volume fraction for the water of column is $\alpha = 1$ and $\alpha = 0$ for the rest of the geometry because the cells are filled with the air. A no-slip boundary condition is assigned at the solid walls of the computational region which implies that the velocity vector is equal to zero. Neuman conditions are considered for the pressure and the volume fraction: $\partial p / \partial n = 0$ and $\partial \alpha / \partial n = 0$. The pressure, velocity and volume fraction at the interface region are set to zero.

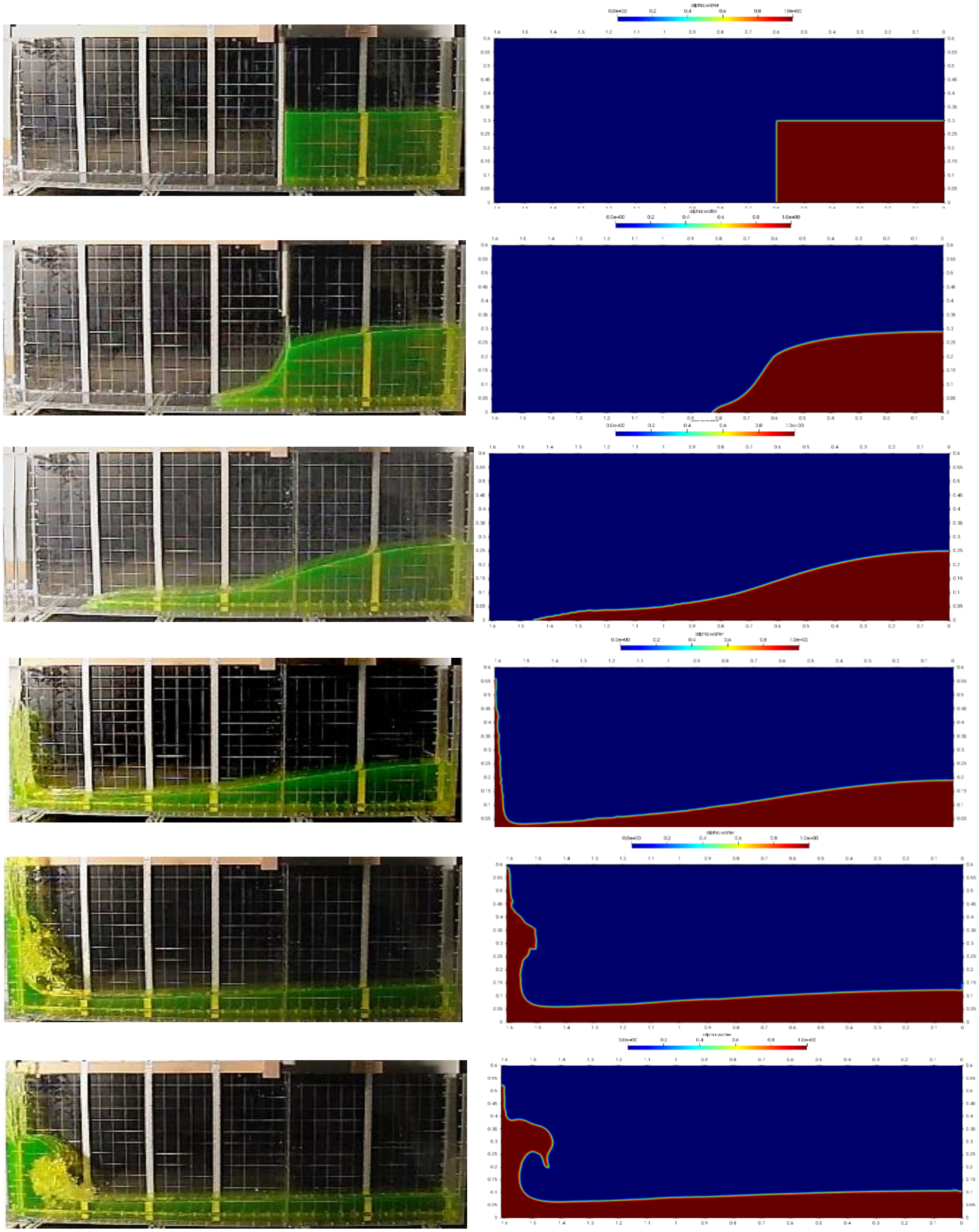

Figure 3-4 Simulation and experiment results for the evolution of free surface profile at [T]=0, 0.91, 2.13, 3.27, 4.93, 5.85

Figure 3-4 shows a comparison between the free surface profile evolution in dimensionless time steps ($T = t\sqrt{g/H}$) predicted by OpenFOAM and the one obtained from experimental results.

Upon gate removal, a gravity-driven downstream wave moves along the dry bed. Once the wave reaches the downstream wall, it runs up vertically as a jet and then rolls and falls into the fluid underneath. The simulation predicts well the free surface profile evolution in comparison to the experiment.

Another way to validate the simulation was performed by comparing the wave front propagation along the dry bed with the experiment. Figure 3-5 shows a good agreement between the wave front evolution predicted by the simulation and the one obtained through experiment. It should be noted that in the experiment, the high speed at which the gate is removed produces a strong shear stress affecting the profile of the free surface near the gate. In the simulation, however, the physical gate is not defined and thus, no shear stress is present between the gate and the water column. Consequently, the discrepancy of the free surface profiles between the simulation and the experiment can be caused by this issue.

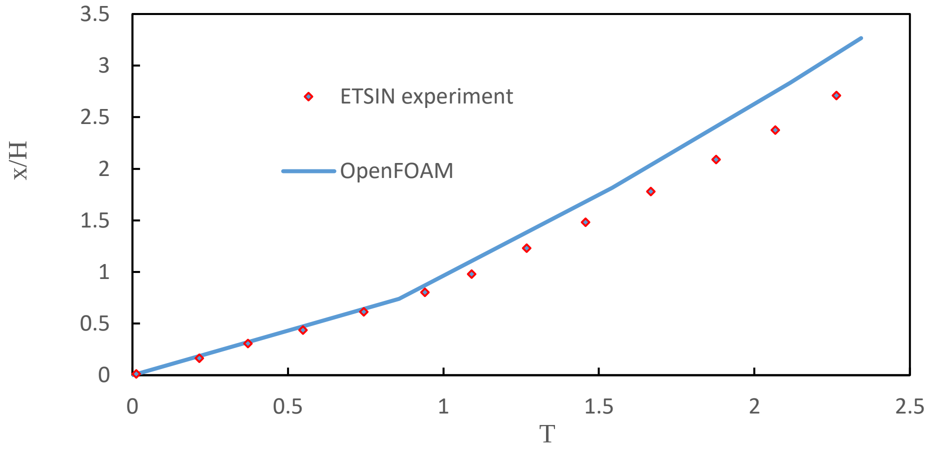

Figure 3-5 The surge front propagation compared to the experiment

The pressure estimated by the simulation is also validated with the measured pressure of a sensor located on the vertical wall at a height of 3 mm. Figure 3-6 shows a comparison between the measured pressures by the sensor and the pressure obtained from the simulation. Since the experiment has been repeated several times, results for different trails are plotted as the thick gray line. The pressure also is non-dementalized with the hydrostatic pressure at the bottom of the tank (i.e. $\rho g H$).

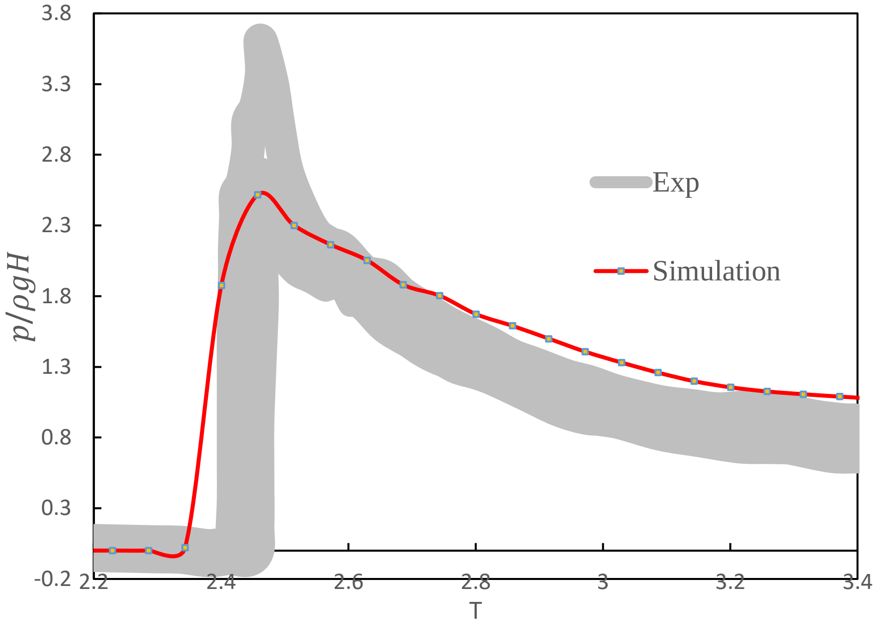

Figure 3-6 Comparison of the measured pressure in experiment and Simulation for a specific point on the vertical wall

It can be seen from Figure 3-6 that the highest peak of pressure occurs at almost the same time for the simulation and the experiment. However, the rising pressure generated by the water wave hitting the vertical wall happens earlier in the simulation due to the wave propagation being slightly underestimated in the simulation by 30%.

3.3.1 Mesh convergence analysis

The accuracy of the CFD results is inversely proportional to the mesh size. As the mesh size decrease, the results are more reliable and accurate. On the other hand, decreasing the mesh size implies increasing the number of meshes. The CFD simulation time is directly proportional to the number of meshes in the computational domain. If the number of meshes increases, the simulation time increases as well. In order to minimize the computational expense while keeping a high level of resolution of the computational domain, a mesh size optimization must be performed [119, 120].

For the dam break test, a mesh convergence study was conducted by three simulations with uniform mesh sizes of 5 mm, 10 mm and 15 mm to predict the pressure at a specific point on the wall. Figure 3-7 shows the pressure predicted by the simulations for different mesh sizes. The pressure predicted by the simulation using a coarse mesh (15 mm) was not in good agreement with the experiment while the simulation with the finer mesh (10 mm) yielded better results. The result obtained from the simulation using a 5 mm mesh size shows better agreement (RMSE = 0.37) with the experiment compared to the simulation with the larger sizes of 10 mm (RMSE=0.52). Simulation with a finer mesh (2.5 mm) was found expensive computationally. Thus, using a 2.5 mm mesh size will not be necessary since computational time will significantly increase.

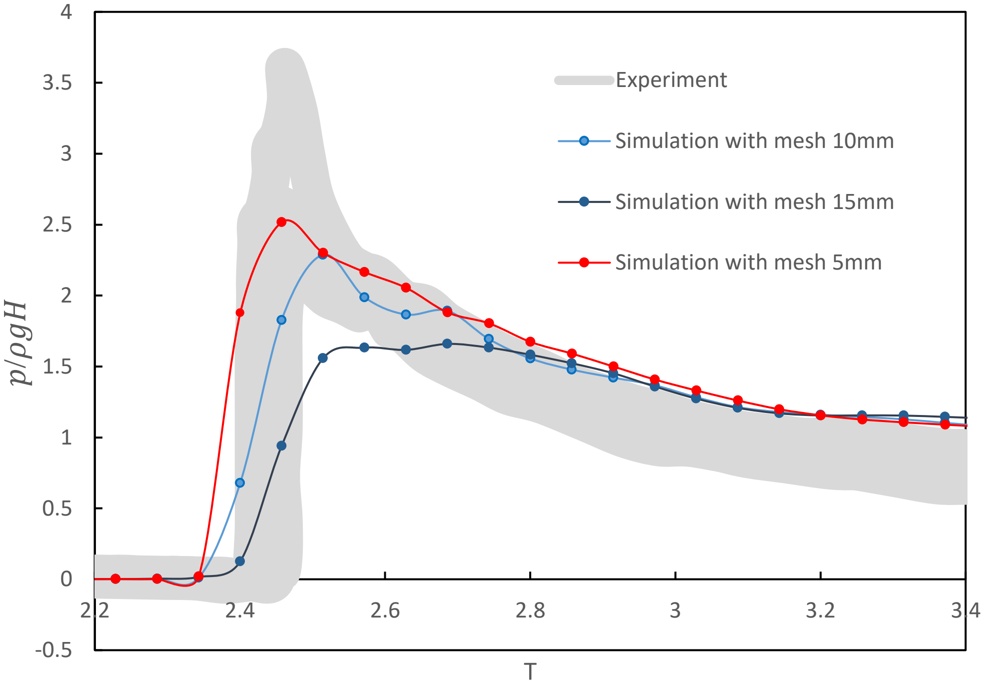

Figure 3-7 Comparison of the measured pressure in experiment and Simulations with different mesh sizes for a specific point on the vertical wall for

3.4 Conclusion

In this chapter, a hydrodynamic model was implemented to simulate a multiphase flow system using VOF method. Opensource code OpenFOAM has been used to simulate a dam break test case. The validation shows the capacities of the VOF solver to model the dam break. However, the water column releasing mechanism in the simulation is different from the experiment and this discrepancy affects the wave propagation and, consequently, influences the time at which the peak pressure occurs. The accuracy of results extremely is depended on mesh sizes in CFD approaches. However, to prevent the computational cost, a mesh size optimization must be performed.

CHAPTER 4 SIMULATION OF MULTIPHASE GRANULAR FLOWS USING CFDEM COUPLING

In this chapter, a coupled CFD-DEM model is developed with the volume of fluid (VOF) method for free surface granular flows. First, we briefly introduce CFD-DEM coupling method and the open source software package implemented in this work. Then the governing equations of incorporating VOF into the unresolved CFD-DEM is presented to capture the free surface and to model the interaction between fluid and particles. At the end, the developed solver is validated in different test cases.

4.1 CFD-DEM coupling

Multiphase flows are widely found in various industry areas and nature. The study of such a complicated phenomenon of gas-liquid-solid flows is difficult issue due to the interactions of different phases. To overcome these difficulties, a number of collective attempts have been made on modeling the solid particles and fluid phases. Among the models proposed, CFD-DEM proved to be more computational efficiency and convenience [36]. Hence, the combination of CFD with DEM is generally accepted in engineering application to describe fluid- particle flow in which the motion of solid particles is modeled individually based on Newton's law and the fluid phase as a continuum is described by the CFD based on the Navier-Stokes equations.

The coupling of the mesh-based Eulerian CFD model with the particle based DEM method can be based on two different approaches, namely, resolved and unresolved CFD-DEM (see Figure 4-1). In the resolved CFD-DEM coupling, the DEM particles are significantly larger than the CFD grid. In this approach each particle must cove at least 8 computational grids [121]. Considering the typical size of granular particles, the grid cells can have a length-scale as small as that of Direct Numerical Simulations (DNS). This method provides the in-depth physics of particle -fluid interaction, however, it is computationally very expensive. Therefore, it is only suitable for cases where we have a low number of particles and want to resolve the behavior of flow between the particles.

On the other hand, the unresolved CFD-DEM coupling the size of grid cells is much larger than that of the particles, therefore, it is computationally affordable for cases with a large number of particles. In this method flow behavior between the particles is not resolved, and the average impact of the particles in the cell is considered [121]. Figure 4-1 shows a comparison of resolved and unresolved CFD-DEM. Considering the nature of the problem and the number of particles, in this work, we use the unresolved CFD-DEM to develop a hybrid hydrodynamics multi-granular flow. In most of the interaction between solid particle and fluid, an unresolved CFD-DEM is adopted for those cases where a large number of particles is used, while resolved coupled CFD-DEM method is designed for cases where the number of particles are small.

(a) Unresolved CFD-DEM (b) Resolved CFD-DEM

Figure 4-1 Schematic of the CFD grid size and particle size in two CFD-DEM approaches

The coupling procedure can be classified into three different cases depending on the interactions between fluid and solid phases: One-way coupling, where only the fluid influence on the particle motion is considered and the particle influence on the fluid is neglected. Two-way coupling, where both influence of particles on fluid and fluid on particles are considered. Four-way coupling, where particle-particle interactions are taken into account as well as the influence of particles to the fluid phases and vice versa [122].

In this study, all multi-phase granular flows are simulated by CFDEM opensource software. CFDEM is an Open Source CFD-DEM engine developed by Goniva et al. [80] .The opensource code CFDEM, combines DEM engine of LIGGGHTS as a C++ library to a CFD framework the OpenFOAM solvers. Both open sources LIGGGHTS and OpenFoam have the capability to run the cases in parallel computation via the Massage Passing Interface (MPI). Running in parallel significantly reduces the computational cost particularly when the number of particles is high. CFDEM also supports full 4-way coupling where all interactions between solid phase and fluid phases are considered [121].

One of the challenges of modeling the multiphase granular flow in presence of free surface (i.e. when three phases of air, liquid and solid is involved) is capturing the free surface. In this study, in order to take into account, the free surface fluid, the volume of fluid (VOF) is incorporated to the CFDEM coupling. The integration of the VOF method into the CFDEM coupling is carried out via the development and combination of the VOF solver, which is called interFoam in the OpenFoam with the CFDEM package. InterFoam is one of OpenFoam's solver used to model multiphase flows for two incompressible, isothermal immiscible fluids using VOF method.

4.2 Governing equations

The model presented in this study is developed for a three-phase system in which water is the primary fluid, air is the secondary fluid and the two fluids are assumed immiscible. Particles interact with other particles and the fluid. The governing equations employed are: the DEM equations used to describe the motion of particles, the Navier-Stokes equations and the modified equation of volume of fluid.

4.2.1 Governing equations of the motion of the particles

As described in chapter 2, the governing equation of translational and rotational motion of each particle can be expressed by:

$$m_i \frac{d\mathbf{U}_i}{dt} = \sum_{j=1}^{n_i^c} \mathbf{F}_{ij}^c + \mathbf{F}_i^f + m_i \mathbf{g} \qquad \text{Eq. 4-1}$$

$$I_i \frac{d\boldsymbol{\omega}_i}{dt} = \sum_{j=1}^{n_i^c} \mathbf{M}_{ij}^c \qquad \text{Eq. 4-2}$$

where, $m_i \; and \; \mathbf{U}_i$ are the mass and translational velocity of particle *i* respectively, $\mathbf{F}_{ij}^c$ is the contact force between particles *i* and *j*, $\mathbf{F}_i^f$ is the fluid force on the particle *i* , I_i is the inertia moment of particle *i*, $\boldsymbol{\omega}_i$ is the angular velocity of particle *i* and $\mathbf{M}_{ij}$ is the moment between particles *i* and *j*. A local-average assumption is used, and this implies that the variables of fluid in the computational cell are averaged over the whole particles. This entails that the torque acting on the surface of particles are not considered since the particle-fluid interaction force is acting on the centroid of the particles and a null torque is obtained and used throughout the particle. Therefore, Eq. 4-2 is considered only for particle-particle interaction not particle-fluid interaction [100].

4.2.2 Navier-stock equations

In the CFD side, the free surface and particles in a multiphase flow are modeled using the Navier-Stocks equations expressed as follows:

$$\frac{\partial(\alpha_f \rho_f \mathbf{u}_f)}{\partial t} + \nabla.\left(\alpha_f \rho_f \mathbf{u}_f \mathbf{u}_f\right) = -\alpha_f\left(\nabla P_m + (\mathbf{g}.\mathbf{X})\nabla \rho_f\right) + \nabla.\left(\alpha_f \boldsymbol{\tau}\right) + \mathbf{f}_s - \mathbf{R}_{pf} \qquad \text{Eq. 4-3}$$

$$\frac{\partial \alpha_f}{\partial t} + \nabla.\left(\alpha_f \mathbf{u}_f\right) = 0 \qquad \text{Eq. 4-4}$$

Where ρ_f is the density of fluid, u_f and α_f are the velocity and the volume fraction of fluid respectively. The modified pressure of the fluid is $P_m = P - \rho_f \mathbf{g}.\mathbf{X}$ as discussed in chapter 3, in which $\mathbf{X}$ is the coordinate vector. $\boldsymbol{\tau}$ is the stress tensor and can be obtained as $\boldsymbol{\tau} = \mu_f(\nabla \mathbf{u}_f + \left(\nabla \mathbf{u}_f\right)^T)$, where μ_f is the dynamic viscosity of fluid. $\mathbf{f}_s = \boldsymbol{\sigma}.k.\nabla\alpha_1$ is the volumetric surface force due to the pressure gradient in the free surface flows. Where k is the mean curvature of the free surface and $\boldsymbol{\sigma}$ is the surface tension. As we discussed in chapter 3, in VOF method, the viscosity and the density of the fluid are the weighted average of two phases. Therefore, the viscosity and density can be expressed as :$\mu_f = \alpha_1\mu_1 + \alpha_2\mu_2$ and $\rho_f = \alpha_1\rho_1 + \alpha_2\rho_2$, where α_1 and α_2 are the volume fraction due to the liquid phase and gas phase respectively. $\mathbf{R}_{pf}$ is the momentum exchange with the particles due to the fluid-particles interactions [100].

4.2.3 Fluid-particles interactions

In multiphase granular systems(solid-gas-Fluid), the surrounding fluid will influence the particle motions through various particle-fluid interactions forces. The typical particle-fluid interaction forces are the drag force, buoyancy force, pressure gradient force, the viscous force, the virtual mass force and the Basset force [36, 121]. However, in many multiphase systems, the main and dominant forces are the drag force, the pressure gradient force and the viscous force and the rest of forces are usually disregarded [121]. In order to take into account theses interactions forces, two kinds of formulations called model A and model B have been proposed to take into account [30, 121] .Depending on the treatment of the pressure term, explicitly or implicitly, model A and model B are different. In model A the fluid equation (Eq. 4-3) consists of both the solid and the fluid pressure. while in model B, the pressure term is attributed to the fluid phase only [30, 121].

In this study, the drag force and the buoyancy force are considered as the main interaction forces. The buoyancy force is applied on particles by the following equation [93]:

$$\mathbf{F}^{b} = \frac{1}{6}\pi\rho d_{p}^{3}\mathbf{g} \qquad \text{Eq. 4-5}$$

The drag model used in this work is proposed by Di Felice and the momentum exchange $\mathbf{R}_{Pf}$ can be calculated based on this model by K_{Pf} and the relative velocity of the fluid and particle:

$$\mathbf{R}_{Pf} = \mathbf{K}_{Pf}(\mathbf{U}_{f} - \mathbf{U}_{P}) \qquad \text{Eq. 4-6}$$

Where $\mathbf{U}^{f}$ and $\mathbf{U}^{P}$ are the velocity of fluid and particle respectively and $\mathbf{K}_{Pf}$ is determined by:

$$\mathbf{K}_{Pf} = \frac{1}{8}C_{d}\rho_{f}\pi\bar{d}_{P}^{2}(\mathbf{U}_{f} - \mathbf{U}_{P}){\alpha_{f}}^{1-x} \qquad \text{Eq. 4-7}$$

where α_{f} is the porosity in the particle Reynolds number, $\bar{d}_{P}$ is the average diameter of particle and C_{d} is the drag coefficient depending on the Reynolds number of the particle and can be obtained from:

$$C_{d} = \left(0.63 + 4.8/\sqrt{Re_{P}}\right)^{2} \qquad \text{Eq. 4-8}$$

where Re_{P} can be calculated by:

$$Re_{P} = \frac{\alpha_{f}\rho_{f}d_{P}|U^{f} - U^{P}|}{\mu_{f}} \qquad \text{Eq. 4-9}$$

x is a corrective function and can expressed as:

$$x = 3.7 - 0.65\exp\left(-\frac{(1.5 - \log_{10}Re_{P})^{2}}{2}\right) \qquad \text{Eq. 4-10}$$

It is worth mentioning that due to the assumption of local average approach, the fluid-particle interaction on a single particle is replaced by applying on its centroid. Therefore, the fluid torques is negligible and are not combined in this study [93, 100].

4.2.4 PISO algorithm for free surface CFD-DEM:

As we discussed in chapter 3, PISO algorithm is adopted to deal with pressure-velocity coupled to solve Navier-Stock equations. Generally, PISO loop contains three steps. First, the velocity and pressure fields from the previous time step are used to solve momentum equation and the velocity is predicted in this step. The discretized form of predicted velocity can be written as:

$$a_p^{\mathbf{u}}\,\mathbf{u}_p = H(\mathbf{u}) - \alpha_f \nabla p_m - \alpha_f(\mathbf{g}.\mathbf{x})\nabla\rho_f + \mathbf{f}_s - \mathbf{R}_{pf} \qquad \text{Eq. 4-11}$$

Where $a_p^{\mathbf{u}}$ is a function of $\mathbf{u}$ and is the matrix coefficient for solving the pressure field. $\mathbf{H}(\mathbf{u})$ consist of the source term and the transport term which can be written as:

$$\mathbf{H}(\mathbf{u}) = \nabla.\left(\alpha_f \boldsymbol{\tau}\right) - \textstyle\sum_N a_N^{\mathbf{u}}\,\mathbf{u}_N \qquad \text{Eq. 4-12}$$

Where the $a_N^{\mathbf{u}}$ is the coefficient matrix related to the velocity field. The velocity can be predicted by:

$$\mathbf{u}_p = \left[a_p^{\mathbf{u}}\right]^{-1}\left[\mathbf{H}(\mathbf{u}) - a_f \nabla p_m - a_f(\mathbf{g}.\mathbf{x})\nabla\rho_f + \mathbf{f}_s - \mathbf{R}_{pf}\right] \qquad \text{Eq. 4-13}$$

In the next step, by substituting the predicted velocity into the transport equation (Eq. 4-4), the pressure field is corrected as:

$$\nabla.\left\{\alpha_f^2[\alpha_P^{\mathbf{u}}]^{-1}\nabla P_m\right\} = \nabla.\left\{[\alpha_P^{\mathbf{u}}]^{-1}\left[\alpha_f \mathbf{H}(\mathbf{u}) - \alpha_f^2(\mathbf{g}.\mathbf{X})\nabla\rho_f + \alpha_f \mathbf{f}_s - \alpha_f \mathbf{R}_{Pf}\right]\right\} + \frac{\partial\alpha_f}{\partial t} \qquad \text{Eq. 4-14}$$

The additional term $\frac{\partial\alpha_f}{\partial t}$ in the right-hand side appears due to the presence of the solid phase in granular flows. In the last step, the velocity is updated with the pressure field obtained from Eq. 4-14 [100].

4.2.5 Modification of the VOF method for a three-phase flow(solid-liquid-gas)

Applying the VOF method for flow including granules needs a modification of the VOF equations. One of the important equations of the VOF method is the transport equation. The transport equation for the three-phase system can be expressed as:

$$\frac{\partial(\alpha_f\alpha_1)}{\partial t} + \nabla.\left(\alpha_f\alpha_1\mathbf{u}_f\right) + \nabla.\left(\alpha_f\alpha_1(1-\alpha_1)\mathbf{u}_r\right) = 0 \qquad \text{Eq. 4-15}$$

Where u_r is the compression velocity as discussed in chapter 3 to yield a sharper interface. α_f represents the local average and α_1 is an indicator of the ratio of wet volume to the dry volume. In other words, $\alpha_1 = 1$ represents a computational cell which is totally occupied with water and $\alpha_1 = 0$ a computational cell which is dry. α_1 between 0 and 1 indicates that the cell is partially filled with liquid and therefore represents the free surface region. Hence, α_1 is the α volume of fraction discussed in the VOF method. In the three-phase flows, each computational cell can be occupied with the particles as well as liquid and air. α_f indicates the void fraction or porosity and can be written as:

$$\alpha_f = 1 - \sum \frac{V_{pi}}{V_c} = (V_1 + V_2)/V_c \qquad \text{Eq. 4-16}$$

Where V_{pi} is the volume of particles in each cell, V_c is the total volume of the computational cell and V_1 and V_2 are the volume of two fluids (air and water). We can define $V_v = V_1 + V_2$ as the volume of void fraction. In a three-phase system, $\alpha_1 = V_1/(V_1 + V_2)$ is the volume fraction of the water over the volume of void. Therefore, $\alpha_f \alpha_1 = V_1/V_c$ indicates the local average phase fraction using the transport equation in VOF method. Figure 4.2 shows a typical three-phase system and how volume fraction and void fraction are considered. It is worth noting that in this VOF method, the position of particles in each computational cell are not considered in the calculation of the volume fraction of fluid and solid as shown in Figure 4-2 .

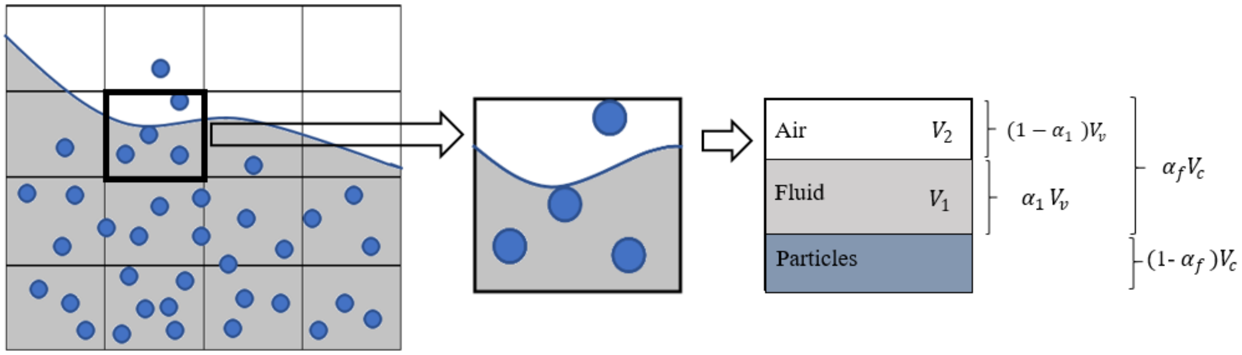

Figure 4-2 Three phase volume fraction in free surface grnaular flow

The transport equation (Eq. 4-8) for three phases systems, comparing to the VOF method has an additional temporal term due to the presence of α_f [100].

4.2.6 Calculation of the local void fraction:

The local void fraction significantly affects the particle’s contribution to particle-fluid forces. The void fraction can be calculated by different approaches. One simple method is based on summing up the volume of those particles whose centre is inside the computational cell. For example, as

Figure 4-3 shows, in addition to the particles B and C, particles A, D and E are counted to calculate the void fraction of the void fraction of cell 1. This method is known as the centre void fraction and, as the name implies, it estimates the value of void fraction for the cells with the particle' centroids and underestimates the void fraction of the neighbouring cells. To improve the calculation the void fraction, the divided method was proposed to calculate the exact void fraction in each cell. The void fraction of cell i can be calculated based on $\omega_{ij} = V_{ij}^{p}/V_{i}^{p}$, where ω_{ij} varies between 0 and 1, V_{ij}^{p} is the volume of the particle i located in cell j, and V_{i}^{p} is the entire volume of particle i. ω_{ij} will become 0 when the particle is completely out of the cell j and 1 when the total volume of the particle is inside the cell j. Hence, the exact void fraction for each cell can be calculated using this method [93, 100].

The two previously mentioned methods are not precise when the particle sizes approach the cell size. Link et al.[123] proposed another method to overcome this limitation where a porous particle's volume is assumed greater than the actual volume of the particle. The void fraction is then obtained by summing up the portions of the porous particle in the cell. A similar model, the bigParticle model, is available in the CFDEMcoupling package and is used to calculate porosity.

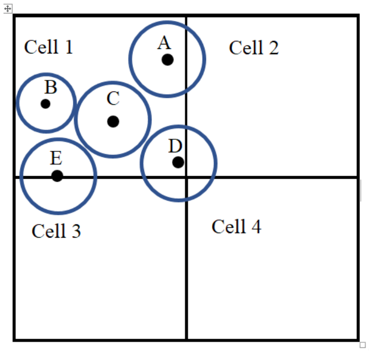

Figure 4-3 Calculation of void fraction in computational cells

After evaluating the particle volume fraction, the fluid-particle interaction momentum exchange can be calculated [100].

4.2.7 Time step in CFD-DEM:

In the coupling of CFD-DEM method, selecting the suitable time step is an important issue. Generally, DEM method requires smaller time step than CFD calculation because it is very important in DEM method to keep the time step sufficiently low to detect the collision events and satisfy the maximum overlap. To choose the time step in CFD-DEM, three critical time steps have to be considered: the Rayleigh time step, the relaxation time step and the time step required to satisfy stability. These are explained more in depth below.

- Time step in DEM:

  In DEM, numerical stability depends on Rayleigh waves. It means that the motion of particles is affected by disturbances propagation from particles located at a distance as well as neighbouring particles. Therefore, the time step for collision detection should be less than the Rayleigh time step which is defined as [121]:

$$T_R = \pi r \frac{\sqrt{\rho/G}}{0.1631\nu+0.8766} \qquad \text{Eq. 4-17}$$

Where ρ and r are the density and the radius of the particles, ν is Poisson's ratio and G is the shear modulus of the particles.

In coupled CFD-DEM model, as the fluid influence the motion of particles, an additional critical time step in DEM is required. Particle relaxation time τ is a measure of the resistance of particle to follow the fluid. Thus, larger relaxation time step indicates more resistance of particles against the fluid flow. Relaxation time step can be defined as [121] :

$$\tau_p = \frac{\rho_p d_p^2}{18\mu}(1 + 0.15Re_p^{0.687})^{-1} \qquad \text{Eq. 4-18}$$

where Re_p is the Reynolds number of particles given by:

$$Re_p = \frac{\rho_{f(u-u_p)d_p}}{\mu} \qquad \text{Eq. 4-19}$$

To prevent numerical instability, DEM time step should not be larger than the relaxation time step and the Rayleigh time step. Hence, in the DEM side, there are two critical time steps the DEM time step should not exceed.

- Time step in CFD:

In CFD side, where only the fluid phase is considered, the CFL number or Courant number is a necessary condition for numerical stability and is defined as [121]:

$$CFL = \frac{u.\Delta t_f}{\Delta x} \qquad \text{Eq. 4-20}$$

Where u is the fluid velocity, Δx is the size of computational cell and Δt_f is the time step in CFD. The stable simulation requires a CFL number equal or smaller than 1.

As mentioned earlier, the time step in DEM is smaller than the time step in CFD. In order to speed up the simulation and prevent a high computational cost, DEM time step and CFD time step can be set independently and the information is transferred between CFD and DEM at specific coupling time step. Typically, a coupling interval is set in CFD-DEM coupling which indicates how many DEM time steps are run before exchanging the data to the CFD side. which indicates how many DEM time steps are run before exchanging the data to the CFD side [121, 124].

4.3 Coupling algorithm

The CFD-DEM scheme for free surface granular flows is shown in Figure 4-4. As we mentioned before, in order to reduce computational expense and speed up the simulation, the DEM time step is chosen smaller than the CFD time step. Typically, an interval coupling ($\Delta t_{CFD}/\Delta t_{DEM}$) is defined which determines how many DEM time steps run before sending information to the CFD side. Therefore, the computation starts with the DEM side by detecting the position of each particle and their contacts. The DEM solves the equation of motion and as a result the position and velocity of particles are calculated based on the contact force and fluid force. The DEM solver computes and updates the velocity and position of particles until the coupling interval is completed Then the local volume fraction (or porosity) is evaluated and through the coupling process, the momentum exchange information is passed to the CFD side. Once the momentum equation is assembled, the VOF method is used to capture free surface and update the void fraction. Then the pressure and velocity fields are calculated by PISO iteration and the fluid forces acting on particles can be obtained. The fluid-particle forces are then sent to the DEM side to solve motion equations in a new computing cycle.

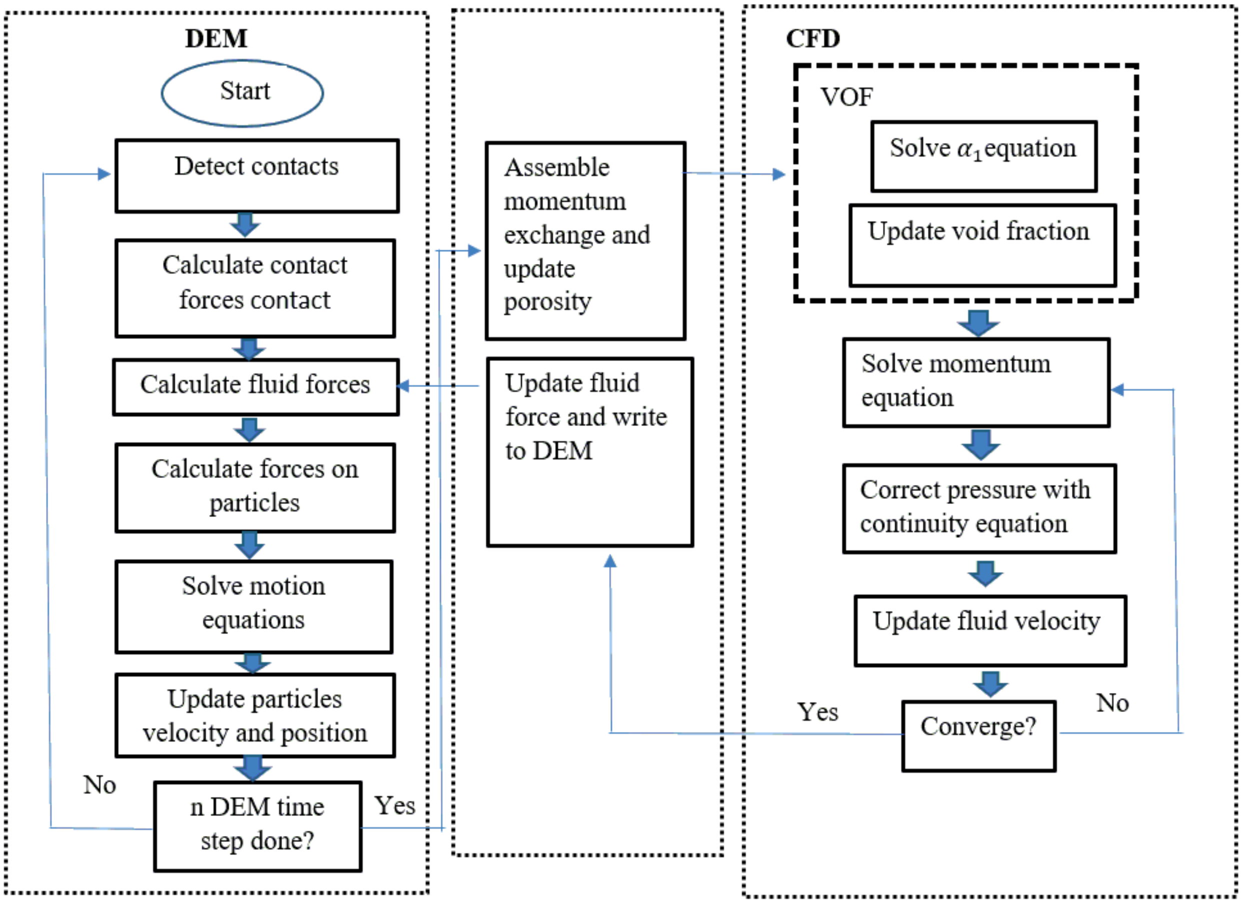

Figure 4-4 CFD-DEM scheme for free surface granular flows

4.4 Implementation and validation of the CFDM solver for free surface flows

In order to evaluate the capabilities of the developed CFDEM coupling solver, the solver is implemented for three test cases including the (1) pouring of a single particle into water, (2) granular collapse, and (3) submersed landslide. The first case is to evaluate the capability of method in dealing with the three-phase (gas, liquid, solid) systems. The second and third cases are to evaluate the model for studying the gravity driven multiphase granular flows. The granular materials in all test cases are glass beads and the fluid phase are water. The simulation results are compared with the experimental data to validate the solver.

4.4.1 One particle pouring from air into water

One particle sedimentation test is a simple case which we firstly used for validation of the solver. In this test case, one solid particle falls through an air-water interface. Figure 4-5 shows the computational setup. The computational domain has a length of 4 mm, a width of 4 mm and a height of 8 mm. One particle with the radiance of 0.1 mm and the initial velocity of zero from the height of 0.001 m above the free surface falls and settles inside the fluid. The particle density and air density are 2500 kg/m^3 and 1kg/m^3 respectively. The box has partially filled the water with a height of 0.004 m and a density of 1000 kg/m^3. The dynamic viscosity of air and water is considered 10 $^{-5}$ Pa.s and 10 $^{-3}$ Pa.s, respectively.

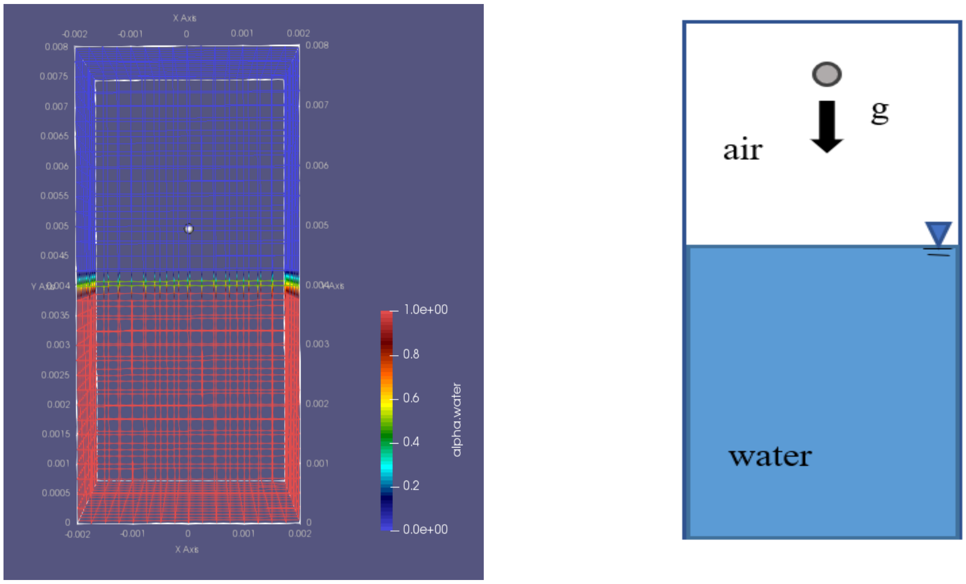

Figure 4-5 Initial set up of particle sedimentation

The velocity and the vertical position of the particle is estimated using the developed CFDEM coupling solver. The CFD mesh size is 0.25 mm which is enough large considering the particle's size. The simulation results are compared with the analytical solution presented in[101] which the Stokes's law is adopted when the particle settles in the water. Figure 4-6 shows a comparison of the particle velocity and the vertical position predicted by the developed CFDEMcoupling solver against the analytical solution. As Figure 4-6 shows, the velocity of the particle dramatically slows down when the particle enters the water phase. The vertical position prediction by the solver has a good agreement with the analytical solution as well. Although the particle motion in the simulation is slightly retarded comparing to the analytical solution, in general, the simulation results has a reasonable agreement with the analytical solution.

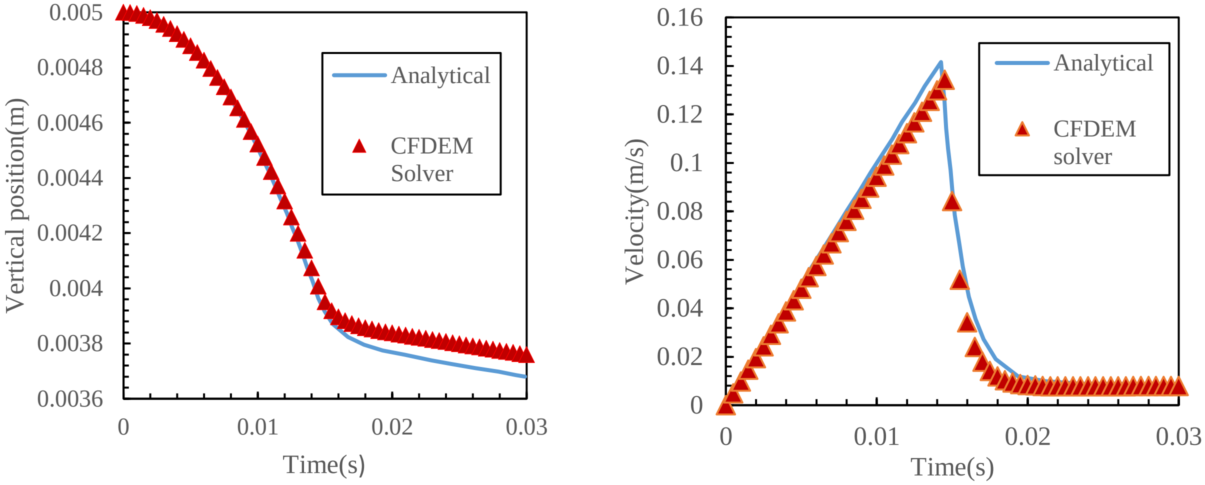

Figure 4-6 Comparison of the analytical solution with the CFDEM solver for one single particle sediment

4.4.2 Submerged granular collapse:

This test case is carried out at the Hydraulics Laboratory of Polytechnique Montreal by Prof. Ahmad Shakibaeinia. In this test case a column of particles is submerged with water in a tank. The length, height and width of the granular column are 0.0975 m, 0.048 m and 0.1 m respectively. The tank is filled with a water height (h_w) of 0.07m to completely submerge the granular column. The initial configuration is shown in Figure 4.7. The granular column is set behind a gate and with moving up the gate, the simulation starts. The granular material is glass beads and the material properties are illustrated in Table 4-1.

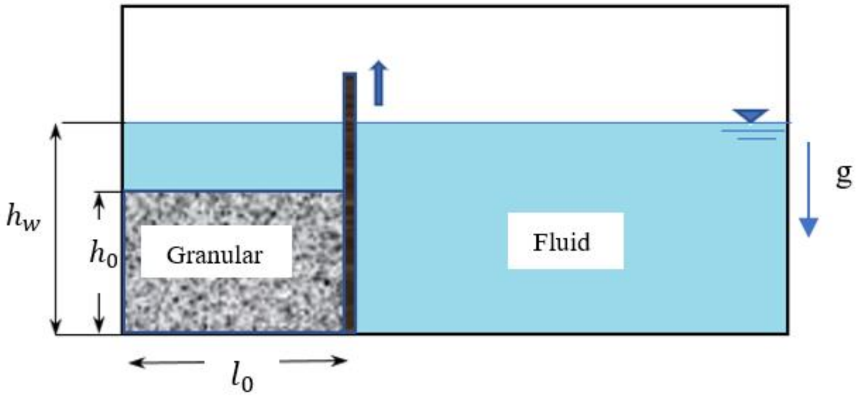

Figure 4-7 Initial configuration of the submerges granular flow test case

Table 4-1 Physical properties of the particles

Young's modulus (GPa)	Friction coefficient	Poisson ratio	Restitution coefficient	Density (kg/m^3)	Bulk density (kg/m^3)	Diameter (m)
60	0.4	0.45	0.9	2500	1535.993	0.0008

To simulate this case, a 3D developed unresolved CFD-DEM coupling is used. To create the initial configuration of the test case, first we run the pure DEM solver to set the particles behind the gate. The gate in this simulation is a STL file which can be imported by LIGGGHTS. When the particles settle in the specific space, the fluid phase can be added to the system in CFD side by running the SetFields utility. SetFields is one of the dictionaries of OpenFoam located in the system in VOF solver. To start the simulation the gate moves up with a velocity of 1m/s in the DEM side and the granular column collapse. To validate the solver, the surface profile and the runout distance in different dimensionless times were compared with the experimental results. The dimensionless time scale is defined $T = t/\sqrt{(\frac{h_0}{g})}$. The CFD grid size in this simulation is 0.0025 m and considering the particles size with the diameter of 0.0008m, the ratio of the CFD mesh over the particles size is 3.125. The simulation is done in parallel with 4 decomposition.

Figure 4.8 shows the snapshots of the simulation results against the experimental results in different dimensionless times([T]). The overall time evolution of the deposit configurations is in agreement with the experimental results. As Figure 4-8 shows by removal the gate in the experiment, some suspension of the particles at the front the granular mass is observed due to the gate removal mechanism. In the simulation, however, the gate is defined in the DEM side only. Therefore, this suspension of particles cannot be observed in the simulation.

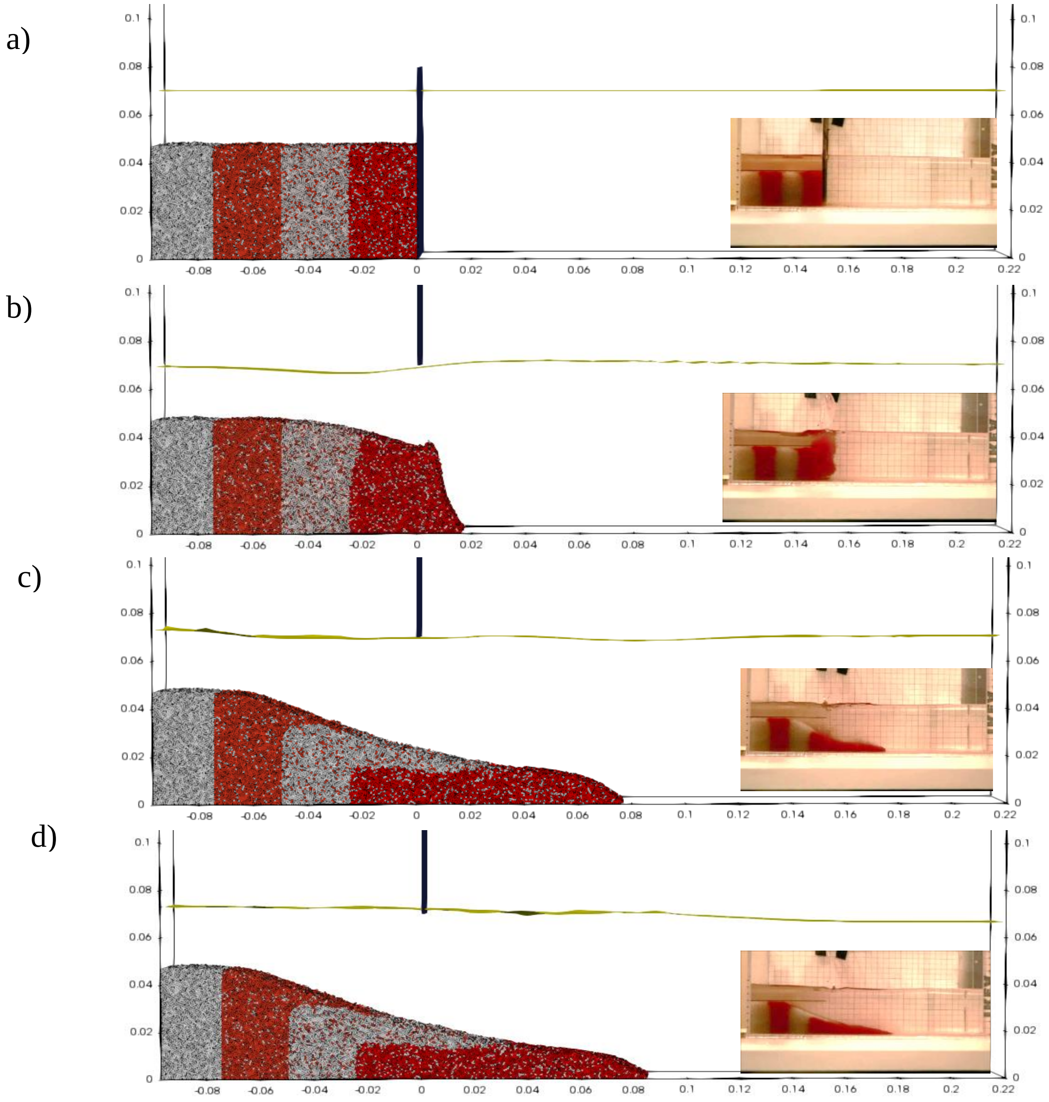

Figure 4-8 Deposit configuration of the submerged granular collapse (a) [T]=0, b) [T]=2, c) [T]=8 , d) final)

It should be noted that, this result was obtained with considering different coefficient friction 0f particle-particle and particle-walls. The coefficient friction for particle-particle was considered 0.4 and for particle-walls 0.1. one can concluded that for the submerged cases the friction between particle and walls is reduced due to the presence of fluid phase.

To validate the solver quantitatively, the digitized surface profiles of the granular collapse are comparing with the experimental surface profiles in Figure 4-9. The surface profiles predicted by the simulation relatively shows a good agreement with experimental results. As time goes on, the flat top of the deposit in the simulation is narrower than that of the experimental results([T]=5), but at the final time, the flat top of the deposit in the simulation becomes similar to the experiment.

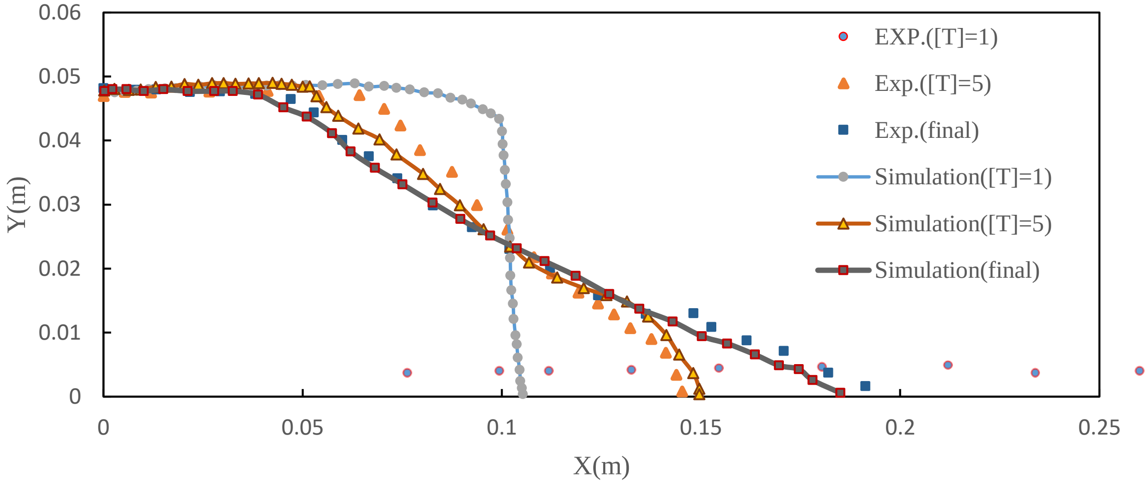

Figure 4-9 Simulation and experimental surface profile for the submerged granular collapse

The simulation results also are validated by plotting for different dimensionless time steps. Figure 4-10 illustrates a comparison of the runout distance of the submerged granular collapse with the experiment. The runout distance is defined based on the last particle of the flow front which is still connected to the mass granular. As Figure 4-10 shows although the CFDEM solver underestimated the runout distance for [T]$> \sim 8$, the overall runout distance is predicted very well corresponding to the experimental results. The error (RMSE) calculated for this test case is 0.004 m. Three flow regimes is observed in submerged granular collapse as reported by previous studies [34].These three regimes are accelerating, steady state and decelerating. According to the Fig.6. one can conclude that the accelerating happened in $[T] < \sim 0.1$ and the decelaring in $[T] > \sim 8$.

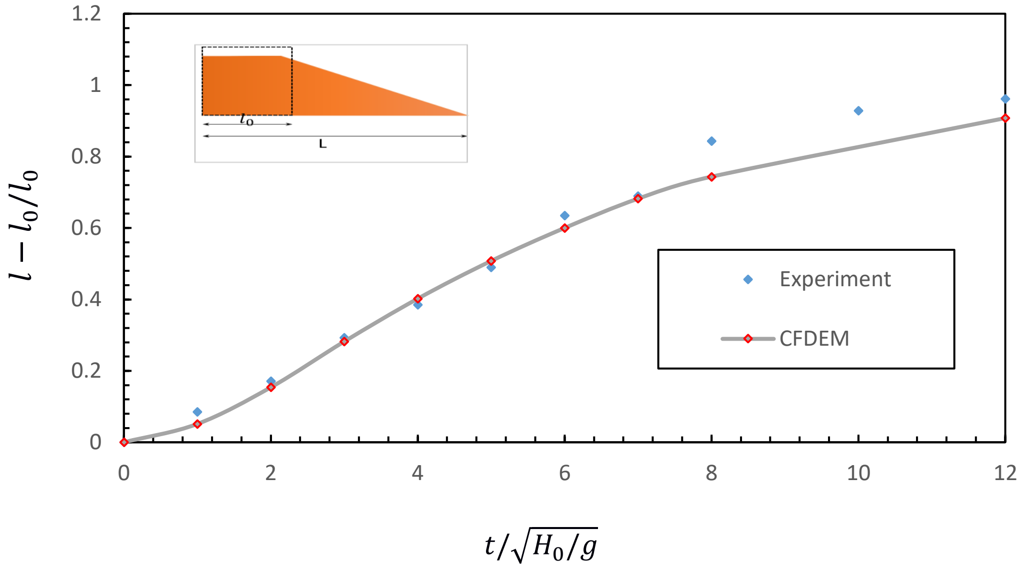

Figure 4-10 Runout distance for the submerged granular collapse

The velocity filed and vector for the submerged granular collapse also is shown in Figure 4-11. One can distinguish a non-yielded (with near-zero velocity) trapezoidal zones, and a yielded zone at the front and surfaces of the granular mass. As the time passes, the yielded zone becomes narrower and eventually disappears when the material come to the rest.

The velocity field shows a maximum velocity happens at [T]=4 and [T]=6 on the top of the surface of granular mass. This maximum velocity can be related to the effect of drag force implemented in the simulation.

The overall configuration of the submerged granular collapse is similar to that of the dry granular collapse presented in chapter 2. However, in the submerged granular collapse the failure happens in a longer time scale comparing to the dry case. Moreover, the thicker front of granular mass, smaller velocity is observed in the submerged case due to the effect of the forces acted from the fluid phase and the counterclockwise vortex in fluid phase on the solid particles [34].

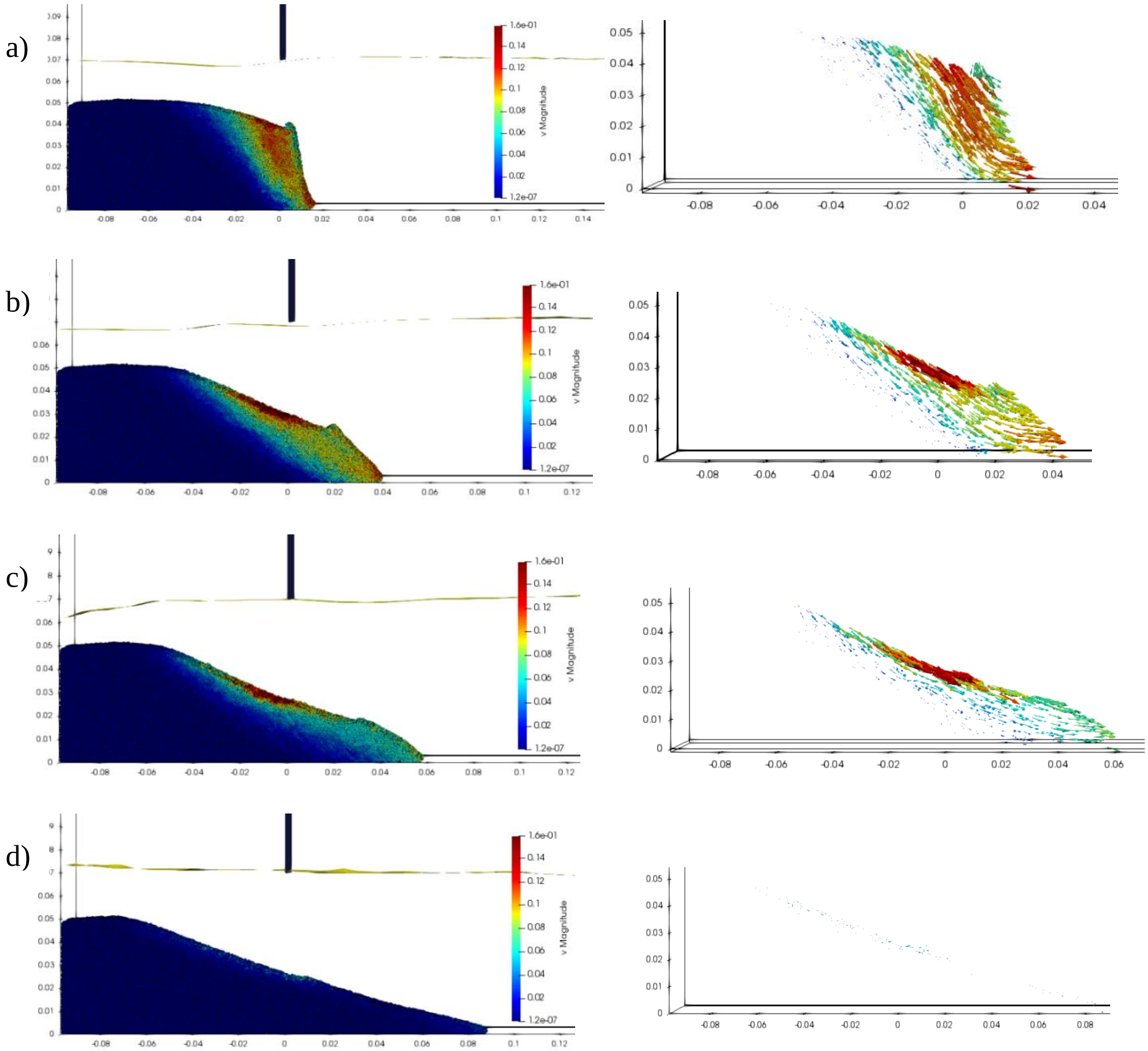

Figure 4-11 Velocity field and vector for submerged granular collapse (a) [T] =2,b) [T]=4, c) [T]=6 and d) final)

4.4.2.1 Sensitivity analysis of the friction coefficient for the submerged granular collapse

Owning to the large uncertainty associated with the external friction factor, and the important role of the coefficient of friction on the DEM results, a sensitivity analysis of the external friction coefficient has been carried out for the submerged case. Table 4-2 shows the parameters of three different simulations for the submerged granular collapse.

Table 4-2 Different friction coefficients for the submerged granular collapse test

No. simulation	Friction coefficient for particle-particle	Friction coefficient for particle-walls	Friction coefficient for particle-gate
1	0.4	0.4	0.4
2	0.4	0.15	0.4
3	0.4	0.1	0.4

Since the friction coefficient between particles and gate did not play a significant role in the evolution of the granular mass in the submerged granular collapse, this value was kept constant in all simulations. Figure 4-12 illustrates the runout distance for different simulations.

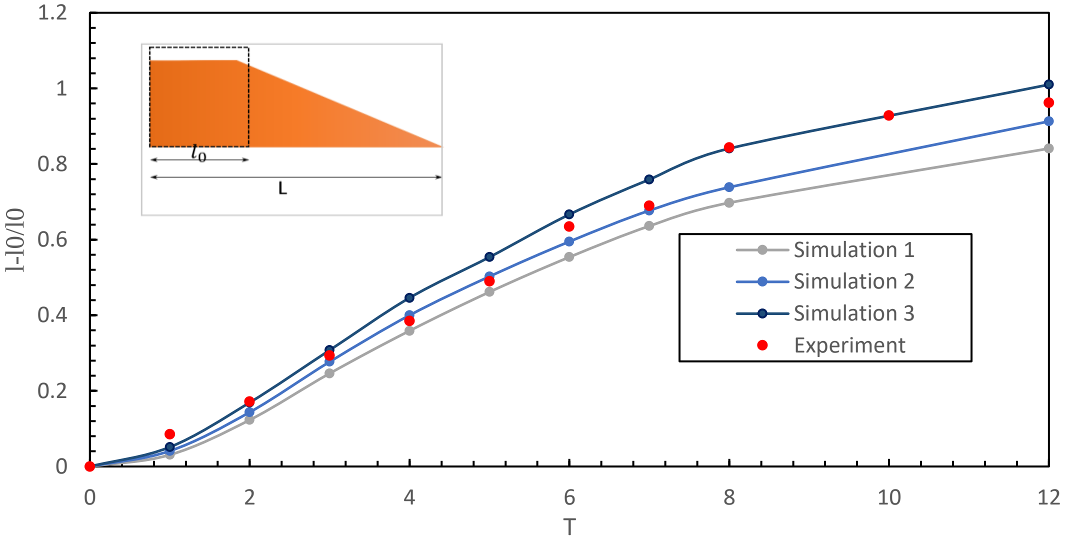

Figure 4-12 The runout distance of different simulations for the submerged granular collapse

From Figure 4-12 one can conclude that as the particles-walls coefficient of friction decreases, the runout distance obtained numerically gets closer to the experimental results. This can be explained by the fact that the friction between particles and walls is small due to the presence of the liquid phase. Using a coefficient friction of 0.1 for particle-wall shows accurate results for the runout distance, particularly in the final time steps.

4.4.3 Submerged granular slide

The granular slide test case consists of an inclined plane with 45 degree and a gate inside a tank. The length, width, and height of the tank are 0.7 m, 0.15 m and 0.3 m respectively. This test case also has don in at the Hydraulics Laboratory of Polytechnique Montreal by Prof. Ahmad shakibaeinia. Figure 4-13 represents the computational domain of the granular slide test case. A granular mass with a triangular shape and with a base (l_g) of 0.06 m and height (h_g) of 0.06 m is set behind the gate. The gate is located with the length and the height of 0.14 m from the slope toe $(l_0, h_0 = 0.2$ m). The tank is filled with a water height (h_f) of 0.25 m to completely submerge the granular column. The material properties are as same as the submerged granular collapse test case. The simulation is started by moving up the gate with a velocity of 1m/s. As Figure 4-13 shows the granular entirely is underwater. In this study, the initial volume fraction is around 60%. To simulate this case, similar to the granular collapse test case, firs the initial granular mass set behind the gate by running the pure LIGGGHTS. Then by setting the setFields the initial volume of water is added to the computational domain. The CFD-DEM simulation is started by moving up the gate. The mesh grid size is similar to the previous test case since the particle radius does not change in this test case.

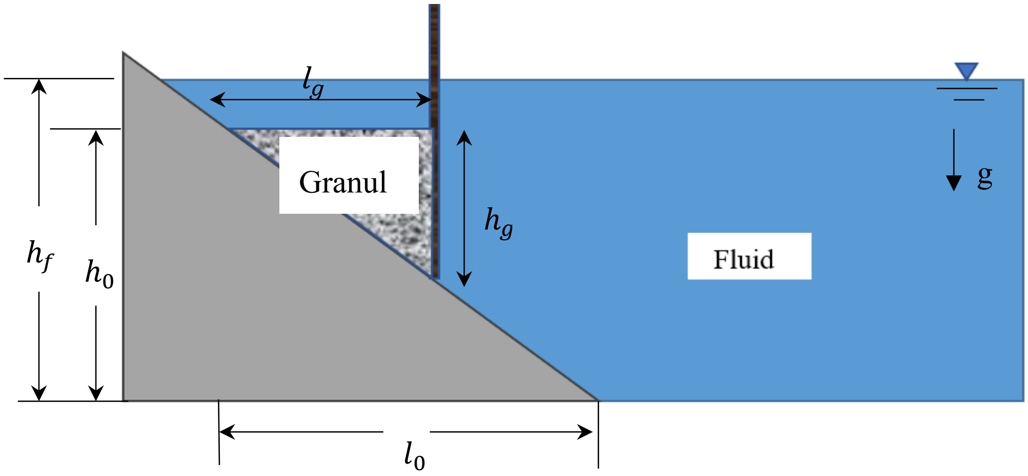

Figure 4-13 Initial configuration of the submerges granular slide

To validate the developed CFDEM solver, the simulation results and the experiment snapshots in different dimensionless time $(T = t/\sqrt{(\frac{h_0}{g})}$) are compared in Figure 4-14.

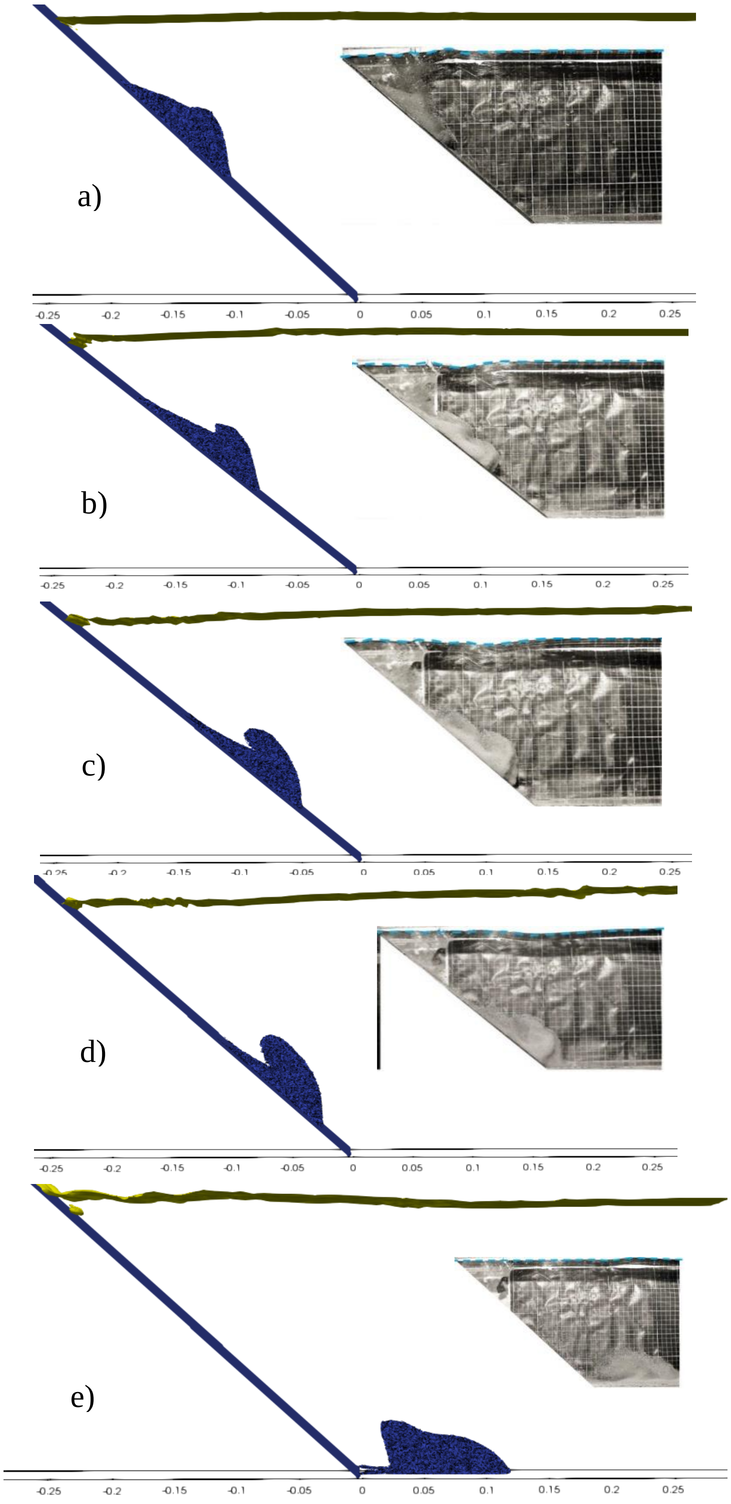

Figure 4-14 Numerical and experimental granular configuration evolution for submerged granular slide (a) [T] =2,b) [T]=3, c) [T]=4, d) [T]=5 and e) final)

As Figure 4-14 shows the granular mass slides down and stretched along the inclined plane with a slimmer tail and thicker front as observed in the experiment and the previous studies[24] .

The thicker front can also be due to forming a counter–clockwise vortex in the fluid phase near the frontier [35]. Similar to the experimental results, the simulation also showing an overall increase in the mean volume fraction comparing to the initial configuration. Contrasting to the simulation results, in the experimental results, the granular mass is associated with particles suspension which can be related to the shear stress of the gate removal mechanism [24]. In the simulation as mentioned before, the gate is defined in the DEM side and the fluid is not influenced by the gate. Hence, the suspension of the material is not observed around the granular mass in the simulation. The discrepancy of the evolution of granular mass in the simulation and the experiment also can be related to the gate mechanism.

In this test case, due to the particle's suspension in the experiment, the simulation and experimental surface profiles can not be easily quantified by plotting the surface profiles of the granular mass. The evolution of the front position shows a similar pattern in the experimental and numerical results. The numerical and experimental surface profiles of the granular mass show a similarity in the initial time steps, but the as time goes on a discrepancy is observed. In the experiments the fluid shear (and the resulted Kelvin-Helmholtz instability) creates two counter-clockwise circulations at the surface of granular mass. However, in the numerical results, only one circulation is observed. The reason for such discrepancy can be neglecting the interparticle fluid flow in the rapidly moving granular mass, though the unresolved CFD-DEM coupling. Other reason can be the initial disturbance caused by the gate removal mechanism, which has been ignored in the numerical simulation.

Fig presents the runout distance for the submerged granular slide for different simulations having different particle-wall friction coefficients. The runout distance predicted by the simulations indicates that the granular mass has a slower motion even with small value of friction coefficient comparing to the experimental results. This discrepancy may be related to the mechanism of the gate. In the experimental case, the fluid phase is influenced by the gate motion while in the simulation, the gate is only defined in the DEM side and does not influence the fluid.

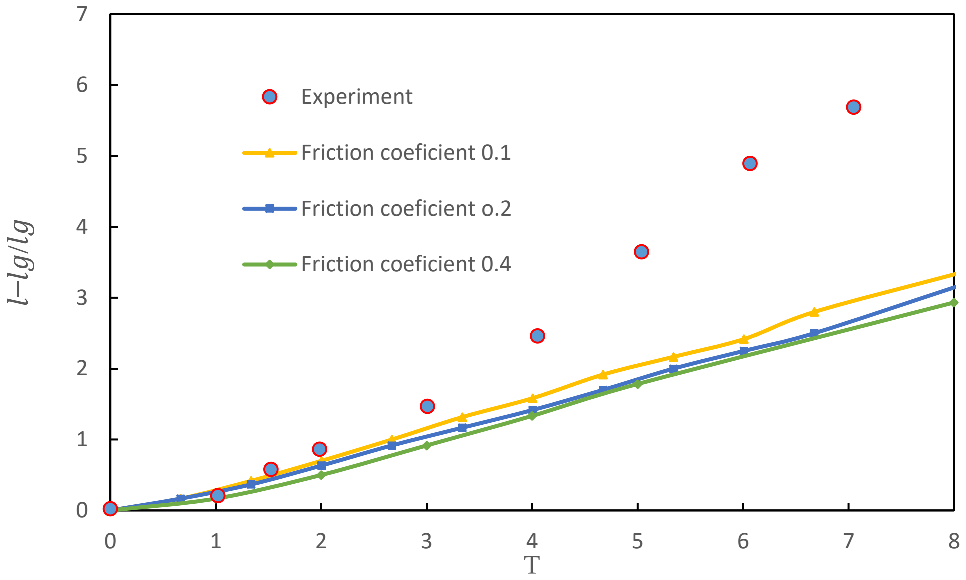

Figure 4-15 The runout distance of different simulations for the submerged granular slide

Figure 4-16 illustrates the snapshots of velocity fields and vector of the submerged landslide. The yielded and non-yielded zones can be distinguished. Moreover, the velocity vector shows the contraclockwise circulation on the front of granular mass as mentioned in previous studies [24].

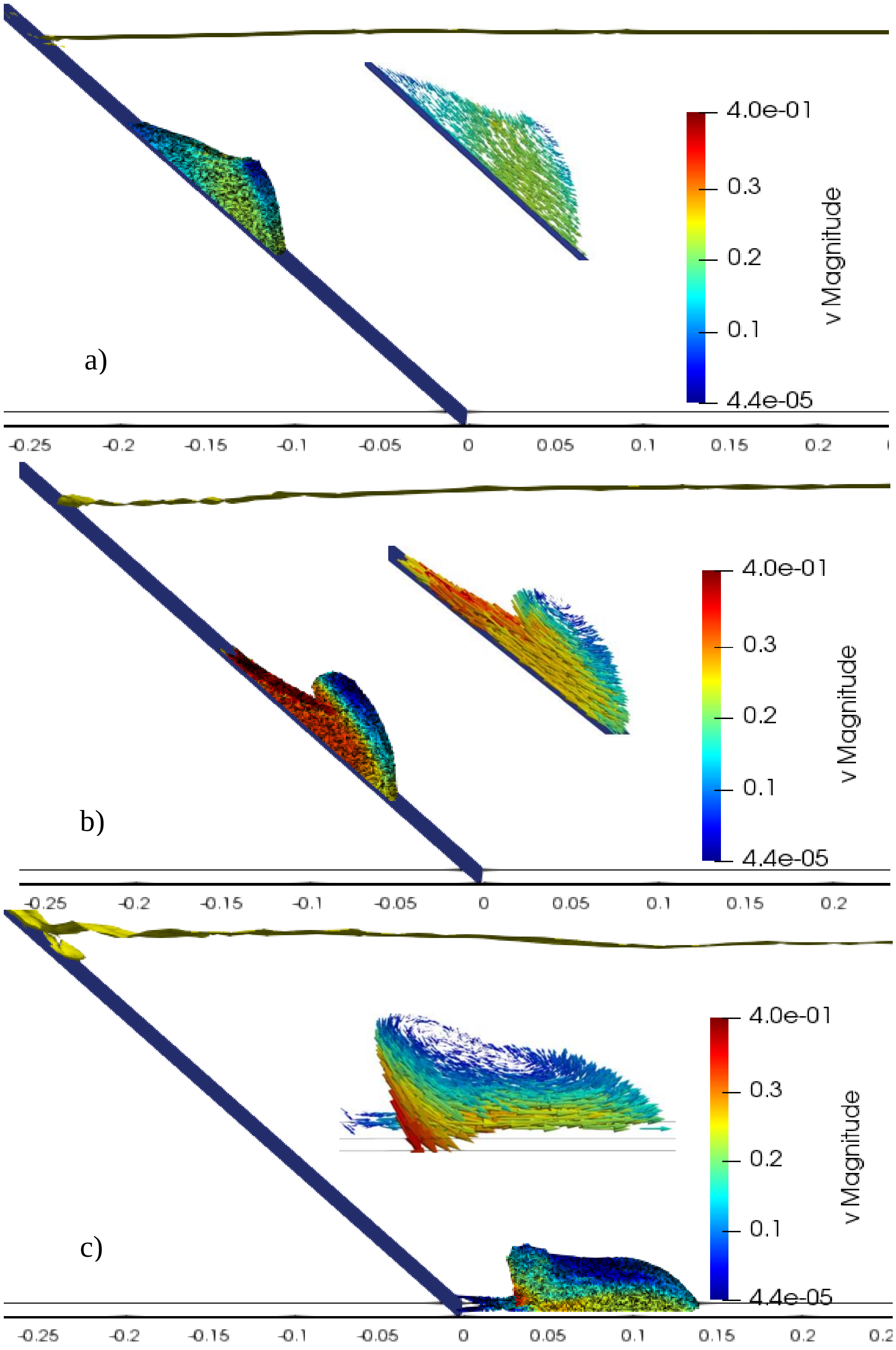

Figure 4-16 Velocity field and vector for submerged granular slide (a) [T]=2,b) [T]=4 and c) Final)

The water wave propagation in the simulation does not have a good agreement with the experimental observation. A turbulence model (k-epsilon) have been applied for this case and Fig shows two snapshots of that turbulence model against the experimental results. The free surface movement shows a better agreement with the experimental snapshot in comparison to the laminar model.

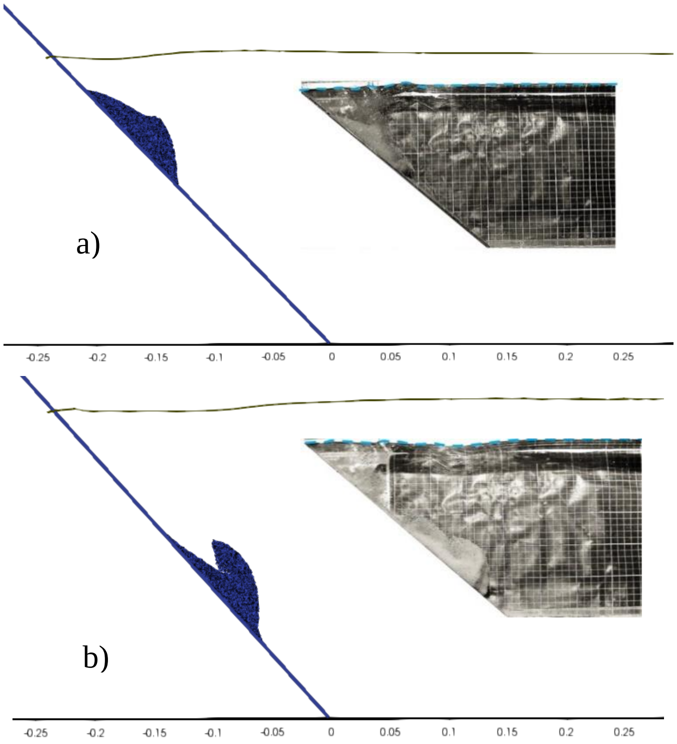

Figure 4-17 Turbulence model and experimental snapshots for submerged granular slide (a) [T] =2 and b) [T]=4)

4.5 Conclusion

A coupled CFD-DEM method has been developed to simulate free surface granular flows. in the coupling CFD-DEM, an open source code LIGGGHTS was employed to model the motion and interaction particle-particle. The fluid phase is modeled using the local averaged Navier-Stocks equation by means of the open source code OpenFOAM. To capture the free surface interface between the fluid(water) and gas(air), VOF method is incorporated to the CFD-DEM coupling by modifying the volume fraction due to the presence solid particles in the computational cells. The interaction between particles and fluid is conducted by exchanging the interaction forces including the drag force and buoyancy force between the DEM side and the CFD side. The developed model is validated by one single particle settling test and has a good agreement with the analytical solution. The model also for the submerged granular collapse provide reasonable results in comparison with experimental results. Validation of the submerged granular slide also shows the overall evolution of the granular mass is in a good agreement with the experimental snapshots in different time steps. However, a slower motion of granular mass has been observed in the simulation which can be related to the mechanism of gate in the simulation and experiment.

CHAPTER 5 CONCLUSION (AND RECOMMANDATIONS)

The aim of this study was to develop an unresolved CFD-DEM coupling to model multiphase gravity-driven granular flows. The DEM method was first implemented for the dry granular flows to validate and calibrate the DEM model by means of the open source code LIGGGHTS. To evaluate the effect of friction coefficient, different simulations for the dry granular collapse have been carried out. The results for the dry granular collapse indicated that the granular deposit was strongly influenced by the particle-wall, particle-gate, and particle-particle friction coefficients.

After the validation of the DEM model for the dry test cases were done, a CFD-DEM model for multiphase granular flows was developed. Two opensource codes, OpenFAOM and LIGGGHTS, were coupled together with another open source code called CFDEM. All available solvers in the public version of CFDEM open source code have been developed for two phase flows (i.e. fluid and solid). In order to model three-phase granular flows, a solver was developed to capture the free surface interfaces. The solver was developed by integrating the VOF method into the CFDEM code. To validate the solver, a particle falling from air to water was simulated and the results were compared with the analytical solutions. The position and velocity obtained in the validation were reasonable. The solver was implemented in the submerged granular collapse case. The overall deposit of granular mass was in good agreement with what was observed in the experimental results. The validation was conducted quantitatively by measuring the runout distance and the profile surfaces of the granular mass. The result presented in this study was based on the different coefficient frictions of particle-particle and particle-walls. Adopting a particle-wall friction coefficient that is smaller than the particle-particle friction coefficient produced results which closer to the experimental results.

The solver also was implemented for the submerged granular slide. The simulation results show that the evolution of the granular mass is in a good agreement with the experimental snapshots in different time steps. Using a turbulence model improved the results since the motion of the wave caused by the release of the granular column has a better agreement with the experimental wave motion compared to the laminar model. Nonetheless, a discrepancy was observed: in the experiments, the fluid shear created two counter-clockwise circulations at the surface of granular mass whereas in the numerical results, there is only one circulation observed. The reason for such discrepancy can be related to the fact that the interparticle fluid was neglected. In addition, the initial disturbance caused by the gate removal mechanism has been ignored in the numerical simulation. The effect of the gate can also affect the motion of the granular mass. From the runout distance result, one can conclude that the motion of the granular mass is slower than the motion in the experiment. This may be again related to the gate removal present in the experiment which caused the granular mass to speed up. In the simulation, since the gate is not defined in CFD, the fluid is not affected by the gate. To overcome this discrepancy, it is suggested to develop a model in which dynamic mesh could be defined in the CFD side.

These discrepancies of submerged granular slides may also be related to the assumptions of the unresolved CFD-DEM approach, which is the limitation of this approach. In this approach since the size of particles are smaller than the mesh size, the interparticle fluid flow in each CFD cell is neglected. To overcome these discrepancies, developing a resolved CFD-DEM approach is recommended.

REFERENCES

1. Forterre, Y. and O. Pouliquen, *Granular flows*, in *Glasses and Grains*. 2011, Springer. p. 77-109.
2. Jop, P., Y. Forterre, and O.J.N. Pouliquen, *A constitutive law for dense granular flows.* 2006. **441**(7094): p. 727-730.
3. Lemaître, A., J.-N. Roux, and F.J.R.a. Chevoir, *What do dry granular flows tell us about dense non-Brownian suspension rheology?* 2009. **48**(8): p. 925-942.
4. *30 Interesting Facts About Food Grains.* 2016.
5. *List of landslides.* 2007.
6. *Assay of Pharmaceutical Products.* 2020.
7. *These Beaches Have The Whitest Sand In The World.* 2016.
8. *Iran-Made Polypropylene Catalyst to Hit Market by March.* 2019.
9. Brennen, C.E. and C.E. Brennen, *Fundamentals of multiphase flow*. 2005: Cambridge university press.
10. Takahashi, T. and D.K. Das, *Debris flow: mechanics, prediction and countermeasures*. 2014: CRC press.
11. MINISTRY, Q.T., *Landslides are Canada's forgotten menace. How can we predict them and save lives?*

. 2018.

12. Dellino, P., et al., *A method for the calculation of the impact parameters of dilute pyroclastic density currents based on deposit particle characteristics.* 2008. **113**(B7).
13. Gurioli, L., et al., *Interaction of pyroclastic density currents with human settlements: evidence from ancient Pompeii.* 2005. **33**(6): p. 441-444.
14. Dartevelle, S.J.G., Geophysics, Geosystems, *Numerical modeling of geophysical granular flows: 1. A comprehensive approach to granular rheologies and geophysical multiphase flows.* 2004. **5**(8).
15. Pouliquen, O., et al., *How do grains flow: towards a simple rheology for dense granular flows.* 2005: p. 859-865.
16. Ancey, C., P. Coussot, and P.J.J.o.R. Evesque, *A theoretical framework for granular suspensions in a steady simple shear flow.* 1999. **43**(6): p. 1673-1699.
17. Savage, S.B. and K.J.J.o.f.m. Hutter, *The motion of a finite mass of granular material down a rough incline.* 1989. **199**: p. 177-215.
18. Pouliquen, O. and Y.J.J.o.f.m. Forterre, *Friction law for dense granular flows: application to the motion of a mass down a rough inclined plane.* 2002. **453**: p. 133-151.

19. Huppert, H., et al. *Granular column collapses*. in *APS Division of Fluid Dynamics Meeting Abstracts*. 2003.

20. Lube, G., et al., *Collapses of two-dimensional granular columns.* 2005. **72**(4): p. 041301.

21. Lube, G., et al., *Axisymmetric collapses of granular columns.* 2004. **508**: p. 175-199.

22. Lajeunesse, E., A. Mangeney-Castelnau, and J.J.P.o.f. Vilotte, *Spreading of a granular mass on a horizontal plane.* 2004. **16**(7): p. 2371-2381.

23. Thompson, E.L. and H.E.J.J.o.F.M. Huppert, *Granular column collapses: further experimental results.* 2007. **575**: p. 177-186.

24. Pilvar, M., M. Pouraghniaei, and A.J.P.o.F. Shakibaeinia, *Two-dimensional sub-aerial, submerged, and transitional granular slides.* 2019. **31**(11): p. 113303.

25. Lajeunesse, E., J. Monnier, and G.J.P.o.f. Homsy, *Granular slumping on a horizontal surface.* 2005. **17**(10): p. 103302.

26. Pudasaini, S.P., et al., *Velocity measurements in dry granular avalanches using particle image velocimetry technique and comparison with theoretical predictions.* 2005. **17**(9): p. 093301.

27. Lueptow, R.M., A. Akonur, and T.J.E.i.F. Shinbrot, *PIV for granular flows.* 2000. **28**(2): p. 183-186.

28. Wu, W., Rodi, W., & Wenka, T, *3D numerical modeling of flow and sediment transport in open channels.* Journal of hydraulic engineering, 2000. **126(1), 4-15.**

29. Van Rijn, L.C., *Mathematical modelling of morphological processes in the case of suspended sediment transport.* 1987.

30. Zhou, Z., et al., *Discrete particle simulation of particle–fluid flow: model formulations and their applicability.* 2010. **661**: p. 482-510.

31. Anderson, T.B., R.J.I. Jackson, and E.C. Fundamentals, *Fluid mechanical description of fluidized beds. Equations of motion.* 1967. **6**(4): p. 527-539.

32. Koshizuka, S., Y.J.N.s. Oka, and engineering, *Moving-particle semi-implicit method for fragmentation of incompressible fluid.* 1996. **123**(3): p. 421-434.

33. Gingold, R. and J. Monaghan, *Smoothed particle hydrodynamics, theory and application to non-spherical stars.[Statistical techniques, equations of motion].* 1977.

34. Nodoushan, E.J., A. Shakibaeinia, and K.J.P.T. Hosseini, *A multiphase meshfree particle method for continuum-based modeling of dry and submerged granular flows.* 2018. **335**: p. 258-274.

35. Tajnesaie, M., et al., *Meshfree particle numerical modelling of sub-aerial and submerged landslides.* 2018. **172**: p. 109-121.

36. Zhu, H., et al., *Discrete particle simulation of particulate systems: theoretical developments.* 2007. **62**(13): p. 3378-3396.

37. Cundall, P.A. and O.D.J.g. Strack, *A discrete numerical model for granular assemblies.* 1979. **29**(1): p. 47-65.

38. Alice Jordam Caserta, H.e.A.N., Luben Cabezas-G´omez, *Damping coefficient and contact duration relations for continuous nonlinear*

spring-dashpot contact model in DEM. Powder Technology, 2016.

39. Zhu, H., et al., *Discrete particle simulation of particulate systems: a review of major applications and findings.* 2008. **63**(23): p. 5728-5770.

40. Di Renzo, A. and F.P.J.C.e.s. Di Maio, *Comparison of contact-force models for the simulation of collisions in DEM-based granular flow codes.* 2004. **59**(3): p. 525-541.

41. Hertz, H.J.J.r.a.M., *Ueber die Beruhrung fester elastischer Korper.* 1882. **92**: p. 156-171.

42. Mindlin, R.D.J.J.A.M., *Elastic spheres in contact under varying oblique forces.* 1953. **20**: p. 327-344.

43. Langston, P., U. Tüzün, and D.J.C.E.S. Heyes, *Continuous potential discrete particle simulations of stress and velocity fields in hoppers: transition from fluid to granular flow.* 1994. **49**(8): p. 1259-1275.

44. Thornton, C., *Coefficient of restitution for collinear collisions of elastic-perfectly plastic spheres.* 1997.

45. Zhou, Y., et al., *Rolling friction in the dynamic simulation of sandpile formation.* 1999. **269**(2-4): p. 536-553.

46. Iwashita, K. and M.J.J.o.e.m. Oda, *Rolling resistance at contacts in simulation of shear band development by DEM.* 1998. **124**(3): p. 285-292.

47. Pelessone, D., *Discrete element simulations using macro-particles*, in *Computational Fluid and Solid Mechanics 2003*. 2003, Elsevier. p. 2089-2092.

48. Bertrand, F., L.-A. Leclaire, and G.J.C.E.S. Levecque, *DEM-based models for the mixing of granular materials.* 2005. **60**(8-9): p. 2517-2531.

49. Hamaker, H.C.J.p., *The London—van der Waals attraction between spherical particles.* 1937. **4**(10): p. 1058-1072.

50. Krupp, H.J.C. and i.Z. Sci, *Particle adhesion. Theory and experiment. Adunn.* 1967. **1**: p. I1.

51. Fisher, R.J.T.J.o.A.S., *On the capillary forces in an ideal soil; correction of formulae given by WB Haines.* 1926. **16**(3): p. 492-505.

52. Lian, G., et al., *A theoretical study of the liquid bridge forces between two rigid spherical bodies.* 1993. **161**(1): p. 138-147.

53. Zhou, Y., et al., *Numerical investigation of the angle of repose of monosized spheres.* 2001. **64**(2): p. 021301.

54. Zhou, Y., et al., *An experimental and numerical study of the angle of repose of coarse spheres.* 2002. **125**(1): p. 45-54.

55. Wei, H., et al., *Discrete Element Method (DEM) and Experimental Studies of the Angle of Repose and Porosity Distribution of Pellet Pile.* 2019. **7**(9): p. 561.

56. Li, C., et al., *The angle of repose and size segregation of iron ore granules: DEM analysis and experimental investigation.* 2017. **320**: p. 257-272.

57. Matuttis, H., S. Luding, and H.J.P.t. Herrmann, *Discrete element simulations of dense packings and heaps made of spherical and non-spherical particles.* 2000. **109**(1-3): p. 278-292.

58. Zhou, Y., et al., *Stress distribution in a sandpile formed on a deflected base.* 2003. **14**(4): p. 401-410.

59. Tordesillas, A., et al., *Stress–dilatancy and force chain evolution.* 2011. **35**(2): p. 264-292.

60. Wang, W., W. Gu, and K.J.T.T. Liu, *Force chain evolution and force characteristics of shearing granular media in Taylor-Couette geometry by DEM.* 2015. **58**(2): p. 197-206.

61. Zhang, X. and L.J.M.o.M. Vu-Quoc, *Simulation of chute flow of soybeans using an improved tangential force–displacement model.* 2000. **32**(2): p. 115-129.

62. Hanes, D.M. and O.R.J.P.t. Walton, *Simulations and physical measurements of glass spheres flowing down a bumpy incline.* 2000. **109**(1-3): p. 133-144.

63. Teufelsbauer, H., et al., *DEM simulation of impact force exerted by granular flow on rigid structures.* 2011. **6**(3): p. 119.

64. Lo, C., M. Bolton, and Y.J.G.M. Cheng, *Velocity fields of granular flows down a rough incline: a DEM investigation.* 2010. **12**(5): p. 477-482.

65. Teufelsbauer, H., et al., *Flow–obstacle interaction in rapid granular avalanches: DEM simulation and comparison with experiment.* 2009. **11**(4): p. 209-220.

66. Zhou, G.G. and Q.J.P.t. Sun, *Three-dimensional numerical study on flow regimes of dry granular flows by DEM.* 2013. **239**: p. 115-127.

67. Langston, P.A., U. Tüzün, and D.M.J.C.E.S. Heyes, *Discrete element simulation of granular flow in 2D and 3D hoppers: dependence of discharge rate and wall stress on particle interactions.* 1995. **50**(6): p. 967-987.

68. Holst, J.M.F., et al., *Numerical modeling of silo filling. I: continuum analyses.* 1999. **125**(1): p. 94-103.

69. Masson, S. and J.J.P.T. Martinez, *Effect of particle mechanical properties on silo flow and stresses from distinct element simulations.* 2000. **109**(1-3): p. 164-178.

70. Cleary, P.W. and M.L.J.A.M.M. Sawley, *DEM modelling of industrial granular flows: 3D case studies and the effect of particle shape on hopper discharge.* 2002. **26**(2): p. 89-111.

71. Goda, T.J. and F.J.P.t. Ebert, *Three-dimensional discrete element simulations in hoppers and silos.* 2005. **158**(1-3): p. 58-68.

72. Balevičius, R., et al., *Analysis and DEM simulation of granular material flow patterns in hopper models of different shapes.* 2011. **22**(2): p. 226-235.

73. Kuo, H., et al., *The influence of DEM simulation parameters on the particle behaviour in a V-mixer.* 2002. **57**(17): p. 3621-3638.

74. Lemieux, M., et al., *Comparative study of the mixing of free-flowing particles in a V-blender and a bin-blender.* 2007. **62**(6): p. 1783-1802.

75. Chen, W., et al., *Numerical simulation of mechanofusion system.* 2004. **146**(1-2): p. 121-136.

76. Maione, R., et al., *DEM investigation of granular flow and binary mixture segregation in a rotating tumbler: Influence of particle shape and internal baffles.* 2015. **286**: p. 732-739.

77. Maione, R., et al., *Axial segregation of a binary mixture in a rotating tumbler with non-spherical particles: experiments and DEM model validation.* 2017. **306**: p. 120-129.

78. Tsuji, Y., T. Kawaguchi, and T.J.P.t. Tanaka, *Discrete particle simulation of two-dimensional fluidized bed.* 1993. **77**(1): p. 79-87.

79. Bérard, A., Gregory S. Patience, and Bruno Blais, *Experimental Methods in Chemical Engineering: Unresolved CFD-DEM.* The Canadian Journal of Chemical Engineering 2020.

80. Kloss, C., et al., *Models, algorithms and validation for opensource DEM and CFD–DEM.* 2012. **12**(2-3): p. 140-152.

81. Hager, A.J.J.K.U.L., Linz, *CFD-DEM on multiple scales: An extensive investigation of particle–fluid interactions.* 2014.

82. Hoomans, B., et al., *Discrete particle simulation of bubble and slug formation in a two-dimensional gas-fluidised bed: a hard-sphere approach.* 1996. **51**(1): p. 99-118.

83. Kuwagi, K., T. Mikami, and M.J.P.T. Horio, *Numerical simulation of metallic solid bridging particles in a fluidized bed at high temperature.* 2000. **109**(1-3): p. 27-40.

84. Yuu, S., T. Umekage, and Y.J.P.T. Johno, *Numerical simulation of air and particle motions in bubbling fluidized bed of small particles.* 2000. **110**(1-2): p. 158-168.

85. Bin, Y., et al., *Discrete particle simulation and visualized research of the gas− solid flow in an internally circulating fluidized bed.* 2003. **42**(1): p. 214-221.

86. Limtrakul, S., et al., *Discrete particle simulation of solids motion in a gas–solid fluidized bed.* 2003. **58**(3-6): p. 915-921.

87. Xu, B. and A.J.C.E.S. Yu, *Numerical simulation of the gas-solid flow in a fluidized bed by combining discrete particle method with computational fluid dynamics.* 1997. **52**(16): p. 2785-2809.

88. Xu, B., et al., *A numerical and experimental study of the gas-solid flow in a fluid bed reactor.* 2001. **13**(1): p. 71-76.

89. Zhou, H., et al., *Simulation of heavy metal vaporization dynamics in a fluidized bed.* 2002. **57**(14): p. 2603-2614.

90. Ku, X., T. Li, and T.J.C.E.S. Løvås, *CFD–DEM simulation of biomass gasification with steam in a fluidized bed reactor.* 2015. **122**: p. 270-283.

91. Liu, R., et al., *CFD-DEM modelling of mixing of granular materials in multiple jets fluidized beds.* 2020. **361**: p. 315-325.

92. Alobaid, F. and B.J.P. Epple, *Improvement, validation and application of CFD/DEM model to dense gas–solid flow in a fluidized bed.* 2013. **11**(5): p. 514-526.

93. Zhao, J. and T.J.P.t. Shan, *Coupled CFD–DEM simulation of fluid–particle interaction in geomechanics.* 2013. **239**: p. 248-258.

94. Zhao, T., et al., *Investigation of submerged debris flows via CFD-DEM coupling.* 2014: p. 497-502.

95. Chen, F., et al., *Coupled discrete element and finite volume solution of two classical soil mechanics problems.* 2011. **38**(5): p. 638-647.

96. Sussman, M., P. Smereka, and S. Osher, *A level set approach for computing solutions to incompressible two-phase flow.* 1994.

97. Hirt, C.W. and B.D.J.J.o.c.p. Nichols, *Volume of fluid (VOF) method for the dynamics of free boundaries.* 1981. **39**(1): p. 201-225.

98. Mao, J., et al., *A resolved CFD–DEM approach for the simulation of landslides and impulse waves.* 2020. **359**: p. 112750.

99. Wu, L., et al., *Development of a DEM–VOF model for the turbulent free-surface flows with particles and its application to stirred mixing system.* 2018. **57**(5): p. 1714-1725.

100. Jing, L., et al., *Extended CFD–DEM for free-surface flow with multi-size granules.* 2016. **40**(1): p. 62-79.

101. Sun, X. and M.J.C.E.S. Sakai, *Three-dimensional simulation of gas–solid–liquid flows using the DEM–VOF method.* 2015. **134**: p. 531-548.

102. Zhao, T., F. Dai, and N.-w.J.L. Xu, *Coupled DEM-CFD investigation on the formation of landslide dams in narrow rivers.* 2017. **14**(1): p. 189-201.

103. Shan, T. and J.J.A.M. Zhao, *A coupled CFD-DEM analysis of granular flow impacting on a water reservoir.* 2014. **225**(8): p. 2449-2470.

104. Padrós, C.B., *Discrete element simulations with LIGGGHTS.* College of Engineering in Computational Mechanics. Swansea University, 2014.

105. Blais, B., et al., *Experimental Methods in Chemical Engineering: Discrete Element Method—DEM.* 2019. **97**(7): p. 1964-1973.

106. *LIGGGHTS documentation.* 2018.

107. 2015.

108. Kloss, C., & Goniva, C. , *LIGGGHTS–open source discrete element simulations of granular materials based on Lammps.* Materials Fabrication, Properties, Characterization, and Modeling, 2011. **2**: p. 781-788.

109. *LIGGGHTS documentation* 2016.

110. Suhr, B., and Klaus Six, *On the effect of stress dependent interparticle friction in direct shear tests.* Powder Technology, 2016. **294**: p. 211-220.

111. Yan, Z., et al, *Discrete element modelling (DEM) input parameters: understanding their impact on model predictions using statistical analysis.* Computational Particle Mechanics 2015. **2.3**: p. 283-299.

112. 2020.

113. Lobovský. E.Botia-Vera b, F.C.c., J.Mas-Soler b, A.Souto-Iglesias, *Experimentalinvestigationofdynamicpressureloads*

during dambreak. Journal of Fluids and Structures, 2014. **48**: p. 407-434.

114. Vinay R. Gopala ∗, B.G.M.v.W., *interface Volume of fluid methods for immiscible-fluid and free-surface flows* Department of Applied Mechanics, Chalmers University of Technology, 2008.

115. Berberović Edin, N.P.v.H., Suad Jakirlić, Ilia V. Roisman, and Cameron Tropea, *Drop impact onto a liquid layer of finite thickness: Dynamics of the cavity evolution.* PHYSICAL REVIEW, 2009. **79**.

116. Science, R.H.U.o.L.a.D.o.I.C.I.C.o., *Computational Fluid Dynamics of Dispersed Two-Phase Flows at High Phase Fractions.* 2002.

117. Jasak Hrvoje % University of London and Diploma of Imperial College Department of Mechanical Engineering Imperial College of Science, T.a.M., *Error Analysis and Estimation for the Finite Volume Method with Applications to Fluid Flows.* 1996.

118. Jasak Hrvoje Aleksandar Jemcov3 , Z.T.W.L., *A C++ Library for Complex Physics Simulations.* International Workshop on Coupled Methods in Numerical Dynamics IUC, Dubrovnik, Croatia, September 19th, 2007.

119. Ginzburg, I., and G. Wittum, *Two-phase flows on interface refined grids modeled with VOF, staggered finite volumes, and spline interpolants.* Journal of Computational Physics 2001. **166.2**: p. 302-335.

120. Bathe, K.-J., and Hou Zhang, *A mesh adaptivity procedure for CFD and fluid-structure interactions.* Computers & Structures 2009. **11-12**: p. 604-617.

121. Hager, A.J.J.K.U.L., Linz, *Cfd-dem on multiple scales-an extensive investigation of particle-fluid interactions.* 2014.

122. Fantin, D., *CFD-DEM Coupling for Systems of Fluid and Non-Spherical Particles.* 2018.

123. Link J.M., L.A.C., N.G. Deen∗, J.A.M. Kuipers, *Flowregimes in a spout–fluid bed:Acombined experimental and*

simulation study. Chemical Engineering Science, 2005

60: p. 3425 – 3442.

124. Blais, B., Lassaigne, M., Goniva, C., Fradette, L., & Bertrand, F, *Development of an unresolved CFD–DEM model for the flow of viscous suspensions and its application to solid–liquid mixing.* Computational Physics, 2016. **318**: p. 201-221.